NUREG/CR-6273
ORNL/TM-12866

Biaxial Loading Effects on Fracture Toughness of Reactor Pressure Vessel Steel

Prepared by
W. J. McAfee, B. R. Bass, J. W. Bryson, Jr., W. E. Pennell

Oak Ridge National Laboratory

Prepared for
U.S. Nuclear Regulatory Commission

AVAILABILITY NOTICE

Availability of Reference Materials Cited in NRC Publications

Most documents cited in NRC publications will be available from one of the following sources:

1. The NRC Public Document Room, 2120 L Street, NW., Lower Level, Washington, DC 20555-0001

2. The Superintendent of Documents, U.S. Government Printing Office, P. O. Box 37082, Washington, DC 20402-9328

3. The National Technical Information Service, Springfield, VA 22161-0002

Although the listing that follows represents the majority of documents cited in NRC publications, it is not intended to be exhaustive.

Referenced documents available for inspection and copying for a fee from the NRC Public Document Room include NRC correspondence and internal NRC memoranda; NRC bulletins, circulars, information notices, inspection and investigation notices; licensee event reports; vendor reports and correspondence; Commission papers; and applicant and licensee documents and correspondence.

The following documents in the NUREG series are available for purchase from the Government Printing Office: formal NRC staff and contractor reports, NRC-sponsored conference proceedings, international agreement reports, grantee reports, and NRC booklets and brochures. Also available are regulatory guides, NRC regulations in the *Code of Federal Regulations*, and *Nuclear Regulatory Commission Issuances*.

Documents available from the National Technical Information Service include NUREG-series reports and technical reports prepared by other Federal agencies and reports prepared by the Atomic Energy Commission, forerunner agency to the Nuclear Regulatory Commission.

Documents available from public and special technical libraries include all open literature items, such as books, journal articles, and transactions. *Federal Register* notices, Federal and State legislation, and congressional reports can usually be obtained from these libraries.

Documents such as theses, dissertations, foreign reports and translations, and non-NRC conference proceedings are available for purchase from the organization sponsoring the publication cited.

Single copies of NRC draft reports are available free, to the extent of supply, upon written request to the Office of Administration, Distribution and Mail Services Section, U.S. Nuclear Regulatory Commission, Washington, DC 20555-0001.

Copies of industry codes and standards used in a substantive manner in the NRC regulatory process are maintained at the NRC Library, Two White Flint North, 11545 Rockville Pike, Rockville, MD 20852-2738, for use by the public. Codes and standards are usually copyrighted and may be purchased from the originating organization or, if they are American National Standards, from the American National Standards Institute, 1430 Broadway, New York, NY 10018-3308.

DISCLAIMER NOTICE

This report was prepared under an international cooperative agreement for the exchange of technical information. Neither the United States Government nor any agency thereof, nor any of their employees, makes any warranty, expressed or implied, or assumes any legal liability or responsibility for any third party's use, or the results of such use, of any information, apparatus, product, or process disclosed in this report, or represents that its use by such third party would not infringe privately owned rights.

DISCLAIMER

NUREG/CR-6273
ORNL/TM-12866

Biaxial Loading Effects on Fracture Toughness of Reactor Pressure Vessel Steel

Manuscript Completed: January 1995
Date Published: March 1995

Prepared by
W. J. McAfee, B. R. Bass, J. W. Bryson, Jr., W. E. Pennell

Oak Ridge National Laboratory
Managed by Martin Marietta Energy Systems, Inc.

Oak Ridge National Laboratory
Oak Ridge, TN 37831-6285

Prepared for
Division of Engineering Technology
Office of Nuclear Regulatory Research
U.S. Nuclear Regulatory Commission
Washington, DC 20555-0001
NRC Job Code B0119

Abstract

The preliminary phases of a program to develop and evaluate fracture methodologies for the assessment of crack-tip constraint effects on fracture toughness of reactor pressure vessel (RPV) steels have been completed by the Heavy-Section Steel Technology (HSST) Program. The primary objectives of this effort were to analytically and experimentally investigate the effect of biaxial loading on fracture toughness, to quantify this effect through use of existing stress-based, dual-parameter, fracture-toughness correlations, or to propose and verify alternate correlations. A cruciform beam specimen with a two-dimensional, shallow, through-thickness flaw and a special loading fixture was designed and fabricated. Tests were performed using biaxial loading ratios of 0:1 (uniaxial), 0.6:1, and 1:1 (equibiaxial). Critical fracture-toughness values were calculated for each test. Biaxial loading of 0.6:1 resulted in a reduction in the lower bound fracture toughness of ~12% as compared to that from the uniaxial tests. The biaxial loading of 1:1 yielded two subsets of toughness values; one agreed well with the uniaxial data, while one was reduced by ~43% when compared to the uniaxial data. The results were evaluated using the J-Q theory and the Dodds-Anderson (D-A) micromechanical scaling model. The D-A model predicted no biaxial effect, while the J-Q method gave inconclusive results. When applied to the 1:1 biaxial data, these constraint methodologies failed to predict the observed reduction in fracture toughness obtained in one experiment. A strain-based constraint methodology that considers the relationship between applied biaxial load, the plastic zone width in the crack plane, and fracture toughness was formulated and applied successfully to the data. Evaluation of this dual-parameter strain-based model led to the conclusion that it has the capability of representing fracture behavior of RPV steels in the transition region, including the effects of out-of-plane loading on fracture toughness. This report is designated as HSST Report No. 150.

Contents

List of Figures

List of Tables

1 Introduction

Pressurized-thermal-shock (PTS) loading produces biaxial pressure and thermal stress fields in a reactor pressure vessel (RPV) wall. Thermal stresses are highest adjacent to the inner surface of the vessel where the effects of irradiation embrittlement and transient temperatures combine to produce the maximum reduction in the material fracture toughness. The net result of this combination of conditions is that the majority of predicted crack initiations originate from shallow flaws located on the inner surface of the vessel. The dominant influence of shallow surface flaws generates a need for an experimental investigation of (1) the effect of reduced crack-tip constraint on the material fracture toughness associated with shallow flaws, and (2) the effect of prototypical biaxial stress states on the material shallow-flaw fracture toughness, coupled with (3) development and validation of dual-parameter correlations that can be used to predict the material fracture toughness associated with shallow flaws in a biaxial stress field.

This report provides a review of ongoing work within the Heavy-Section Steel Technology (HSST) Program aimed at evaluating effects of these factors on fracture toughness of RPV steels. A validated technology that incorporates constraint effects associated with shallow cracks and biaxial loading is essential to the transfer of fracture-toughness data to RPVs from, for example, miniature fracture-toughness surveillance specimens. Consequently, assessment of dual-parameter fracture-toughness correlations through applications to measured data from testing programs represents a major element of this research program.

1.1 Shallow-Flaw Effects

Fracture-toughness tests have been performed on single-edge-notch bend (SENB) test specimens using both deep (a/W = 0.5) and shallow (a/W = 0.1) flaws.[1,2] Beam specimens used in these tests are shown in Figs. 1.1 and 1.2. The beams tested by Oak Ridge National Laboratory (ORNL) (Fig. 1.1) were fabricated from A 533 B material and were nominally 100 mm (4 in.) deep. Beams with a 230-mm-square (9-in.) cross section (Fig. 1.2) were cut from the RPV from a canceled nuclear plant and tested, under an HSST Program subcontract, by the National Institute for Standards and Technology (NIST), Gaithersburg, Maryland. The inner-surface stainless steel cladding remained in place on the large-scale beams tested by NIST, and the flaws were located in the RPV longitudinal welds. Additional shallow-flaw fracture-toughness data for A 533 B material were generated by the Fatigue and Fracture Branch of the Naval Surface Warfare Center (NSWC) in Annapolis, Maryland.[3] Material for the NSWC tests was heat-treated to increase its yield stress. The NSWC tests were also conducted using large [B = 89 mm (3.5 in.), W = 83 mm (3.25 in.)] SENB specimens. Use of large-scale beams permitted testing of shallow flaws with depths in the range identified as critical for PTS analysis. Use of prototypical flaw depths reduced the uncertainties associated with extrapolation of shallow-flaw fracture-toughness data for application to full-scale structures. Data from Refs. 1–3 were generated using large-scale SENB specimens fabricated from RPV steel. They can, therefore, be combined into deep- and shallow-flaw data sets.

Figures 1.3 and 1.4 show that deep- and shallow-flaw fracture-toughness data from Refs. 1–3 form a homogeneous population when plotted as a function of T – NDT. A single curve defines the lower bound to the shallow-flaw fracture-toughness data sets. A comparison of Figs. 1.3 and 1.4 shows that the lower-bound curves for the deep- and shallow-flaw data are similar, but the mean fracture toughness and scatter of data are significantly higher for shallow flaws than for deep flaws.

1.2 Biaxial Loading Conditions

A typical biaxial stress field produced by PTS transient loading is shown in Fig. 1.5, together with a constant-depth shallow surface flaw. One of the principal stresses is seen to be aligned parallel to the crack front. There is no counterpart of this far-field out-of-plane stress in the shallow-flaw fracture-toughness tests previously described. The far-field out-of-plane stress has the potential to increase stress triaxiality (constraint) at the crack tip and thereby reduce some of the fracture-toughness elevation and data scatter associated with shallow flaws. The HSST biaxial test program[4,5] was instituted to investigate this effect.

A cruciform test specimen[4] was developed at ORNL to investigate the effects of biaxial loading on the shallow-flaw fracture toughness of pressure vessel steels. Conceptual features of the specimen are shown in Fig. 1.6. The specimen design is capable of reproducing a linear approximation of the nonlinear biaxial stress distribution shown in Fig. 1.5. The cruciform design, coupled with a statically determinate load reaction system, permits the specimen to be loaded in either uniaxial (four-point bending) or biaxial (eight-point bending) configurations. Tests of nominally identical specimens can thus be performed with the level of stress biaxiality as the only test variable. Detailed results from testing and analysis of cruciform specimens within the HSST Program are described herein and in Refs. 4 and 5.

ORNL-PHOTO 8024-91

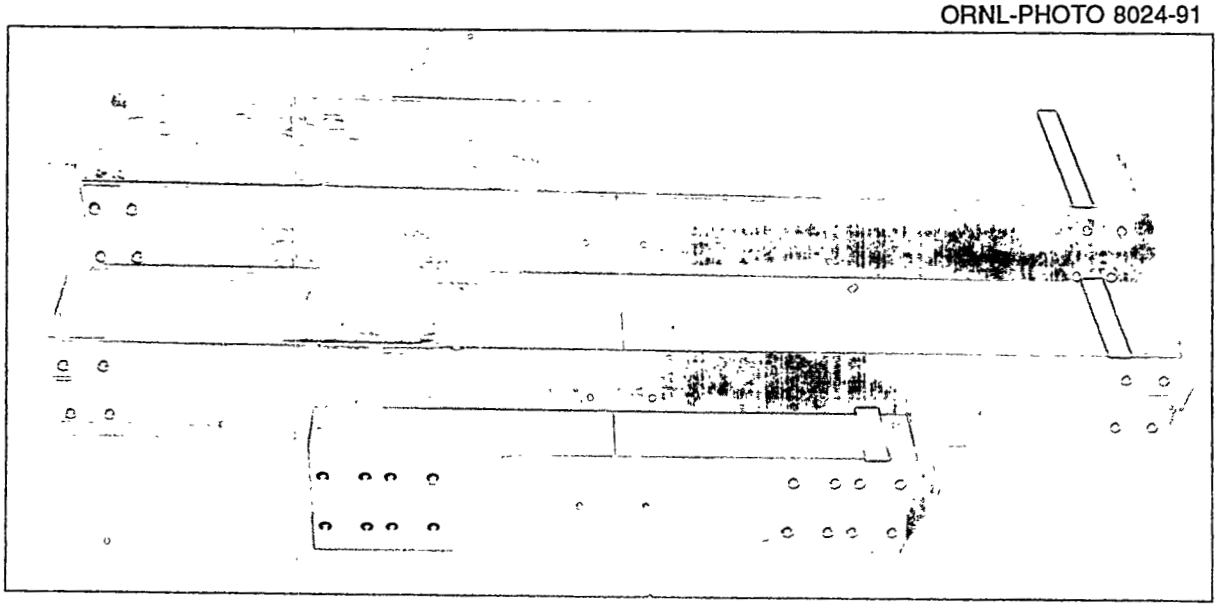

Figure 1.1 The 100-mm deep beams used in shallow-flaw test program to permit full-scale testing of surface flaws having depths in the range that PTS analysis has shown to be the controlling range for crack initiation

ORNL-PHOTO 8318-92

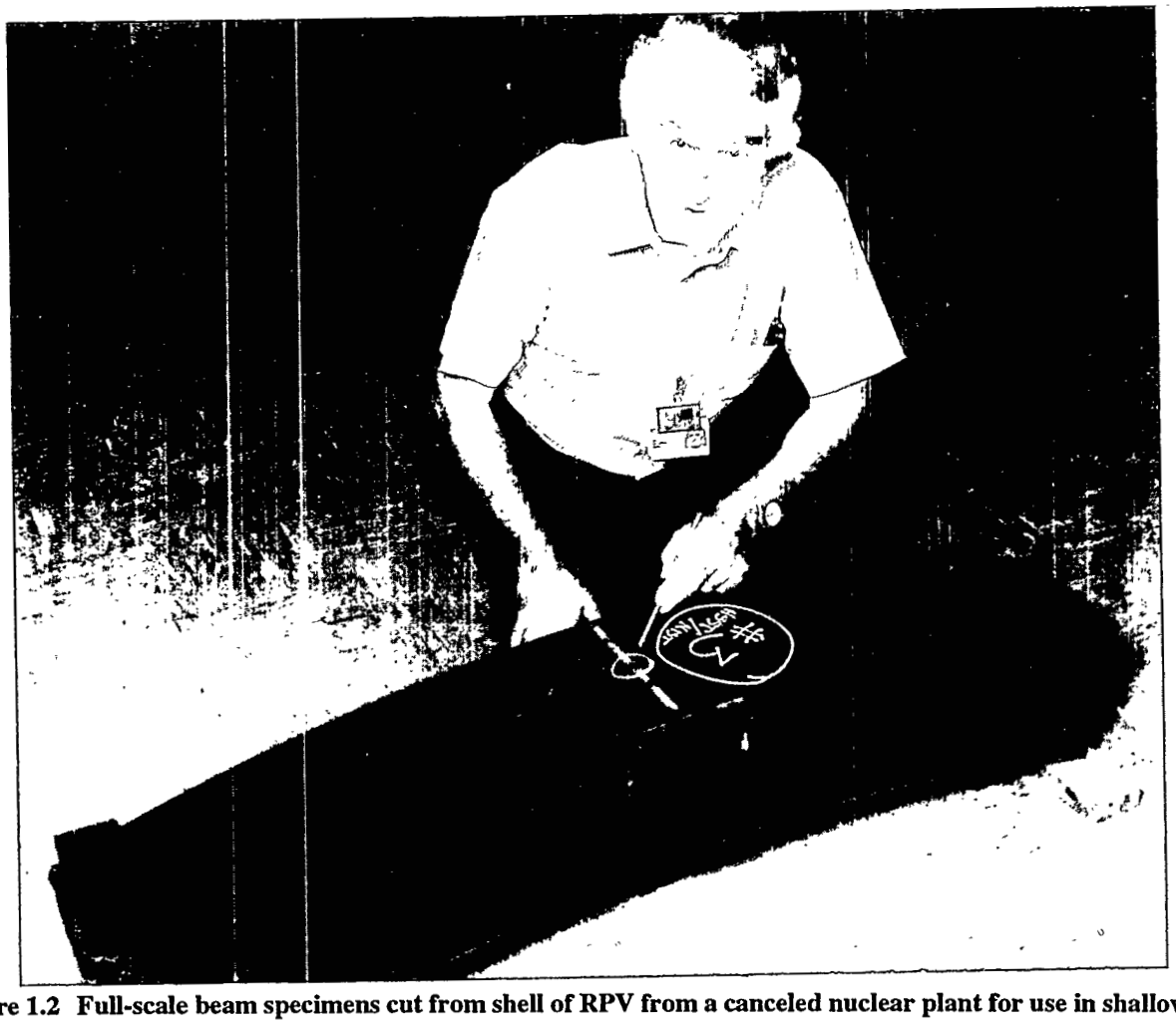

Figure 1.2 Full-scale beam specimens cut from shell of RPV from a canceled nuclear plant for use in shallow-flaw test program

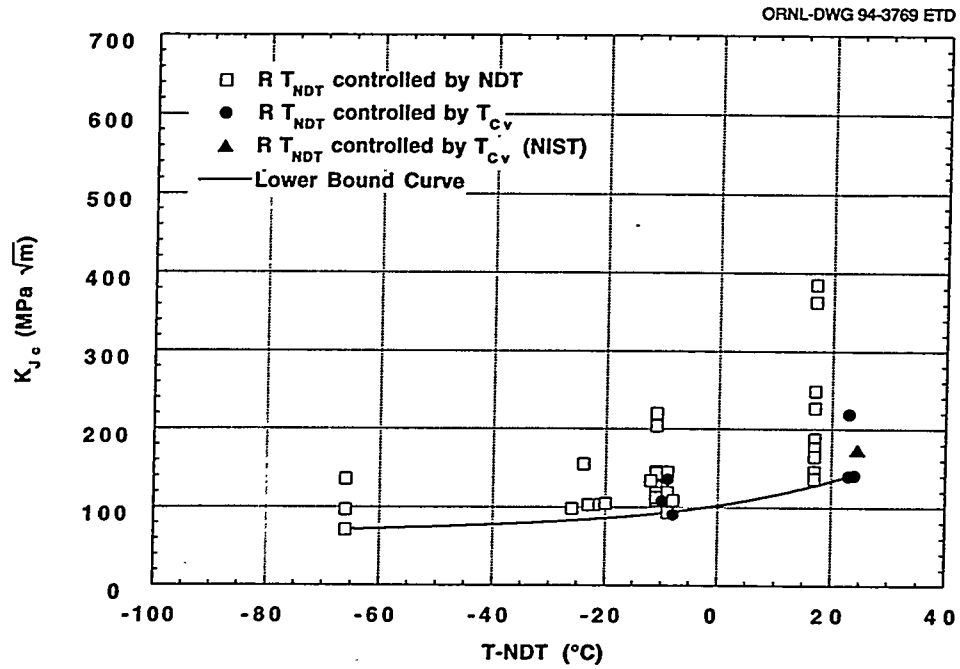

Figure 1.3 The parameter-controlling T – NDT has no significant effect on distribution of K_{Jc} vs T – NDT data points from deep-crack SENB A 533 B specimens, single curve adequately defines lower bound for combined data set

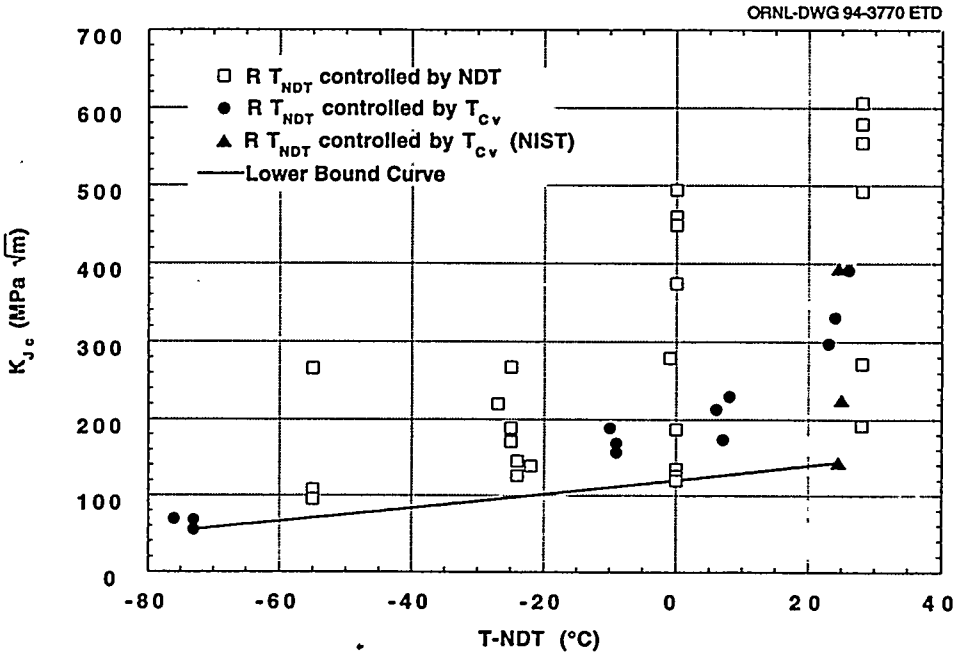

Figure 1.4 Shallow-flaw fracture toughness data for A 533 B plate and weld material form a single homogeneous group when plotted as function of the normalizing parameter T – NDT. Lower-bound curve of this data set is similar to that of deep-flaw data set, but shallow-flaw data set shows an increase in both mean toughness and data scatter

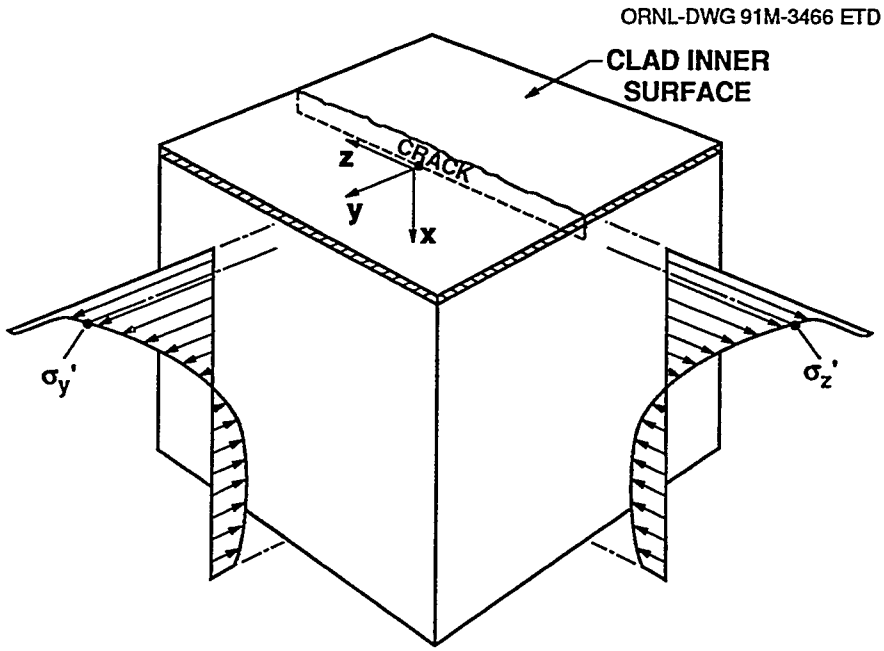

Figure 1.5 PTS loading produces biaxial stress in an RPV wall with one of the principal stresses aligned parallel with the tip of the constant-depth shallow surface flaw

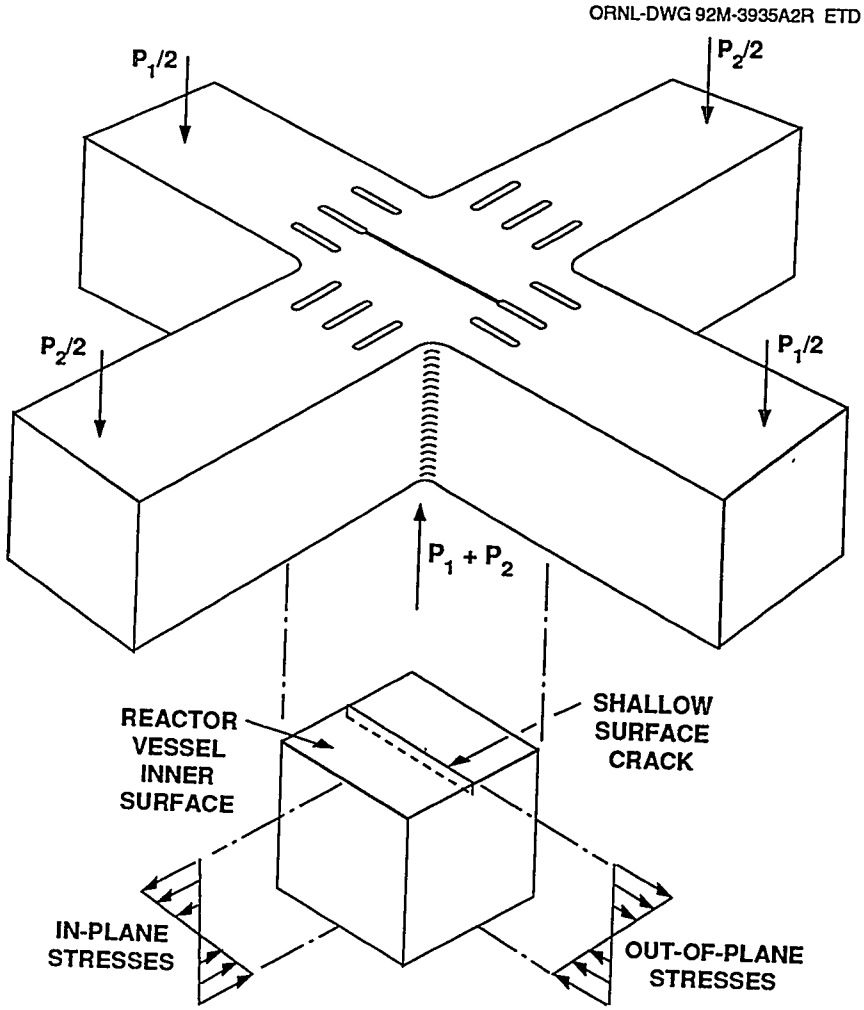

Figure 1.6 Conceptual features of cruciform flaw biaxial fracture-toughness test specimens

1.3 Dual-Parameter Correlations

Fracture in a brittle material occurs when the opening-mode tensile stresses at the tip of a crack exceed a critical value over a finite length.[6] Local yielding of the material at the crack tip limits the buildup of opening-mode stresses and thereby directly influences fracture toughness.

Crack-tip stress fields can be divided into hydrostatic and shear components. Yielding of the material is governed by the shear component of the stress field. Tensile hydrostatic stresses contribute directly to the crack-tip opening-mode tensile stresses but do not influence yielding. It follows, therefore, that fracture toughness will be directly influenced when the hydrostatic component of the crack-tip stress field increases.

Crack-tip constraint is the term used to describe conditions that influence the hydrostatic component of the crack-tip stress field. Low constraint reduces the hydrostatic stress contribution to the opening-mode stress and thereby increases the fracture toughness relative to that obtained in a high-constraint configuration.

Dual-parameter, fracture-toughness correlations have been proposed to provide a quantitative assessment of the effects of reduced crack-tip constraint on fracture toughness. The existing dual-parameter methodologies being investigated within the HSST Program include stress-based fracture characterizations (i.e., J-Q methodology of O'Dowd and Shih[7,8] combined with Ritchie-Knott-Rice (RKR) fracture criteria[6] and the Dodds-Anderson constraint correction technique[9]) and stress-strain-based characterizations (i.e., plane-strain fracture ductility techniques of Clausing,[10] Barsom,[11] Merkle,[12] Tetleman and McEvily,[13] and others). Determinations are being made concerning the bounds of applicability of the existing constraint effects correlation methodologies (i.e., how effective are they in matching existing data?). Evaluations that utilized applications of the stress-based correlations (i.e., J-Q and an engineering model[14] derived from the Dodds-Anderson methodology) were described in Ref. 5. Additional evaluations are described herein based on applications of two models to the ORNL cruciform specimen (Fig. 1.6), namely, the original formulation of the Dodds-Anderson scaling model[9] and an ORNL/HSST strain-based model,[15*] incorporating plastic zone width in the crack plane as a second parameter.

*W. E. Pennell and W. R. Corwin, "Reactor Pressure Vessel Structural Integrity Research," Proceedings of the U.S. Nuclear Regulatory 22nd Water Reactor Safety Information Meeting, NUREG/CP-0140, in publication.

1.4 Biaxial Testing Program and Fracture Model

The following chapters describe results from a recent phase of the HSST testing program devoted to biaxial stress effects on fracture toughness. Chapter 2 provides a detailed summary of the testing program, including a description of the test specimen and experimental results obtained from the test matrix. Analysis of the test data, which includes a description of the modeling techniques and comparisons of test data and analytical results, is included in Chap. 3. Chapter 4 presents an evaluation of various dual-parameter fracture-toughness correlations based on applications to fracture-toughness data obtained from the biaxial testing program. Finally, a summary and some conclusions regarding the biaxial testing program and constraint methods development in the transition temperature region are given in Chap. 5.

References

1. T. H. Theiss and D. K. M. Shum, Martin Marietta Energy Systems, Inc., Oak Ridge National Laboratory, "Experimental and Analytical Investigation of the Shallow-Flaw Effect in Reactor Pressure Vessels," USNRC Report NUREG/CR-5886 (ORNL/TM-12115), July 1992.*

2. J. A. Keeney, B. R. Bass, W. J. McAfee, and S. K. Iskander, Martin Marietta Energy Systems, Inc., Oak Ridge National Laboratory, "Preliminary Assessment of the Fracture Behavior of Weld Materials in Full-Thickness Clad Beams," USNRC Report NUREG/CR-6228 (ORNL/TM-12735), October 1994.*

3. R. E. Link and J. A. Joyce, "Experimental Investigation of Fracture Toughness Scaling Models," *Constraint Effects in Fracture: Theory and Applications*, M. Kirk and A. Bakker, eds., ASTM STP 1244, 1994.†

4. T. J. Theiss et al., Martin Marietta Energy Systems, Inc., Oak Ridge National Laboratory, "Initial Results of the Influence of Biaxial Loading on Fracture Toughness," USNRC Report NUREG/CR-6036 (ORNL/TM-12349), June 1993.*

5. B. R. Bass, J. W. Bryson, T. J. Theiss, and M. C. Rao, Martin Marietta Energy Systems, Inc., Oak Ridge National Laboratory, "Biaxial Loading and Shallow Flaw Effects on Crack-Tip Constraint and Fracture

Toughness," USNRC Report NUREG/CR-6132 (ORNL/TM-12498), January 1994.*

6. R. O. Ritchie, J. F. Knott, and J. R. Rice, "On the Relationship Between Critical Tensile Stress and Fracture Toughness in Mild Steel," *J. Mech. Phys. Solids* 21, 395–410 (1973).†

7. N. P. O'Dowd and C. F. Shih, "Family of Crack-Tip Fields Characterized by a Triaxiality Parameter: Part 1– Structure of Fields," *J. Mech. Phys. Solids* 39, 989–1015 (1991).†

8. N. P. O'Dowd and C. F. Shih, Brown University, "Two-Parameter Fracture Mechanics: Theory and Applications," USNRC Report NUREG/CR-5958 (CDNSWC/SME-CR-16-92), February 1993.*

9. R. H. Dodds, Jr., T. L. Anderson, and M. T. Kirk, "A Framework to Correlate a/W Ratio Effects on Elastic-Plastic Fracture Toughness (Jc)," *Int. J. Fract.* 48, 1–22 (1991).†

10. D. P. Clausing, "Effect of Plastic-Strain State on Ductility and Toughness," *Int. J. Fract. Mech.* 6(1) (March 1970).†

11. J. M. Barsom, "Relationship Between Plane-Strain Ductility and K_{Ic} for Various Steels," *J. Eng. Ind.* (November 1971).†

12. J. G. Merkle, Martin Marietta Energy Systems, Inc., Oak Ridge National Laboratory, "An Elastic-Plastic Thick-Walled Hollow Cylinder Analogy for Analyzing the Strains in the Plastic Zone Just Ahead of a Notch Tip," ORNL/TM-4071, January 1973.*

13. A. S. Tetleman and A. J. McEvily, Jr., *Fracture of Structural Materials*, John Wiley & Sons, Inc., New York, 1967.†

14. R. H. Dodds, C. F. Shih, and T. L. Anderson, University of Illinois, "Continuum and Micromechanics Treatment of Constraint in Fracture," UILU-ENG-92-2014, November 1992.†

15. W. E. Pennell, "Heavy-Section Steel Technology Program: Recent Developments in Crack Initiation and Arrest Research," *Nucl. Eng. Des.* 255–266 (1993).†

*Available for purchase from National Technical Information Service, Springfield, VA 22161.
†Available in public technical libraries.

2 Load-Ratio Test Program

The ORNL/HSST biaxial test program was initiated in FY 1992. The effort was basically divided into two phases. In Phase I, the specimen and test facility were designed, fabricated, and shakedown tests were performed to demonstrate proper function. Five specimens, BB-1 through BB-5, were fabricated and tested to demonstrate that a viable biaxial fracture-toughness specimen had been developed. Two biaxial loading ratios (ratio of transverse load to longitudinal load), 0:1 and 0.6:1, were investigated in Phase I. In Phase II, four additional specimens, BB-7, -9, -10, and -11, were fabricated and tested to extend the Phase I matrix to include a biaxial ratio of 1:1. While some details of these efforts have been reported previously,[1–3] all elements of the experimental effort are described herein to provide a unified presentation of the load-ratio test program and results.

2.1 Description of Test Specimen

2.1.1 Specimen Design

A number of basic requirements were established for a specimen to generate biaxial fracture-toughness data in the transition temperature range. First, the specimen should be capable of reproducing the essential features of the PTS loading condition. A beam-type cruciform specimen has this capability by generating a linear approximation of the nonlinear, through-thickness, biaxial stress distribution developed during PTS loading. Second, the specimen should permit clear separation and interpretation of any biaxial effect on shallow-flaw fracture toughness considering the scatter normally associated with fracture-toughness data. Again, a beam-type cruciform specimen provides this capability because the biaxial load ratio can be varied with no other change in test parameters. Third, the specimen should be economical in material usage, in fabrication costs, and in test preparation and execution. These requirements led to identification of the following specimen criteria:[1]

1. Specimen fabrication should be relatively simple and economical.
2. The quantity of fully characterized test material required should be small.
3. The crack-driving forces and out-of-plane biaxial stress fields similar to those of an RPV should be achievable.
4. The specimen must accommodate a through-crack assumption compatible with present NRC Regulatory Guide 1.154 (Ref. 4). The use of a through-crack simplifies the investigation of out-of-plane constraint effects.
5. The crack-driving forces should be relatively uniform over a substantial portion of the crack front.
6. The specimen should be amenable to testing in a uniaxial or biaxial configuration, with all other parameters unchanged.
7. Loading conditions should be unambiguously defined, that is, statically determinant.

While several test specimen configurations have the potential for satisfying these criteria, a beam-type cruciform specimen was selected as being the most readily implemented. The basic specimen design is shown schematically in Fig. 2.1. The specimen is in the shape of a cruciform with test section dimensions of 9.1-mm thickness, 102-mm length, and 102-mm width ($3.6 \times 4.0 \times 4.0$ in.) with a straight through-flaw of uniform depth [102 mm (0.4 in.)] in a plane perpendicular to the longitudinal direction of the beam. Note that the longitudinal direction was identified as the maximum load direction for this series of tests. The overall length of the specimen is 660 mm (26 in.) with an active beam length of 610 mm (24 in.).

A unique feature of the specimen is the configuration of the slots machined into each beam arm as shown in Fig. 2.1. These load diffusion control slots (LDCS) serve to minimize diffusion of the load applied by one set of beam arms into the material of the adjacent beam arms. Referring to Fig. 2.1, the LDCS are able to open freely, providing greater flexibility (less constraint) in the direction normal to their length while retaining essentially all the beam arm stiffness in the direction parallel to their length. Thus, the stresses caused by bending moments applied in one loading plane are less affected by the constraint of the beam arm normal to that loading plane. With uniformly distributed stresses, the flaw tip is then loaded uniformly over most of its length. The flaw-tip stress intensity distributions generated under different loading conditions are discussed in Chap. 3.

Four different LDCS configurations were considered before selecting a final specimen design[1] (see Fig. 2.2). Only three of these were actually implemented into test specimens. These geometries involved positioning of the inner end of the center LDCS relative to that of the adjacent, outer slots to minimize peak stress intensity (K) values and stress concentrations near the ends of the test flaw, that is, where the test flaw intersected the end of the center LDCS. Three-dimensional (3-D) finite-element analyses (FEA) demonstrated that positioning the inner end of the center LDCS at different distances from the specimen, midplane from that of the outer LDCS, was essential to controlling the peak values of K at the flaw/LDCS intersection.

Load-Ratio

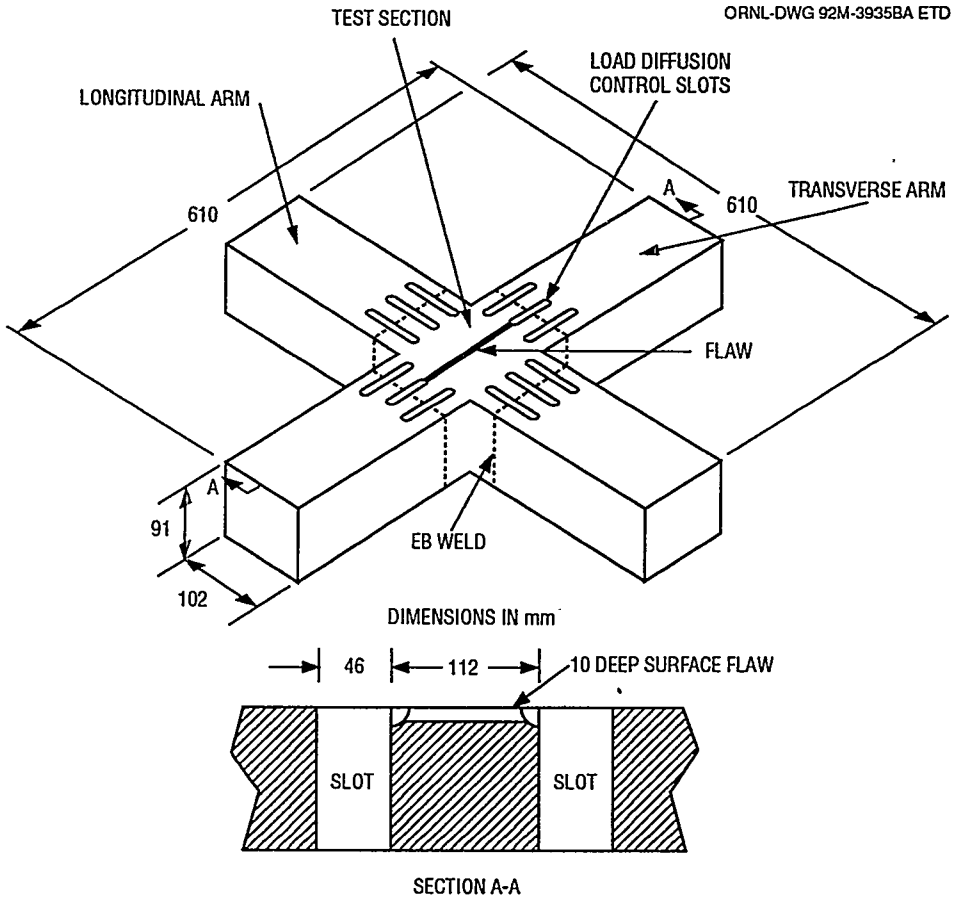

Figure 2.1 Typical cruciform beam test section for specimens tested in Phase I

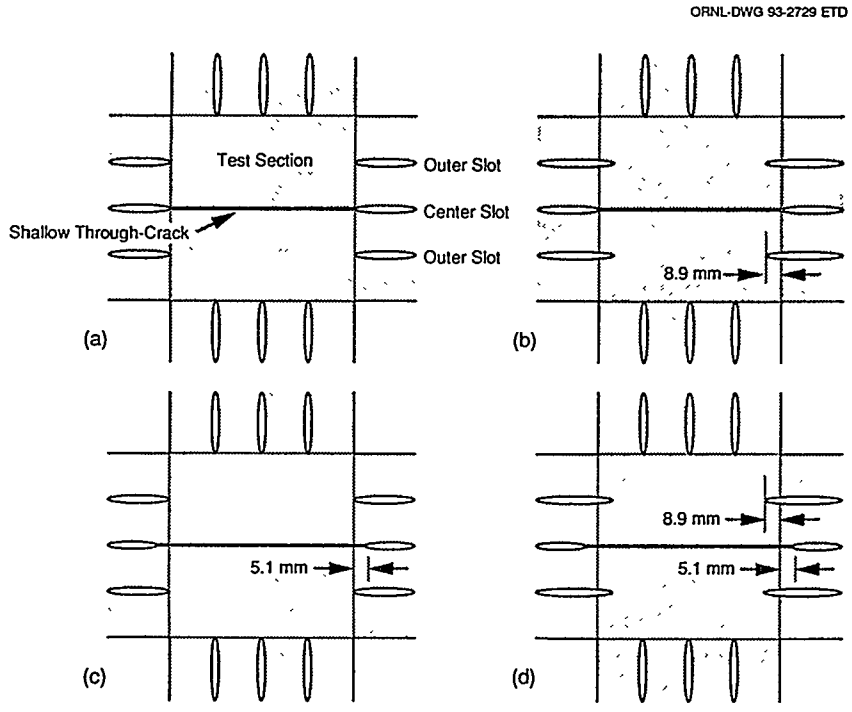

Figure 2.2 Slot configurations used in analyses of cruciform bend specimen: (*a*) uniform slots on test section boundary, (*b*) outer slots extended inward by 8.9 mm across test section boundary, (*c*) center slot contracted away by 5.1 mm from test section boundary, and (*d*) superposition of configurations (*b*) and (*c*)

Results from the design FEA are shown in Figs. 2.3–2.6. These figures show plots at different longitudinal load levels for the variation of K_J vs distance from the specimen centerline. Note that K_J is the elastic-plastic stress-intensity factor determined from J-integral values. It was found that for slot configuration (*a*) under a biaxial load ratio of 0.5:1, a large peak K_J existed at the flaw/LDCS intersection (Fig. 2.3). Extending the outer slots toward the specimen midplane, configuration (*b*), elevated K_J at the specimen midplane while significantly reducing the peak behavior at the flaw/LDCS intersection. It was observed, however, that a large opening-mode stress concentration still existed at the flaw/LDCS intersection. Under 0.6:1 biaxial loading, configuration (*c*) exhibited a further reduction in the tendency for K_J to peak at the flaw/LDCS intersection (Fig. 2.5), while this peak was completely removed in configuration (d) (Fig. 2.6). In addition, in configuration (*d*) there is only a moderate variation in K_J over the center half of the flaw front for the full range of applied loading. Configuration (*d*) was selected as the reference geometry for the biaxial specimen and, as discussed in Sect. 2.3, the behavior predicted by the analysis was verified through testing.

2.1.2 Specimen Fabrication

For the series of development tests, it was desired to use material with extensive prior characterization through fracture testing. The test sections were fabricated from a heat of A 533 grade B class 1 steel that had previously been used in the HSST wide-plate[5,6] and shallow-crack[7] test programs. The broken halves of the shallow-crack beam specimens had a maximum width of 150 mm (6 in.). For Phase I, after some refinement of the design, the test sections were machined into the configuration shown in Fig. 2.7, including the LDCS and the test flaw. A completed test section is shown in Fig. 2.8. The flaw was machined using a single-pass wire electron-discharge-machining (EDM) process, resulting in a flaw width at the surface of ~0.3 mm (0.012 in.), tapering to a root radius of ~0.15 mm (0.006 in.). The flaw was cut to a uniform depth of 10 mm (0.4 in.), resulting in a two-dimensional (2-D) shallow flaw with no surface singularities because the flaw ends intersected the end of each center LDCS.

The two longitudinal beam arms were electron-beam (EB) welded to the test section to form a uniaxial beam configuration. The EB welding procedure has been used extensively in companion test programs. It has been shown to provide a reliable structural joint with distortion levels low enough that, with accurate initial alignment, only cleanup of the EB weld bead at the surface is required to maintain the specified tolerances on specimen straightness and flatness. In addition, there is minimum heat input to the test piece with a relatively small heat-affected zone (HAZ).

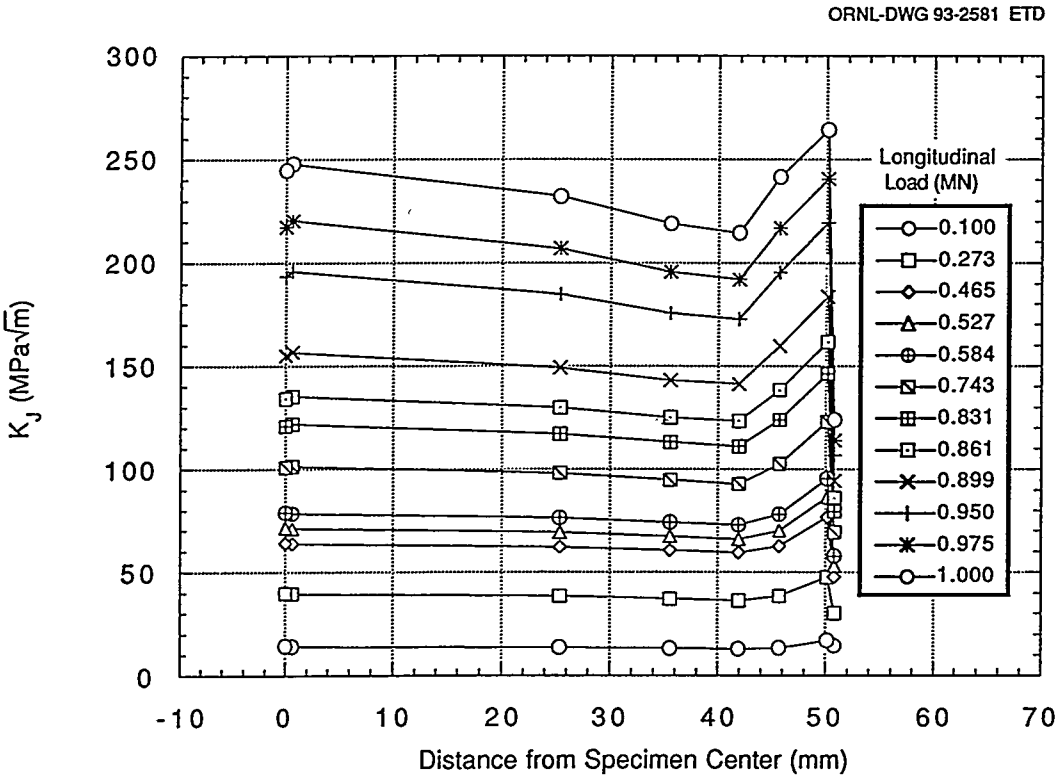

Figure 2.3 Distribution of K_J vs distance along crack front as function of applied longitudinal load for biaxial loading ratio of 0.5:1 applied to HSST cruciform bend specimen with slot configuration (*a*) in Fig. 11

Load-Ratio

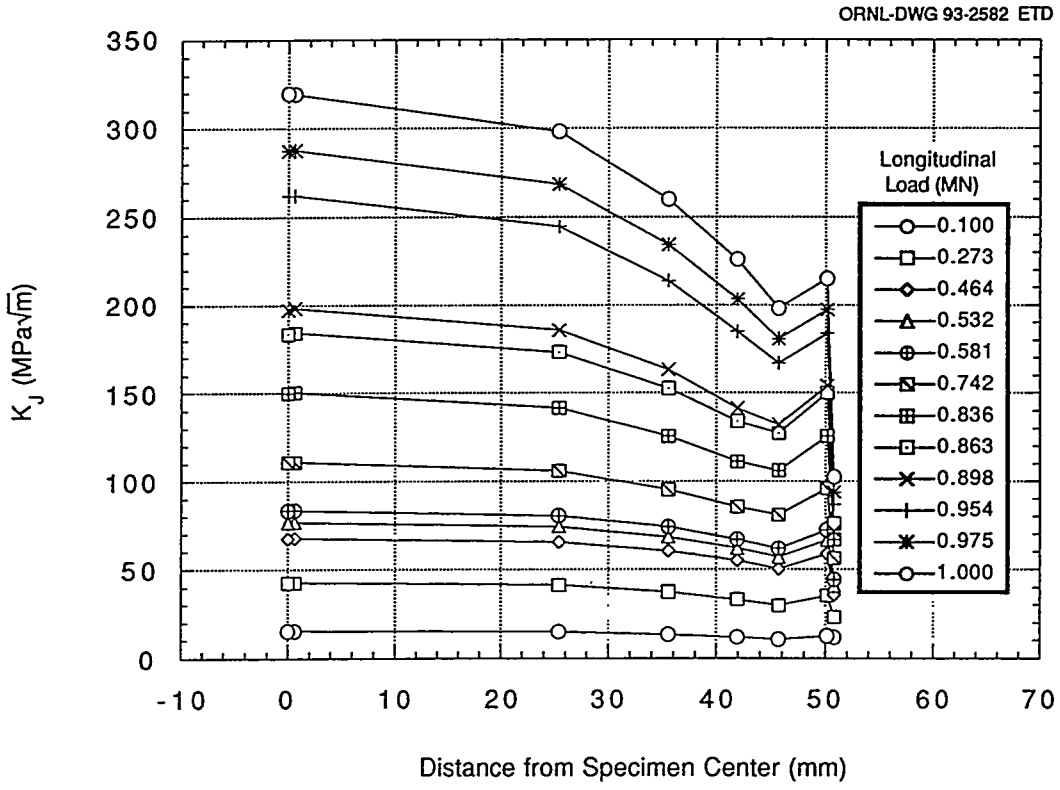

Figure 2.4 Distribution of K_J vs distance along crack front as function of applied longitudinal load for biaxial loading ratio of 0.5:1 applied to HSST cruciform bend specimen with slot configuration (*b*) in Fig. 11

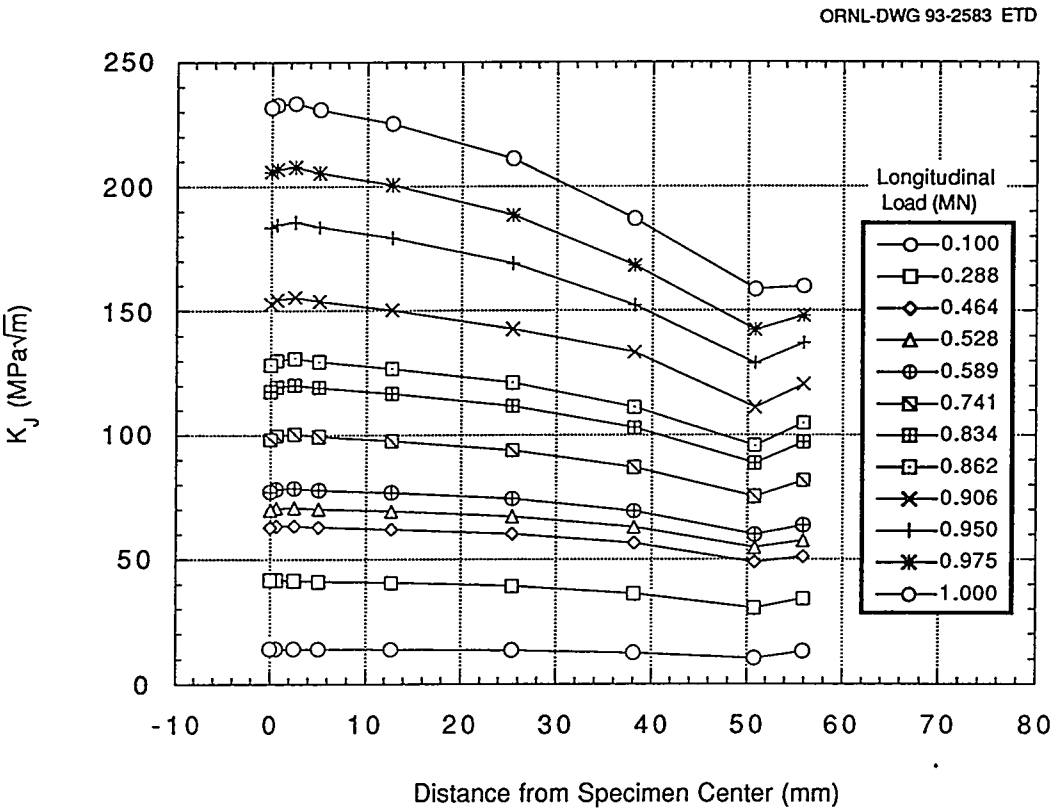

Figure 2.5 Distribution of K_J vs distance along crack front as function of applied longitudinal load for biaxial loading ratio of 0.6:1 applied to HSST cruciform bend specimen with slot configuration (*c*) in Fig. 11

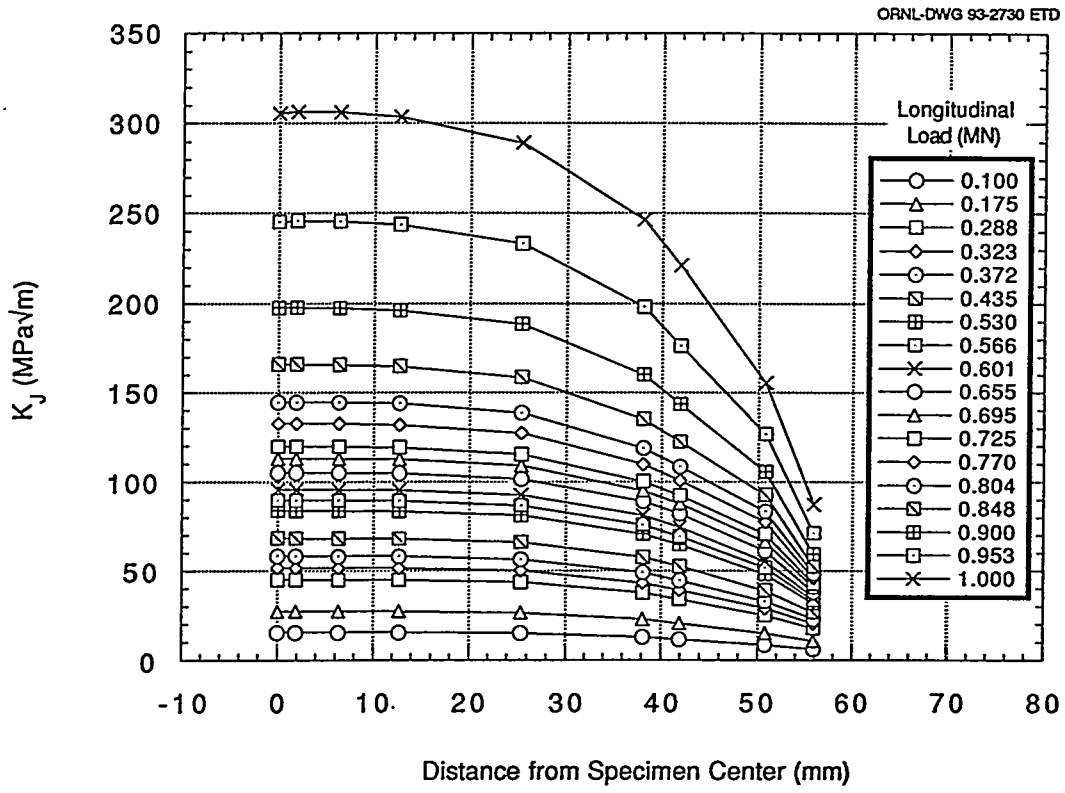

Figure 2.6 Distribution of K_J vs distance along crack front as function of applied longitudinal load for biaxial loading ratio of 0.6:1 applied to HSST cruciform bend specimen with slot configuration (*d*) in Fig. 11

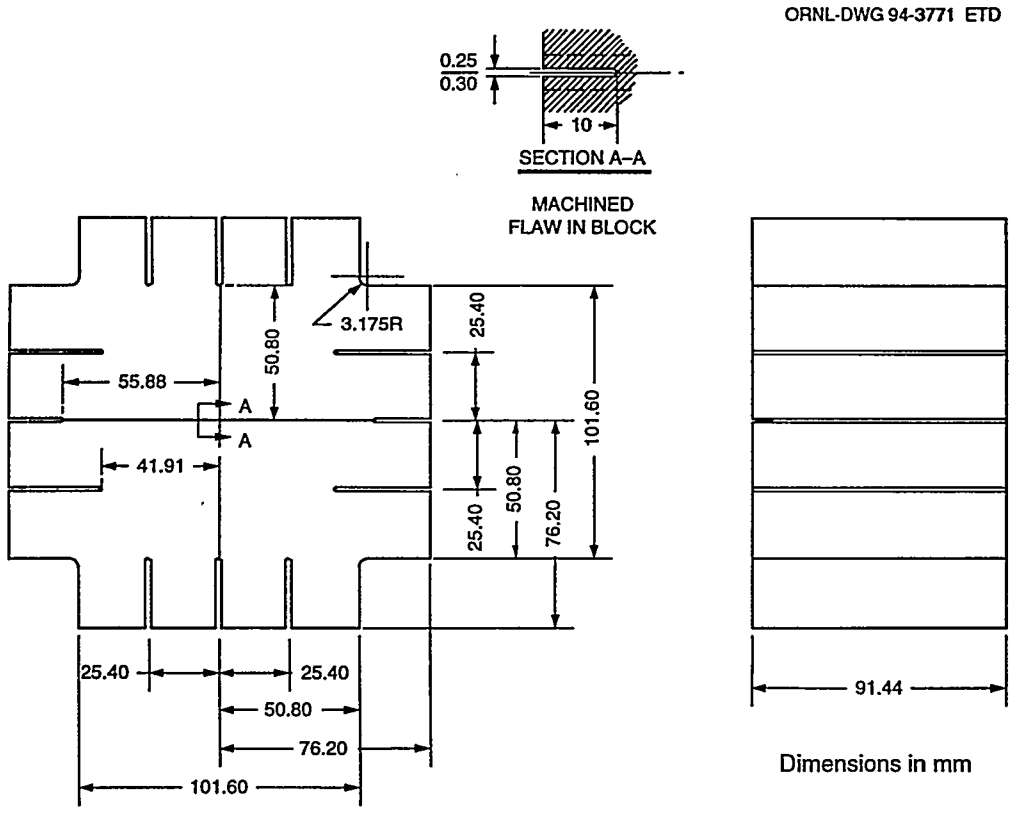

Figure 2.7 Schematic of final test section design used in Phase I tests

Load-Ratio

PHOTO YP15591

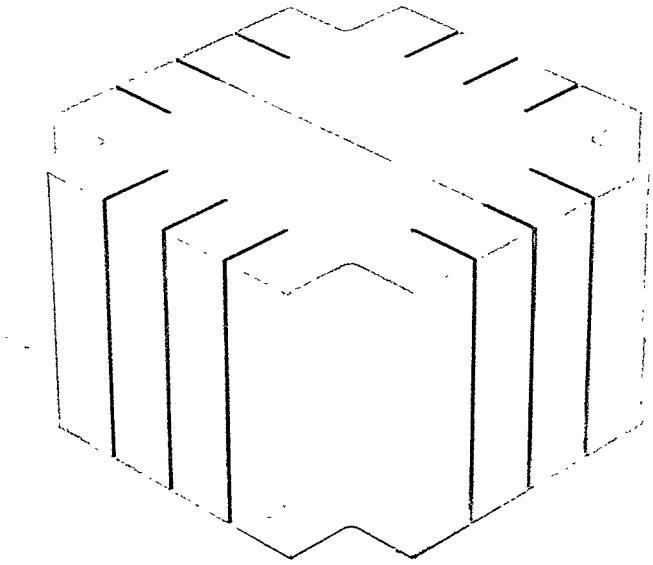

Figure 2.8 Cruciform beam test section of configuration used in Phase I testing

This feature prevents any modification of test section material properties. The beam was fatigue precracked in four-point bending using a change in compliance technique to determine flaw growth. The transverse beam arms were EB welded in place, and the beam was final machined to remove these EB weld beads. A completed cruciform test specimen assembly is shown in Fig. 2.9. As part of the final machining, a mechanical milling operation was used to remove any EDM embrittled material and any fatigue-crack-growth irregularities from the center LDCS/machine flaw intersection. This feature is shown in Fig. 2.1 as the semicircular cutouts at each end of the flaw.

In this test specimen design, the test section was the only portion fabricated from the fully characterized material. The beam arms were fabricated from a more generally available A 533 material and were designed to be reusable.

PHOTO YP15592

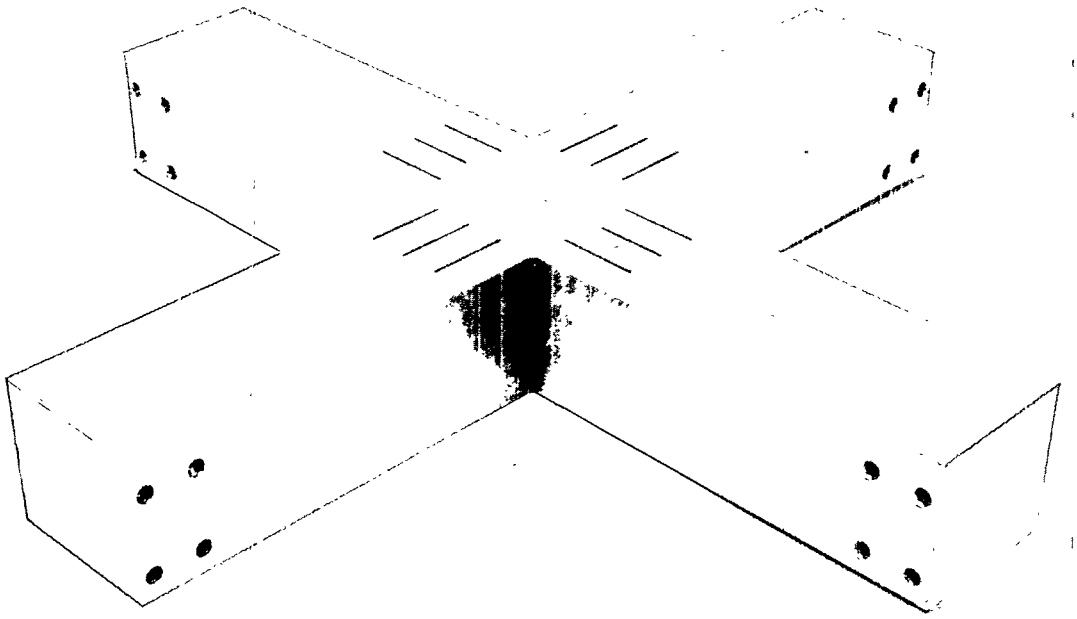

Figure 2.9 Completed cruciform beam specimen showing location details of LDCS and test flaws

This procedure proved to be economical in both material usage and in fabrication costs.

Referring to Fig. 2.1, it can bee seen that the design of the specimens tested in Phase I placed the EB welds joining the test section and beam arms at the midlength of the LDCS. This was dictated by the 152-mm-wide (6-in.) size of the material available for Phase I specimen fabrication. This area is one of high-stress loading. For the Phase II specimens where more stock material was available, the design was modified by lengthening the test section extensions and completely enclosing the LDCS. This modification moved the EB weld into a region of homogeneous material and resulted in the configuration shown in Fig. 2.10. All other test section dimensions and fabrication sequences were retained to be the same as those of Phase I.

2.2 Test Facility and Data Acquisition

2.2.1 Loading System

The primary functional requirement for the test facility was that it have the capability for applying either uniaxial (four-point bending) or biaxial (eight-point bending) configurations to achieve the desired biaxial loading ratios and that the load reaction system be statically determinant. A statically determinant system provides simplicity because a complex computer-controlled system of load actuators is not needed. By its function, the loads applied to each beam arm are determined from static equilibrium.

A schematic of the loading system and the cruciform beam interface is shown in Fig. 2.11. The loading fixture is mounted in an INSTRON 2.47-MN (550-kip) servo-hydraulic test machine. The compass points shown in Fig. 2.11 are used for reference and define the orientation of the fixture in the test machine. The specimen is loaded by the test machine actuator with the vertical line of force being directly through the center of the test section. The applied load is reacted at the ends of the beam arms by means of one fixed support and three matched hydraulic cylinders with 534-kN (120-kip) capacity each. The interface between the actuator and the specimen is a spherical seat, which ensures that resisting overturning moments are not introduced into the specimen. The applied load is transmitted to the test section through a flat, square seat that fits directly beneath the test section's central 100- by 100-mm (4- by 4-in.) region. Thus, as the specimen

PHOTO YP19572

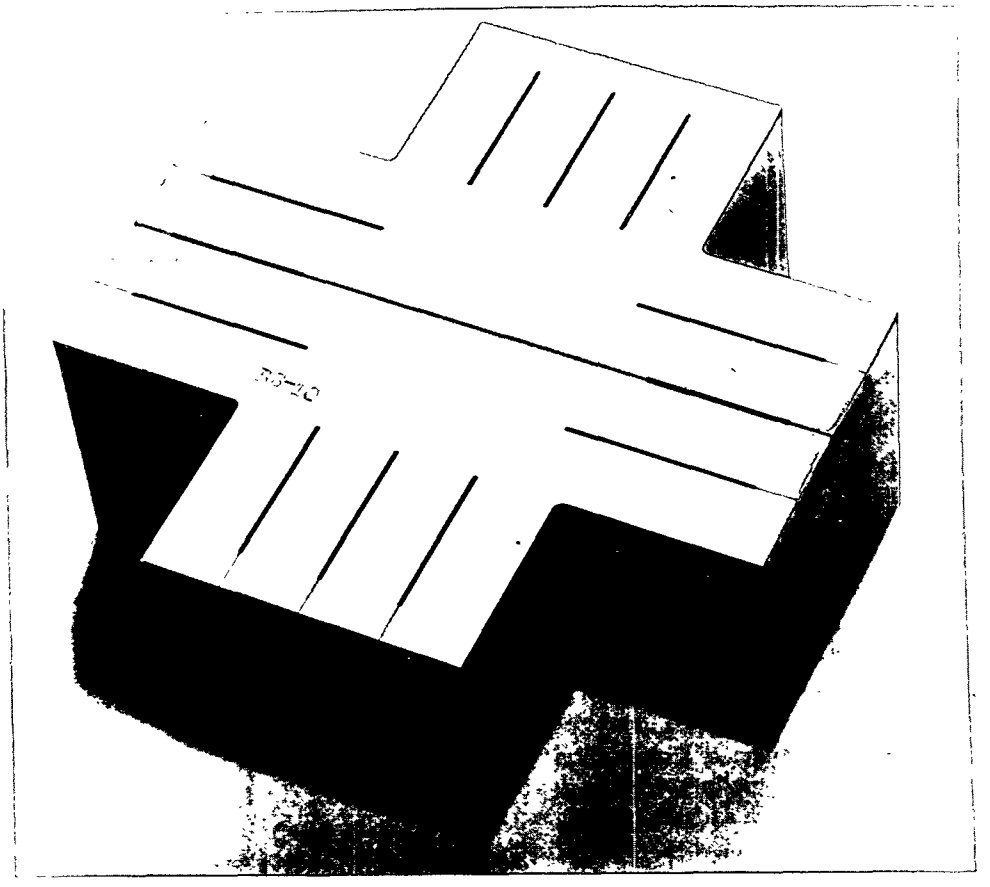

Figure 2.10 Test section configuration used for Phase II cruciform specimens showing lengthened extensions that completely contain the LDCS

Load-Ratio

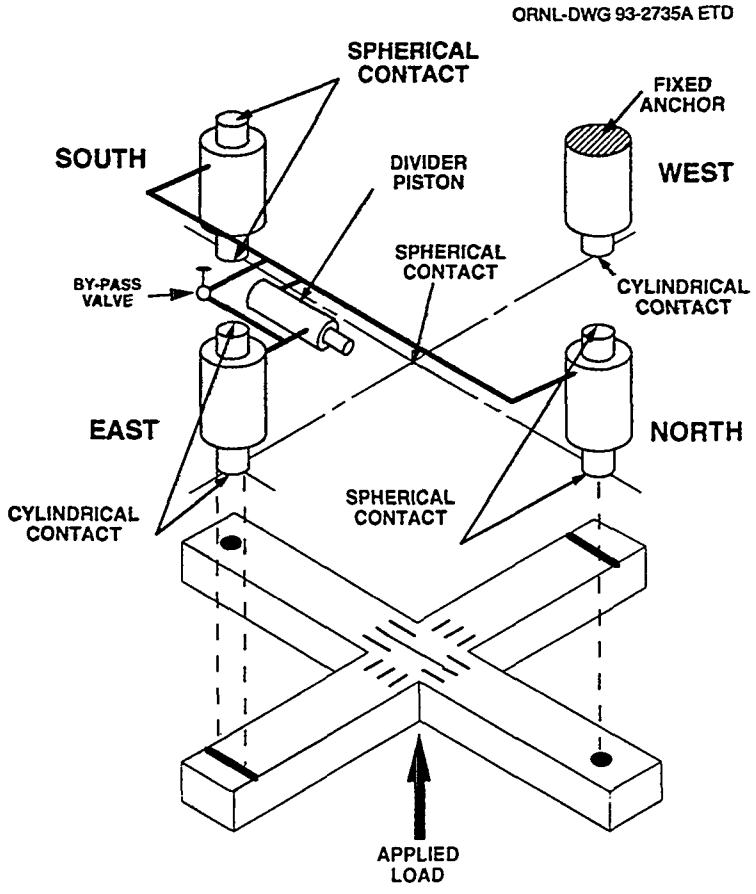

Figure 2.11 Schematic of biaxial loading fixture showing interface of load points with test specimen

deflects under load, the test section is bent into two orthogonal cylindrical surfaces that contact the load seat along its outer edges. For the general loading case, the specimen is then tested under eight-point loading rather than five-point loading, which might be construed from the schematic shown in Fig. 2.11.

The longitudinal loading plane is defined by the west fixed anchor, the central applied load point, and the east reaction cylinder (see Fig. 2.11). The fixed anchor is rigidly mounted to the test fixture upper platen and, in conjunction with the test machine actuator, provides horizontal stability for the specimen. To ensure stability and positional control, cylindrical contact points are used between the specimen and the anchor and at each end of the east hydraulic cylinder support. The specimen can then be tested in a uniaxial configuration (east-west) with a completely stable load and support system. The transverse loading plane is defined by the north reaction cylinder, the central applied load point, and the south reaction cylinder. Spherical contact points are used at both upper (platen) and lower (specimen) ends of these cylinders and, in conjunction with the spherical seat at the actuator, offer no resisting moment to planer alignment of the specimen during a test.

The three hydraulic cylinders and the anchor passively react the applied load. The cylinders are connected through a closed manifold system that contains a bypass valve and a divider piston. The manifold contains a constant volume of oil during a test. The manifold can be reconfigured to achieve different biaxial load ratios. For example, if the divider piston is fully bypassed, each cylinder reacts the same load because each is subjected to the same internal pressure. The load on the fixed anchor is then known from the equations of static equilibrium and is equal to the force exerted by each piston. This results in 1:1 biaxial loading. The uniaxial (0:1) load case is achieved by bypassing the north-south side of the manifold such that the applied load is reacted by the east-west reaction points only. When biaxial ratios other than 0:1 or 1:1 are desired, the north-south pistons are connected to the east piston through a divider piston as shown in Figs. 2.11 and 2.12. The divider piston is a standard, double-acting, hydraulic cylinder with a low- to high-pressure piston face area ratio that approximates the desired load ratio. Ignoring friction in the piston/cylinder seals, no external forces are acting on the divider piston. Static equilibrium then requires that the forces acting on the opposing face of the piston be equal. The effect of atmospheric pressure can be ignored also because the additional force introduced is insignificant. A reaction

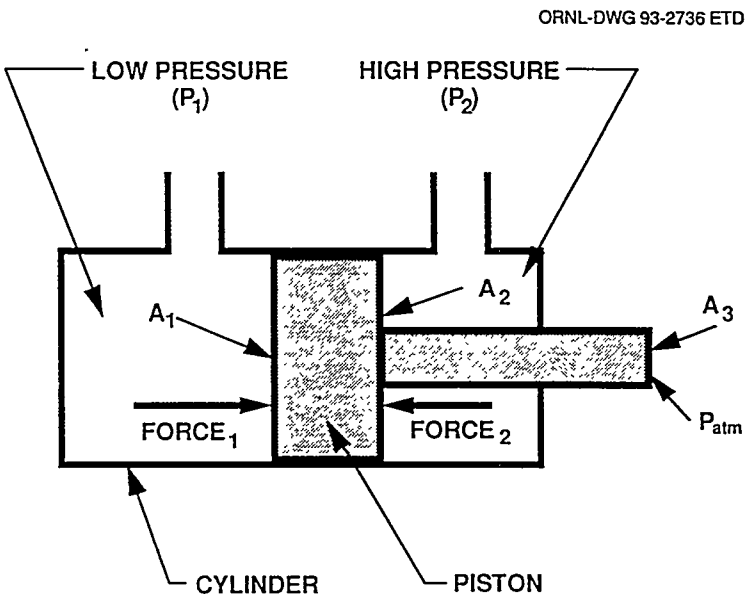

Figure 2.12 Section of biaxial test fixture divider piston used to achieve proportional biaxial loading

force ratio results that is inversely proportional to the divider piston area ratio.

Preliminary analyses indicated a high probability of a biaxial loading effect on fracture toughness under 0.5:1 biaxial loading. A double-acting piston with an area ratio near 0.6 was selected for this series of tests because this was a low-cost, standard off-the-shelf item. The divider piston was set up so that the east cylinder was connected to the high-pressure side of the manifold (divider piston). This configuration resulted in the maximum load being applied in the east-west plane.

Calibration tests were performed using a homogeneous beam (no flaw) machined to the dimensions of the cruciform specimen shown in Fig. 2.9. The calibration beam was fully instrumented using foil-type surface strain gages applied to the central test section and to all four beam arms. The primary purpose of the tests was to demonstrate that the loading system applied the specified forces to the test section and that the test section, in the absence of a flaw, deformed consistent with the applied forces and boundary conditions. The calibration beam was loaded successively with biaxial load ratios of 0:1, 0.6:1, and 1:1 to load levels less than the elastic limit load, and measurements of beam arm and test section strains were made.

Figure 2.13 shows the beam arm strains measured for each of the above load cases, together with results from elastic calculations of the expected response. Figure 2.13(*a*) presents results for the uniaxial case and shows complete agreement between the strains measured on the east and the west beam arms. This confirms that any resistance in the roller contact points and in the spherical seat at the applied load point is negligible, and the specimen is deforming under four-point bending with no induced in-plane loads. In addition, the plots are linear, indicating that small changes in geometry do not lead to redistribution in loading. Figure 2.13(*b*) shows the results for the 0.6:1 load case. Opposing beam arm strains agree very closely with one another, and the strain ratio (load ratio) remains essentially constant over the full range of loading. Figure 2.13(*c*) gives the results for the 1:1 biaxial case. In this case, each beam arm reacts the same load, which is reflected by the close agreement of the measured beam arm strains. While not shown, the test section behaved in a completely predictable manner for this configuration under four- and eight-point bending. Through these tests, the functionality of the test facility and the predicted behavior of the specimen configuration were verified.

2.2.2 Instrumentation and Test Procedures

Every specimen was fully instrumented with thermocouples, surface strain gages, potentiometers, and clip gages to measure test parameters for toughness evaluations and to verify proper loading and temperature distribution. Strain gages were used on both the test section and the beam arms. The general pattern of gages on the test section is illustrated in Fig. 2.14. These gages were used to evaluate the general response and the load distribution in the test section. After initial shakedown, two strain gages were installed on the top surface of each beam arm 177 mm (7 in.) from the test section geometric center. These gages provided verification of the applied biaxial loads. Because beam arm behavior was linear-elastic, the beam arm loads could be verified using simple beam formulas.

Load-Ratio

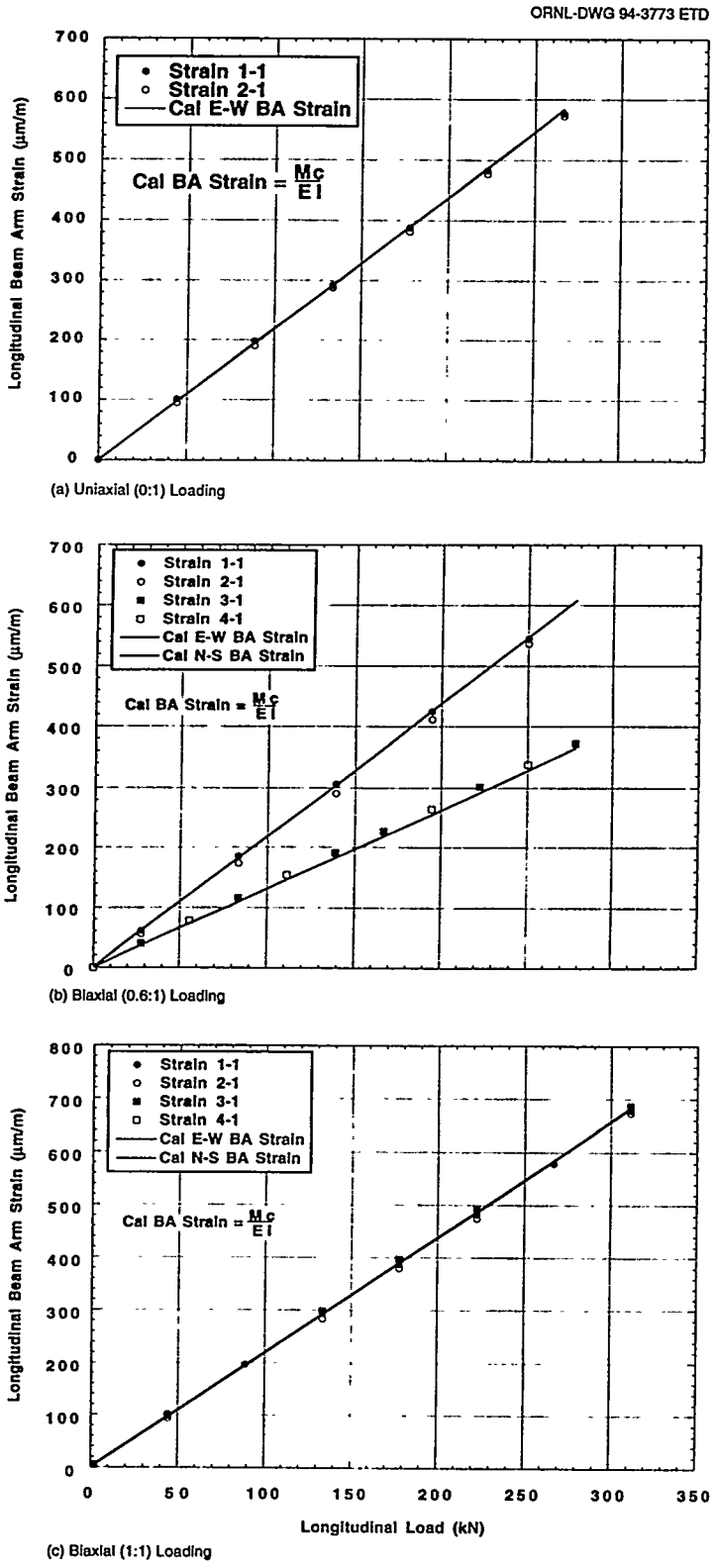

Figure 2.13 Schematic of biaxial loading fixture showing interface of load points with test specimen

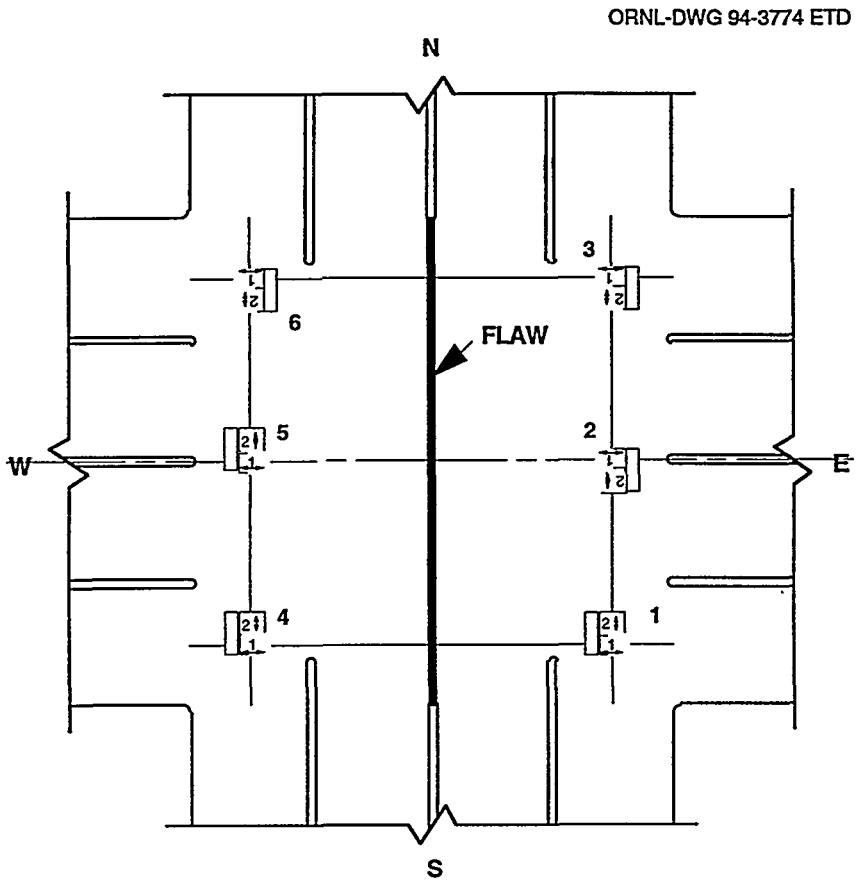

Figure 2.14 Pattern of strain gages used on test section of cruciform specimens

Potentiometers were located under the reaction points of each beam arm to measure load-line displacement (LLD). Because the only common point of reference for the orientation of the specimen was the spherical seat between the specimen and actuator, a spider arrangement was used to support the potentiometers. Each potentiometer was mounted on a cantilever arm that, in turn, was fixed to the central load seat above the actuator. This spider allowed measurement of the deflection of each beam arm relative to the test section without sensing rigid body rotations of the specimen. The LLD for a given plane of loading was taken as the average of the two potentiometers in that plane. One problem with use of these potentiometers was that a finite amount of travel was required to properly establish consistent readings. It was verified from other instrumentation output that this phenomenon was due to both a finite load required for proper initial seating of the specimen against the load points and by some dead space in the mechanical contacts in the potentiometers. This initial nonlinearity was removed by extrapolation of the data back to zero load.

Four clip gages were installed across the flaw mouth for each test to measure crack-mouth-opening displacement (CMOD). These gages were located on the specimen longitudinal centerline, 19 mm (0.75 in.) north and south of the centerline, and 38 mm (1.5 in.) south of the centerline (identified as "far south" gage). For each test, general agreement between the north, middle, and south clip was observed; this verified pretest analyses of essentially uniform loading across the center half of the width of the specimen and of symmetric loading of the specimen. The "far south" gage yielded measurements ~25% less than that of the centerline gage, which further validated specimen behavior as predicted by pretest analyses.

The specimen was cooled to the prescribed test temperature using liquid nitrogen (LN_2). A rectangular, 75-mm (3-in.) long and 100-mm (4-in.) wide hollow cup was mounted on the top of each beam arm ~89 mm (3.5 in.) from the center of the specimen. LN_2 was fed into these cups through a manifold system that permitted control of flow to each cup. During the Phase I tests, eight thermocouples were mounted on the specimen. These were located at each interior corner (as viewed from the top) of the test section, four near the top surface of the specimen and four near the bottom. The thermocouples were protected from direct LN_2 spray to ensure that consistent temperatures were measured during the tests. For the Phase II tests, reliable test procedures had been developed so that only the four thermocouples near the top surface were

needed, except for BB-9 where provisions were made for a fifth thermocouple on the bottom surface of the specimen.

For Phase I tests, examination of the thermocouple data for each test showed a steady rise in temperature measured at the bottom of the test section. In addition, results from the BB-2 test indicated a temperature rise at the top surface. A one-dimensional heat transfer analysis was performed to investigate the impact of these measurements on the temperature at the flaw tip. The analysis indicated that the temperature rise at the bottom surface had negligible impact on the temperature at the flaw tip. In addition, for tests with near isothermal conditions at the top surface, the flaw-tip temperature was adequately reflected by the top surface thermocouple measurements. For tests where the top surface temperatures were essentially constant, the flaw-tip temperature was taken as the average of the top surface thermocouple outputs. The transient analysis of the temperature increase in specimen BB-2 indicated that the average flaw-tip temperature was ~2°C cooler than the average top surface temperature. For tests of this type, the flaw-tip temperature was taken as lagging the top surface average by ~2°C. For verification of temperature distribution, a fractured specimen was instrumented with two additional thermocouples imbedded in the specimen at a depth approximating the flaw-tip depth. Measurements from this specimen confirmed that the average top surface temperature was very closely related to the flaw-tip temperature.

Before each test, the clip gages and potentiometers were mechanically calibrated at room temperature before being mounted on the specimen. The strain gages were calibrated using shunt resistors. Load and stroke outputs were also calibrated.

The specimen was mounted in the fixture and carefully aligned with the principal planes of loading. The hydraulic system was balanced, and the hydraulic cylinders were extended and aligned to ensure that each acted through the prescribed load point. A small preload was then applied to the specimen to hold this configuration. The LN_2 flow was started, and the specimen was cooled to the test temperature and held at constant temperature for a period up to 30 min to ensure isothermal conditions in the test section. The specimen was then loaded to failure at a constant displacement rate. After fracture, the remaining load was removed, and the test section was sprayed with a light oil to inhibit oxidation. When the specimen had warmed to room temperature, it was removed from the test machine and sectioned for fracture surface examination and analysis.

Five cruciform specimens were tested in Phase I of the program. An additional four were tested under the expanded load ratio investigation of Phase II. One of the primary objectives of Phase I was to develop and demonstrate a test specimen geometry suitable for the generation of biaxial fracture-toughness data. All specimens were tested at a nominal test temperature of –45°C (–49°F). The normalized test temperature ($T - RT_{NDT}$) was –10°C (–18°F) (Ref. 2).

2.3 Experimental Results

The LDCS configuration proved to be a major factor influencing the fracture initiation site location. The first specimen tested was specimen BB-1, LDCS configuration (*b*), under 0.6:1 biaxial loading. The CMOD and LLD responses for this specimen are shown in Figs. 2.15 and 2.16, respectively. Posttest examination of the fracture surface indicated that the fracture initiation site was only 2.5 mm from the corner formed by the intersection of the center LDCS and the test flaw. The general location of this fracture initiation site may be seen in Fig. 2.17. While the toughness value determined from this test was considered acceptable, there was concern that this particular configuration was overly susceptible to edge effects. LDCS configuration (*c*) was used for the next specimen, specimen BB-2, because analyses had indicated that the stress concentration at the LDCS/flaw corner would be reduced. Specimen BB-2 was tested under 0:1 uniaxial loading. The CMOD and LLD results for this test are shown in Figs. 2.18 and 2.19, respectively. The CMOD results were consistent with pretest predictions of the distribution across the flaw mouth, and the LLD results graphically exhibit the uniform bending achieved during test. The fracture initiation site for this specimen was ~20 mm from the north edge, as noted on Fig. 2.20. This location is not in a region of the peak K_J although the toughness value determined from the test results can be considered as valid. It did appear, however, that this configuration was still subject to adverse edge effects. The next specimen, specimen BB-3, was tested with the same LDCS configuration (*c*) but under biaxial 0.6:1 loading. This specimen failed exactly at the LDCS/flaw corner as is shown in Fig. 2.21 and was not considered in further assessments of cruciform results. It was concluded that configuration (*c*) could not be relied upon to yield consistently valid fracture results.

The next specimen tested, specimen BB-4, was modified to LDCS configuration (*d*) and tested under 0.6:1 biaxial loading. An additional fabrication step was included to address the concern that there could be a zone of embrittled material remaining in the region of the LDCS/flaw intersection that could influence fracture results. After fatigue precracking, a mechanical milling process was used to relieve each corner of the sharpened flaw. The

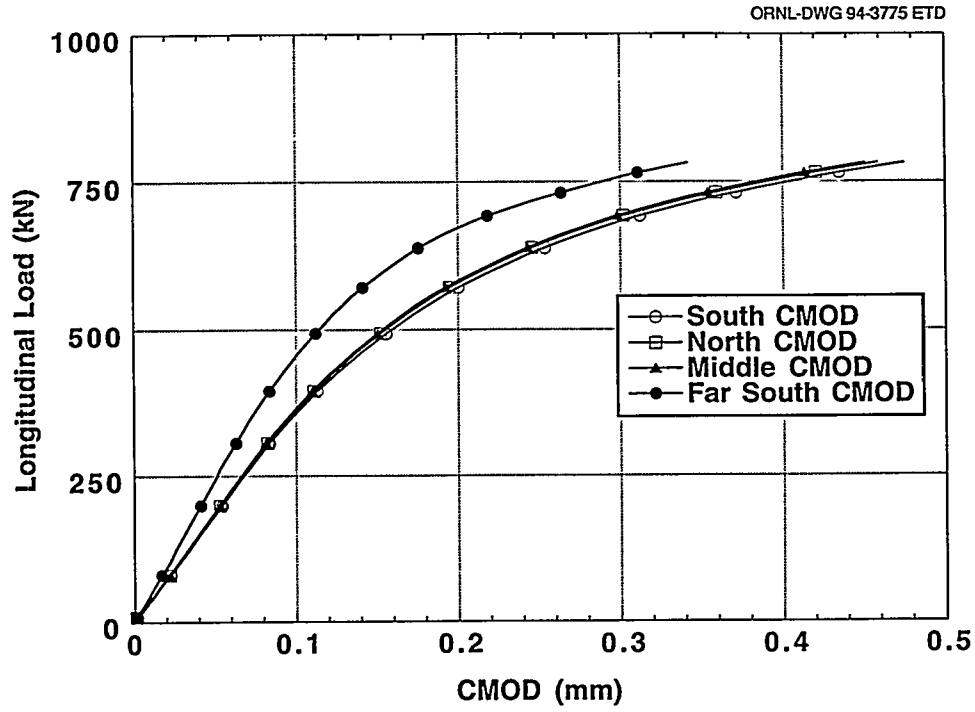

Figure 2.15 CMOD for failure test of shallow-flaw cruciform specimen BB-1: load ratio = 0.6:1

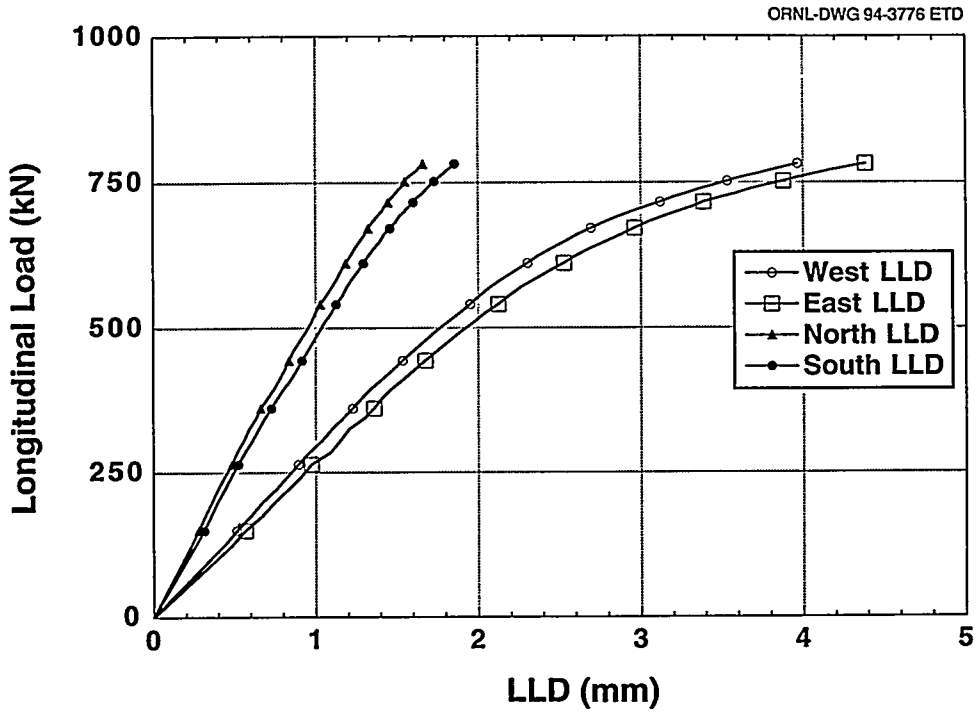

Figure 2.16 LLD for failure test of shallow-flaw cruciform specimen BB-1

Load-Ratio

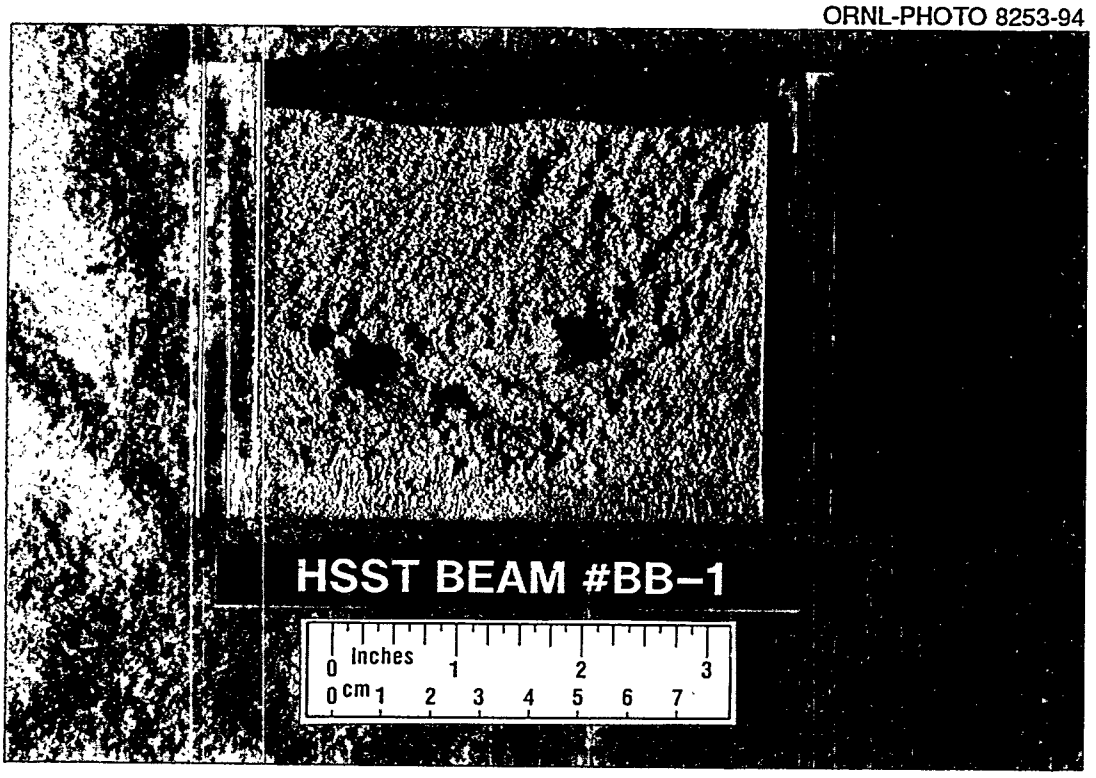

Figure 2.17 Fracture surface for shallow-flaw cruciform specimen BB-1 with fracture initiation site indicated

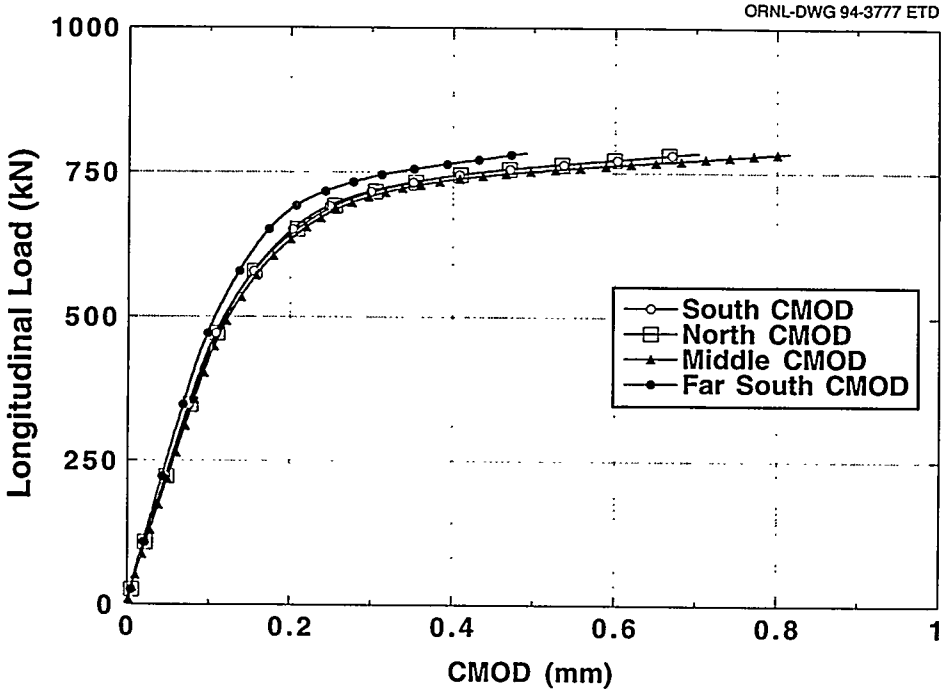

Figure 2.18 CMOD for failure test of shallow-flaw cruciform specimen BB-2: load ratio = 0:1

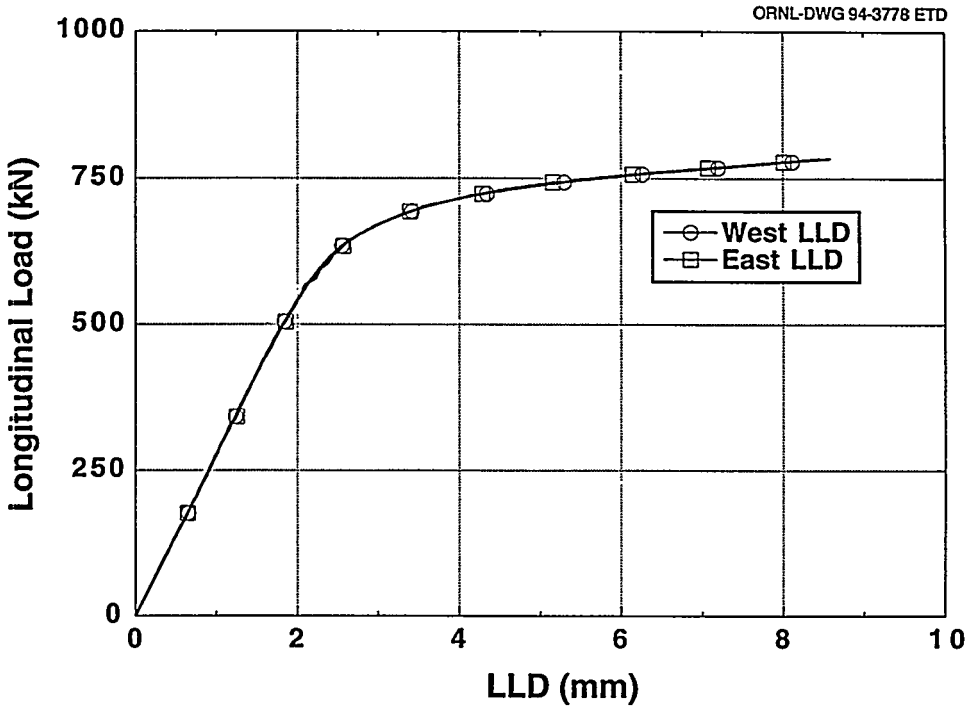

Figure 2.19 LLD for failure test of shallow-flaw cruciform specimen BB-2

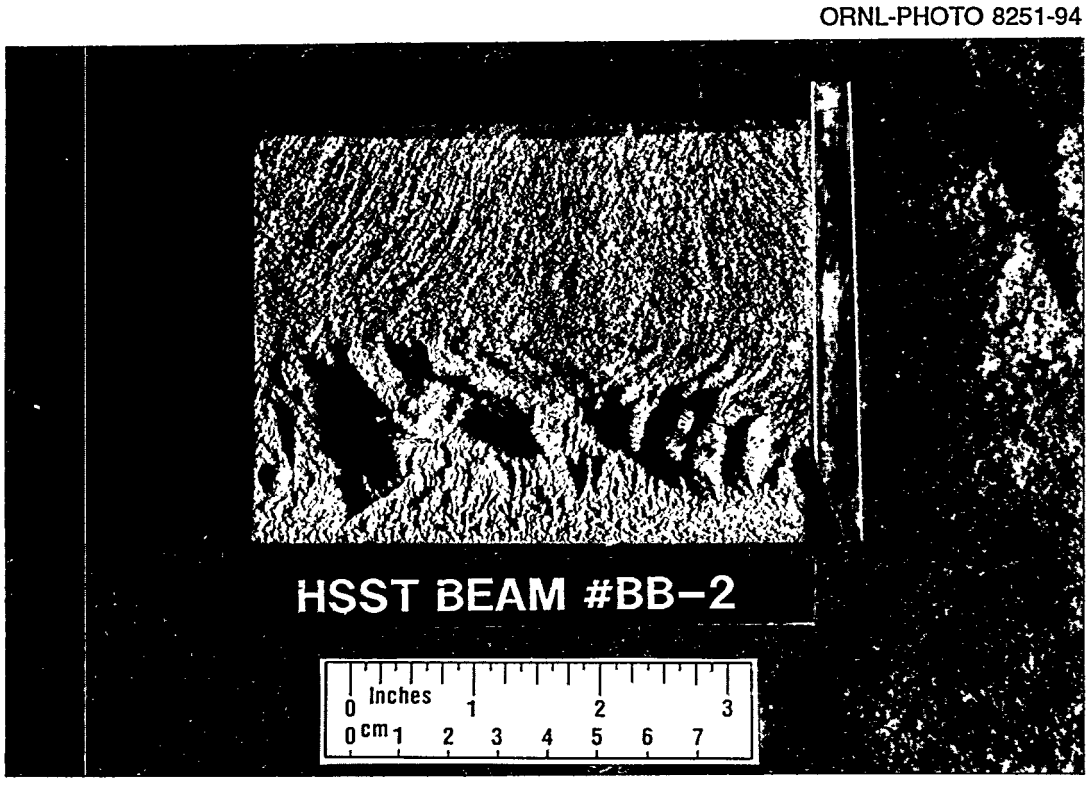

Figure 2.20 Fracture surface for shallow-flaw cruciform specimen BB-2 with fracture initiation site indicated

ORNL-PHOTO 8255-94

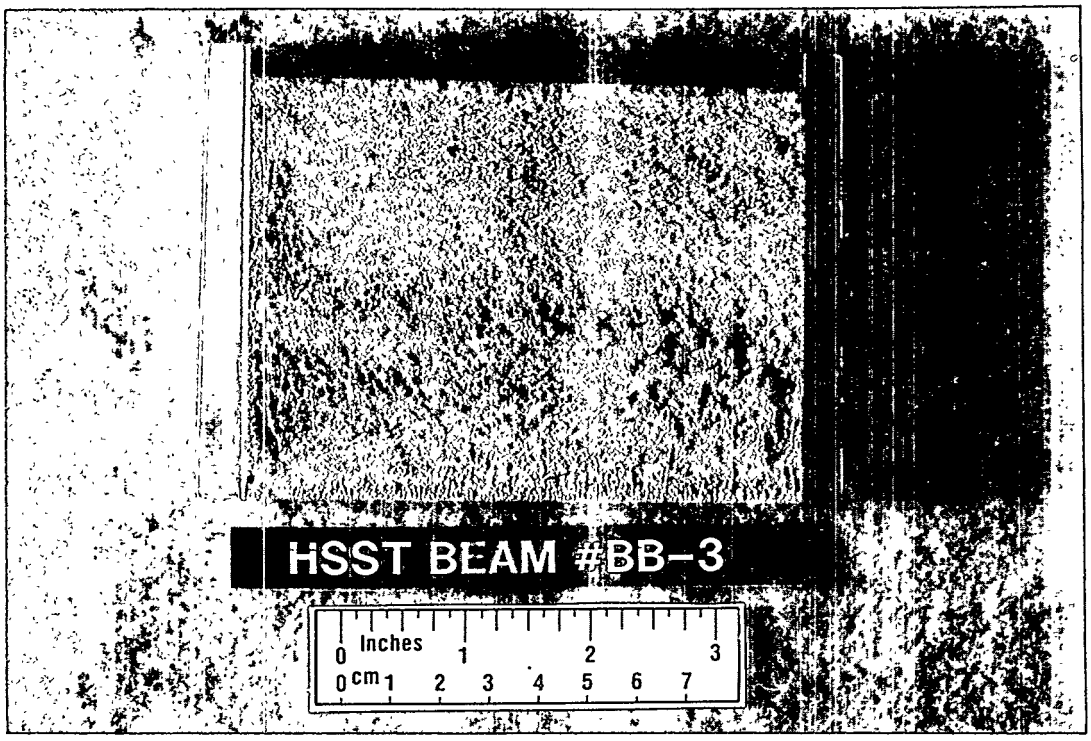

Figure 2.21 Fracture surface for shallow-flaw cruciform specimen BB-3 with fracture initiation site indicated

CMOD results (Fig. 2.22) and the LLD results (Fig. 2.23) exhibited well-behaved deformation response. In particular, the three center clip gages indicated a very uniform distribution of CMOD across that portion of the flaw mouth; this was consistent with pretest predictions of a more uniform CMOD, and thus K_J, distribution. Posttest examination of the fracture surface (Fig. 2.24) revealed the fracture initiation site to be ~18 mm from the north edge of the specimen, well within the flaw region to yield valid toughness results. Also, note in Fig. 2.24 the relief of the corner intersection of the center LDCS and the fatigue precracked flaw. The next specimen, specimen BB-5, used the same LDCS configuration and was tested under the same biaxial loading as BB-4. The CMOD and LLD results are shown in Figs. 2.25 and 2.26, and the fracture

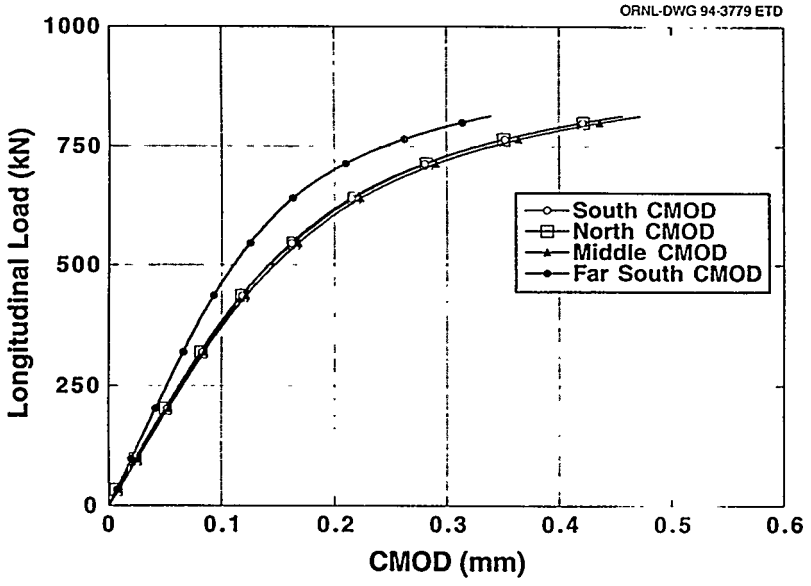

Figure 2.22 CMOD for failure test of shallow-flaw cruciform specimen BB-4: load ratio = 0.6:1

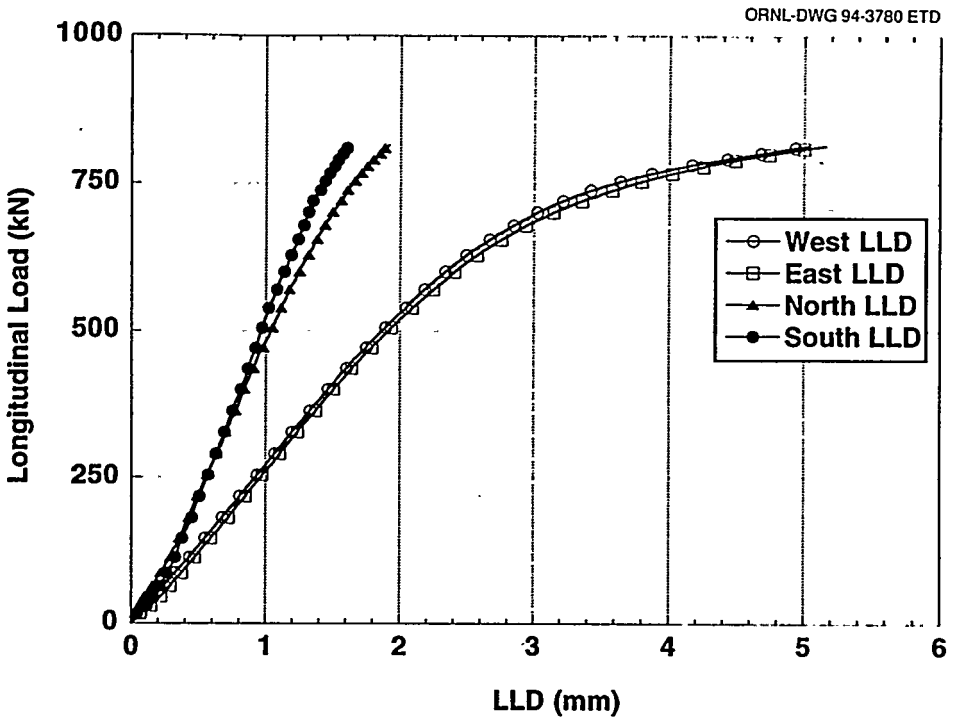

Figure 2.23 LLD for failure test of shallow-flaw cruciform specimen BB-4: load ratio = 0.6:1

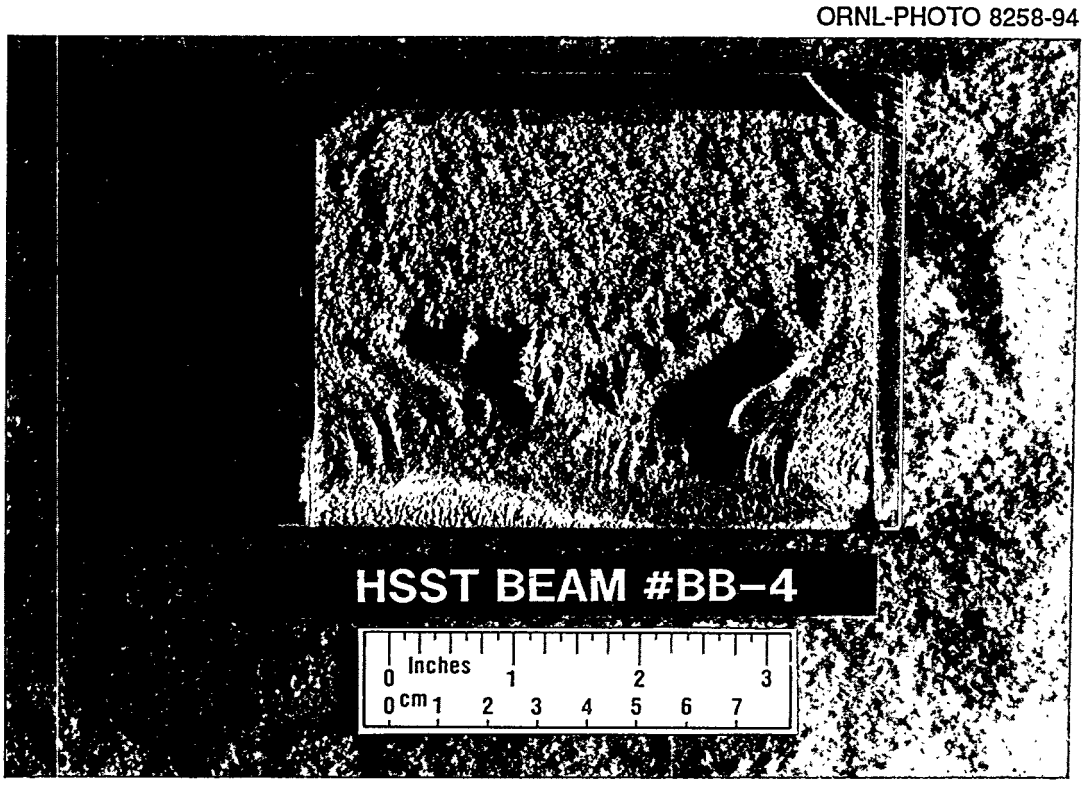

Figure 2.24 Fracture surface for shallow-flaw cruciform specimen BB-4 with fracture initiation site indicated

Load-Ratio

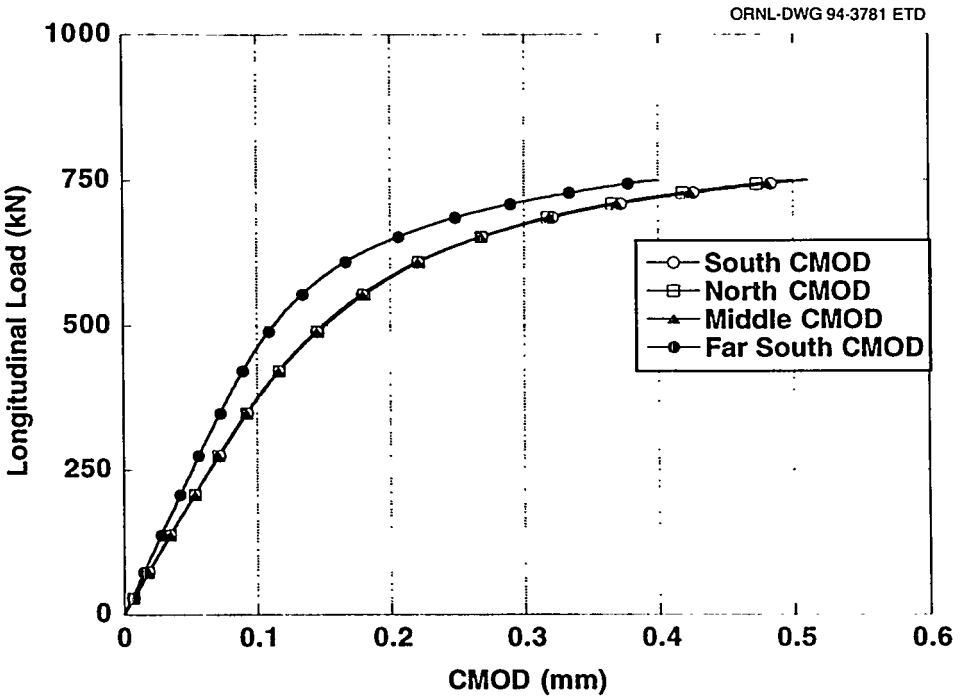

Figure 2.25 CMOD for failure test of shallow-flaw cruciform specimen BB-5: load ratio = 0.6:1

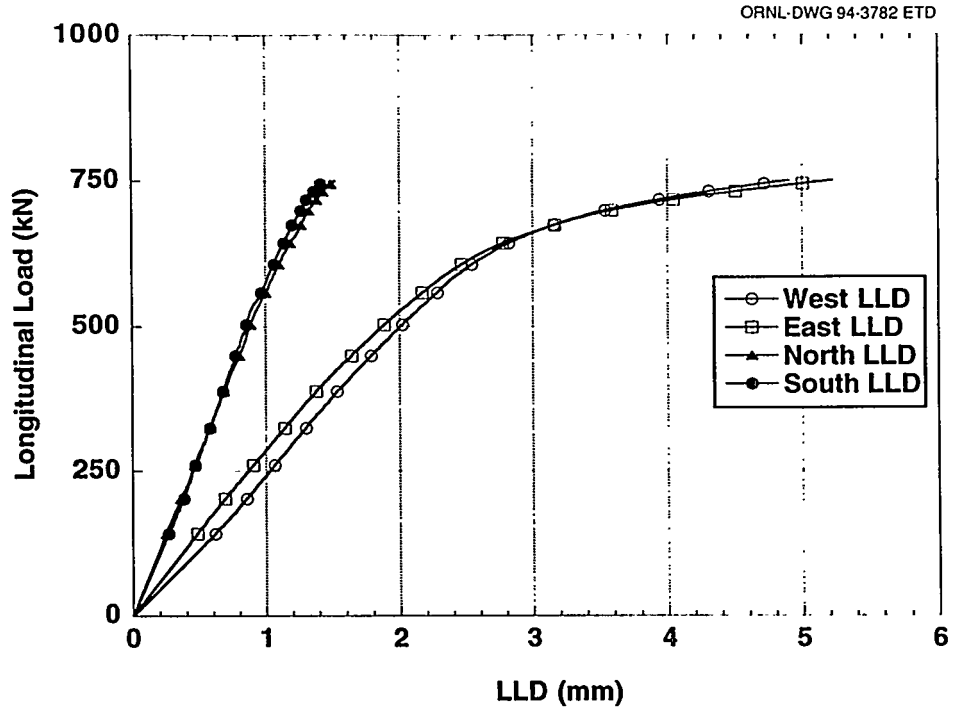

Figure 2.26 LLD for failure test of shallow-flaw cruciform specimen BB-5: load ratio = 0.6:1

surface is shown in Fig. 2.27. In this case, fracture occurred very near the center of the specimen, which is the theoretical point of greatest K_J.

The test conditions and fracture observations for the specimens in Phase I are summarized in Table 2.1. Specimens BB-4 and -5 confirmed the use of configuration (*d*) as being satisfactory for the generation of valid uniaxial and biaxial fracture toughness data. All subsequent specimens used this basic configuration.

In presenting the deformation data, the longitudinal load has been used as the independent variable. Longitudinal load generates the primary flaw-tip driving force and

ORNL-PHOTO 8259-94

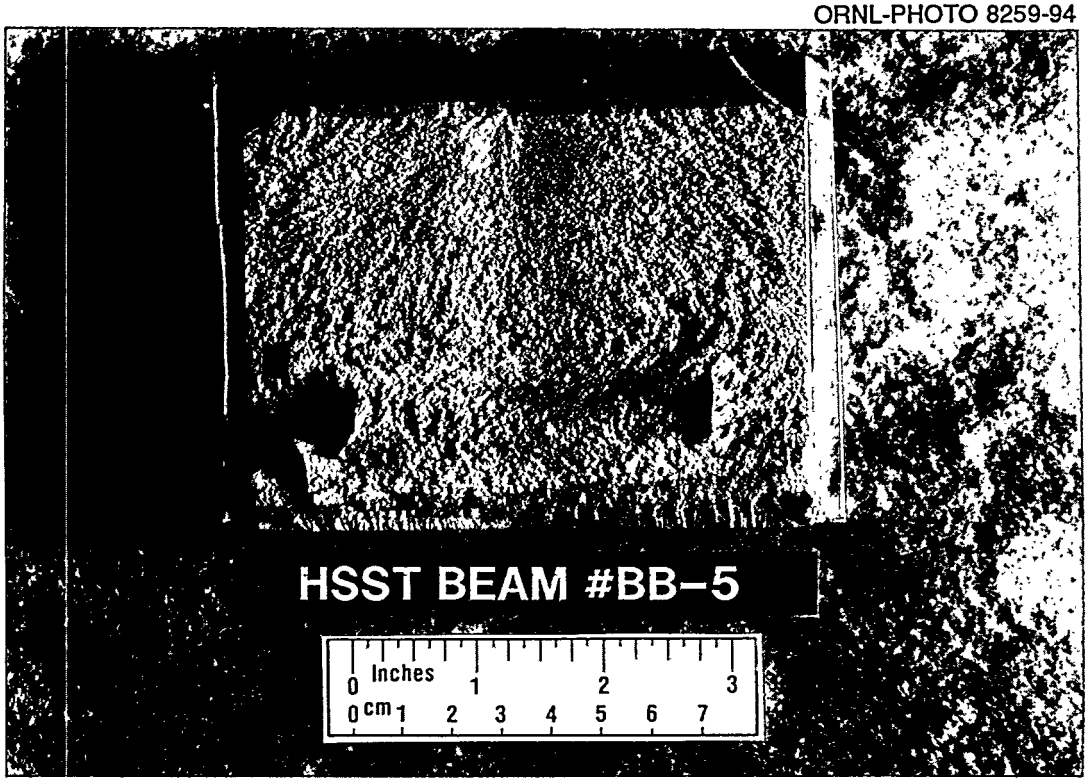

Figure 2.27 Fracture surface for shallow-flaw cruciform specimen BB-5 with fracture initiation site indicated

Table 2.1 Summary of load ratio specimens and fracture observations

Specimen No.	Load ratio	Test section configuration	Fracture initiation site	Result
		Phase I		
BB-1	0.6:1	*b*	2.5 mm from south edge	Acceptable
BB-2	0:1	*c*	20 mm from north edge	Acceptable
BB-3	0.6:1	*c*	North corner	Not acceptable[a]
BB-4	0.6:1	*d*	18 mm from north edge	Acceptable
BB-5	0.6:1	*d*	50 mm from south edge	Acceptable
		Phase II		
BB-7	1:1	*d*	50 mm from edge	Acceptable
BB-9	1:1	*d*	48 mm from edge	Acceptable
BB-10	1:1	*d*	47 mm from edge	Acceptable
BB-11	0:1	*d*	56 mm from edge	Acceptable

[a]Due to initiation in corner.

Load-Ratio

provides a consistent basis for comparison of specimens with different biaxial loading. Because the force applied to the transverse beam arms is directly proportional to the hydraulic cylinder pressure, the pressure ratio was used to determine the biaxial load ratio actually applied to the specimen.

The results for Phase II tests are shown in Figs. 2.28–2.39 using the same sequential ordering, that is, CMOD, LLD, and fracture surface, as was used previously. As is noted in Table 2.1, these specimens all failed near the center of the flaw and thus yielded valid fracture-toughness results. A summary of the failure results for all specimens is shown in Table 2.2. When comparing CMOD and LLD values from Table 2.2, the specimens loaded under 0.6:1 biaxiality form a distinct group. With one exception, the specimens subjected to 0:1 and 1:1 biaxial loading behaved similarly. The exception was specimen BB-10, which failed at a load level significantly less than any other specimen. The CMOD and LLD for this specimen were correspondingly less. The interpretation of these results is covered in Chap. 4 of this report. The procedures for determining toughness are discussed in the following paragraphs.

2.4 Data Reduction Procedures and Toughness Estimates

2.4.1 Data Reduction

Because the cruciform specimen used in this investigation differs from standard ASTM fracture-toughness specimens, combined analytical methods and experimental results are required to determine fracture toughness. For the cruciform tests, fracture toughness is estimated in terms of the critical J-integral and is then converted into an elastic-plastic stress-intensity factor, K_{Jc}. Two techniques, both based on the "work" at the flaw tip as measured by the area under the load vs deflection curves, are employed to estimate toughness. The first of these techniques utilizes the area under the experimental load-CMOD curve to calculate toughness, while the second utilizes the load-LLD curve. In addition to experimental load vs deflection data, both techniques require an η-factor that relates work at the flaw tip to initiation toughness and is determined from FEAs of the specimen. The η-factor technique does not require different FEAs for small variations in specimen geometry, flaw depth, and load distribution because the FEA results are somewhat insensitive to such *small* variations. By using the work at the flaw tip, both critical load and critical displacement factor into the determination of toughness.

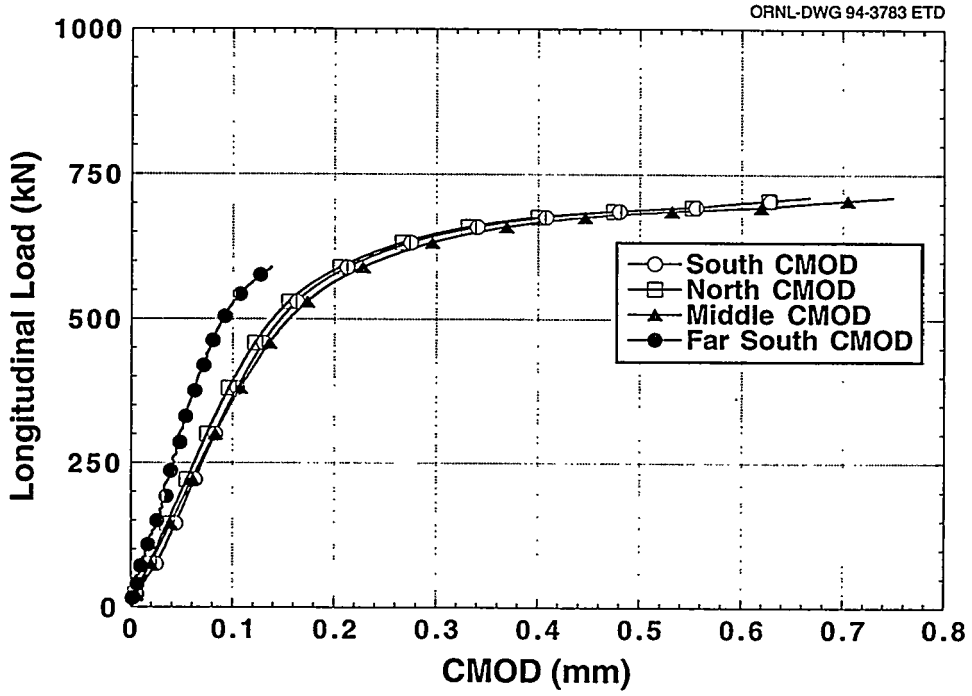

Figure 2.28 CMOD for failure test of shallow-flaw cruciform specimen BB-7: load ratio = 1:1

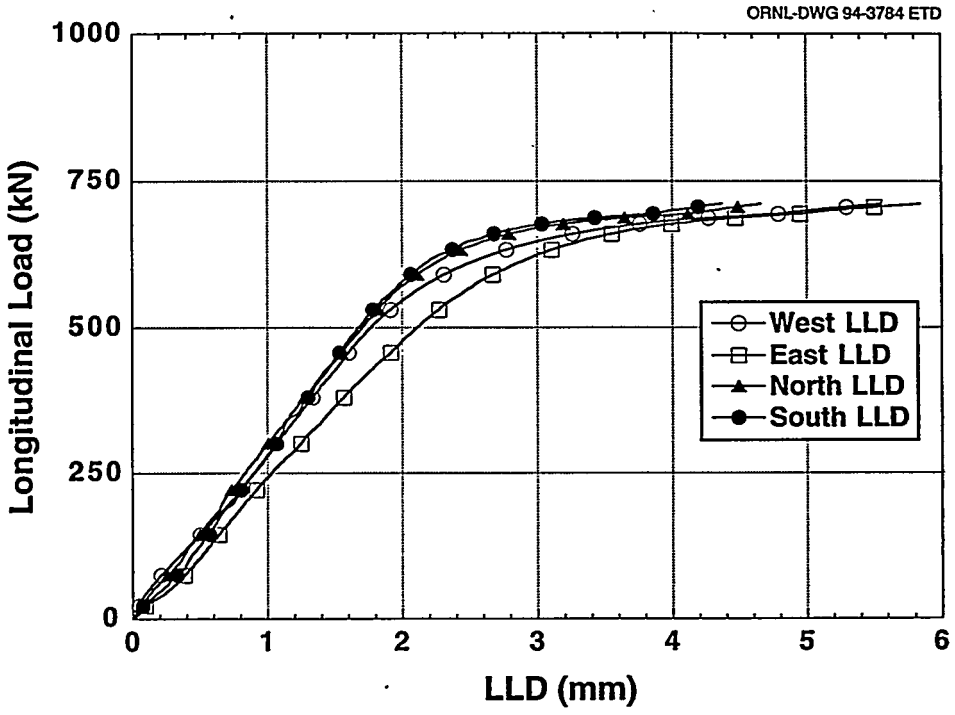

Figure 2.29 LLD for failure test of shallow-flaw cruciform specimen BB-7: load ratio = 1:1

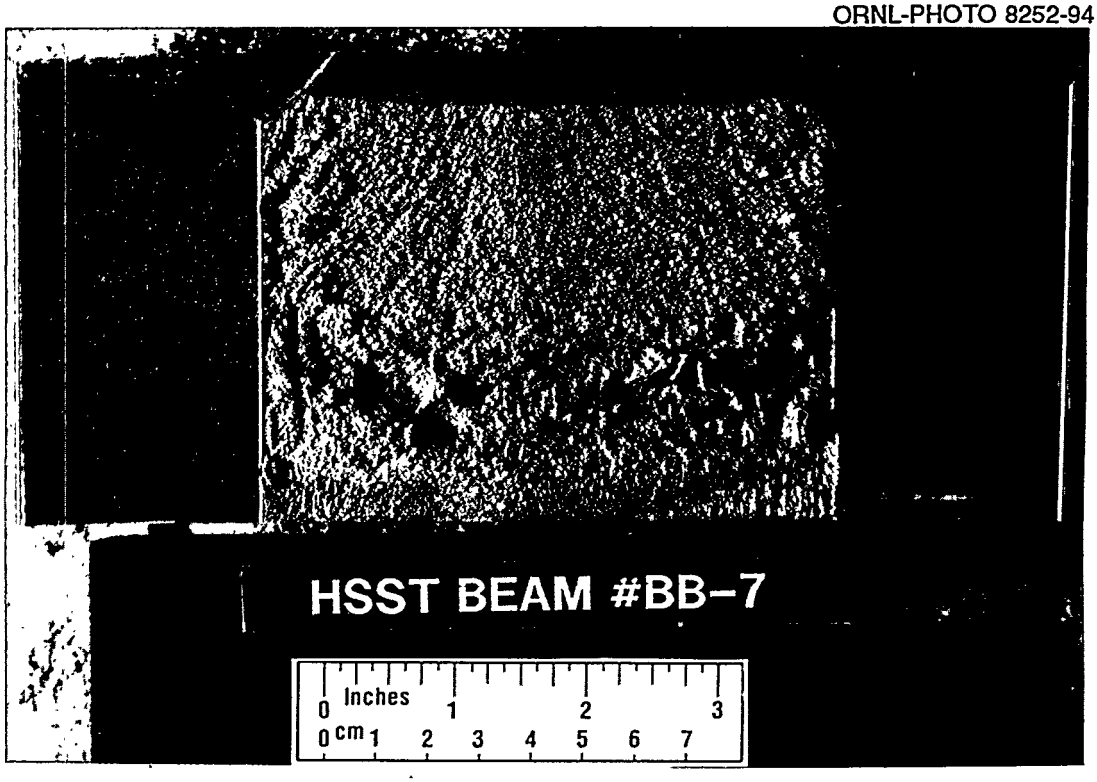

Figure 2.30 Fracture surface for shallow-flaw cruciform specimen BB-7 with fracture initiation site indicated

Load-Ratio

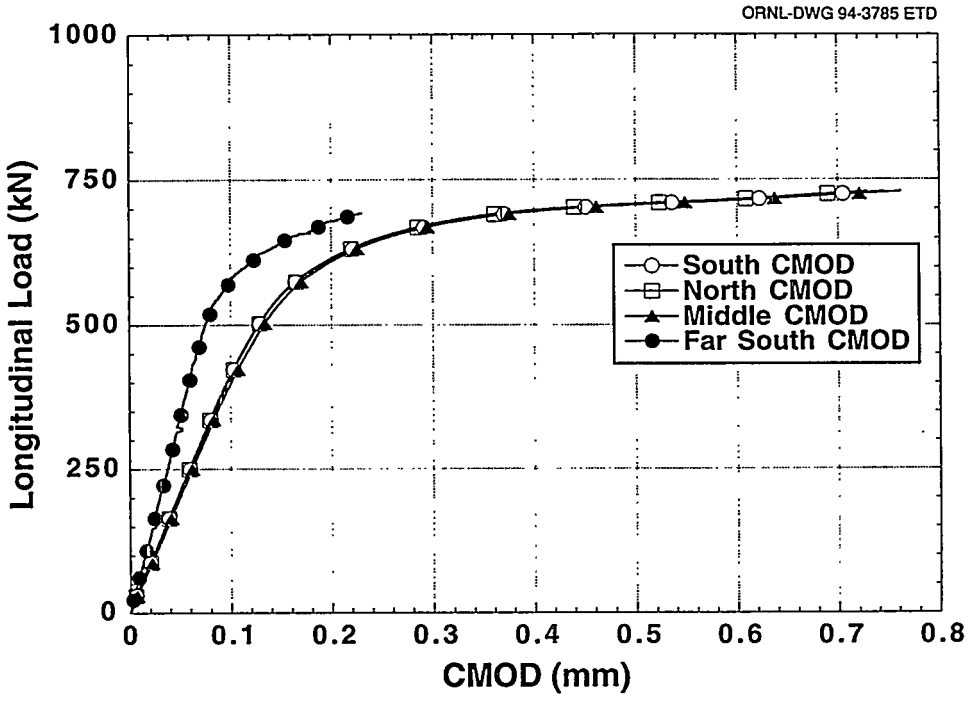

Figure 2.31 CMOD for failure test of shallow-flaw cruciform specimen BB-9: load ratio = 1:1

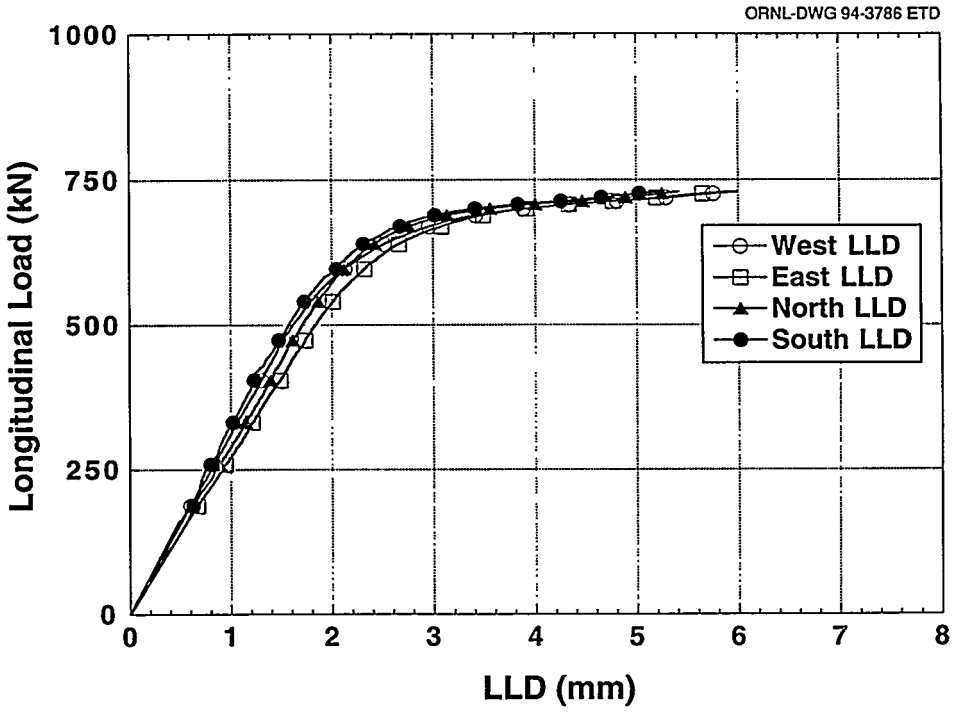

Figure 2.32 LLD for failure test of shallow-flaw cruciform specimen BB-9: load ratio = 1:1

To illustrate the data reduction procedures, the load-CMOD method of calculating toughness will be presented in detail. Note that essentially the same procedures are applied for the load-LLD method. The technique for estimating J is similar in many respects to that presented in ASTM E813 (Ref. 8). This technique was first proposed by Kirk and Dodds[9] and uses the area under the load vs CMOD curve rather than the plastic component of CMOD

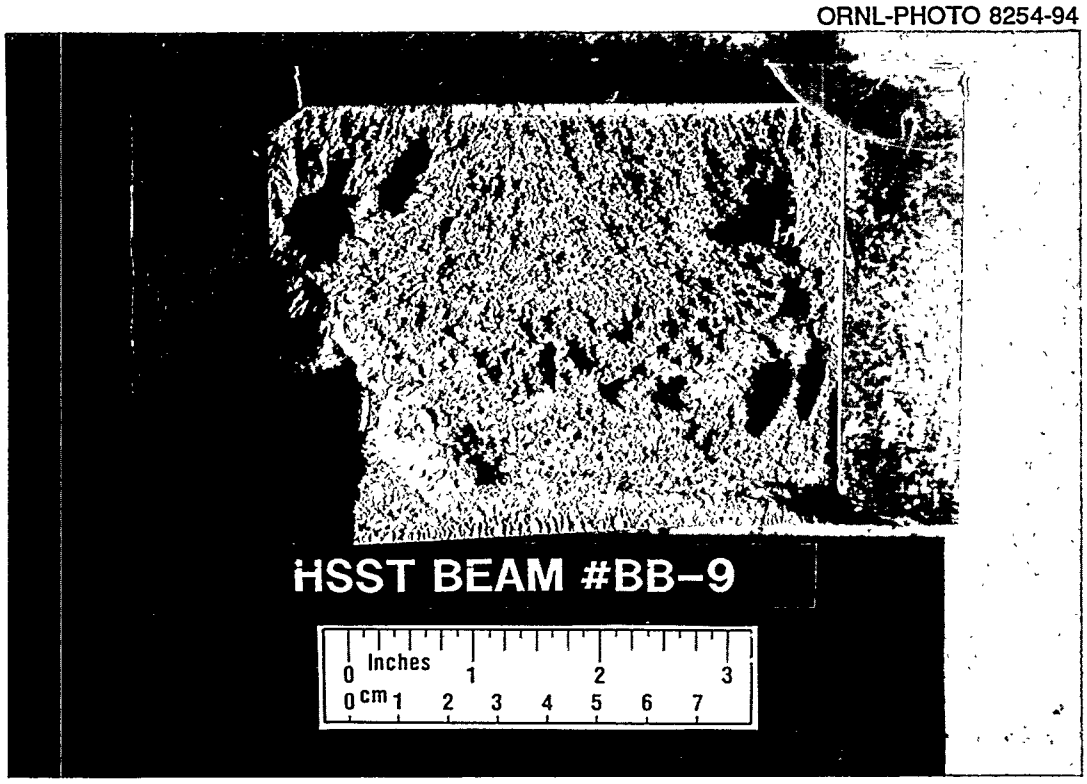

Figure 2.33 Fracture surface for shallow-flaw cruciform specimen BB-9 with fracture initiation site indicated

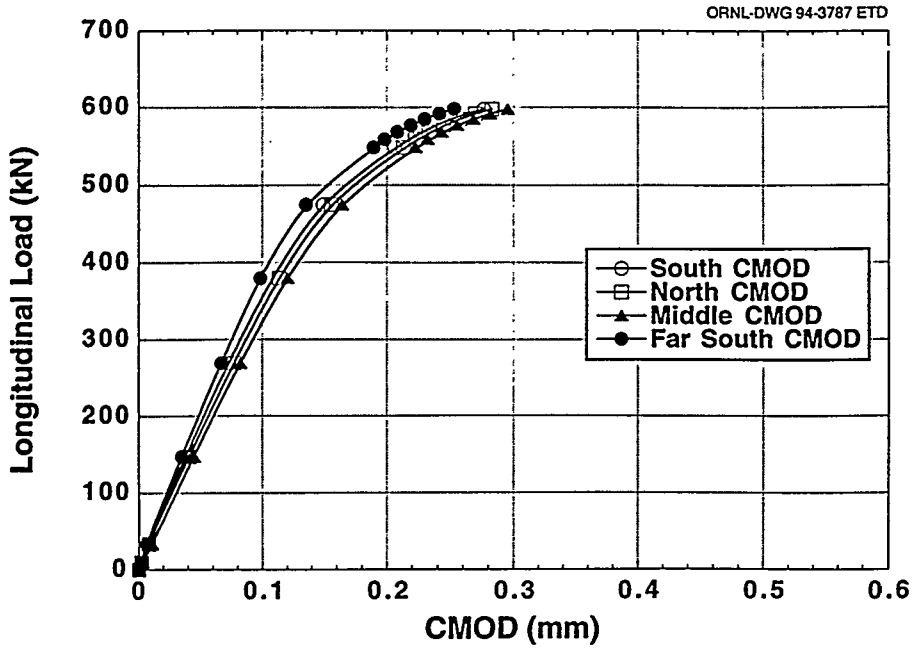

Figure 2.34 CMOD for failure test of shallow-flaw cruciform specimen BB-10: load ratio = 1:1

to calculate J. The J-integral is divided into elastic and plastic components as shown in the following equation.

$$J = J_{el} + J_{pl} = J_{el} + \frac{\eta_{pl}^{c} A_{pl}}{Bb}, \qquad (2.1)$$

where

J_{el} = elastic component of J,
J_{pl} = plastic component of J,
A_{pl} = plastic component of area under load versus CMOD curve,
B = specimen thickness,

Load-Ratio

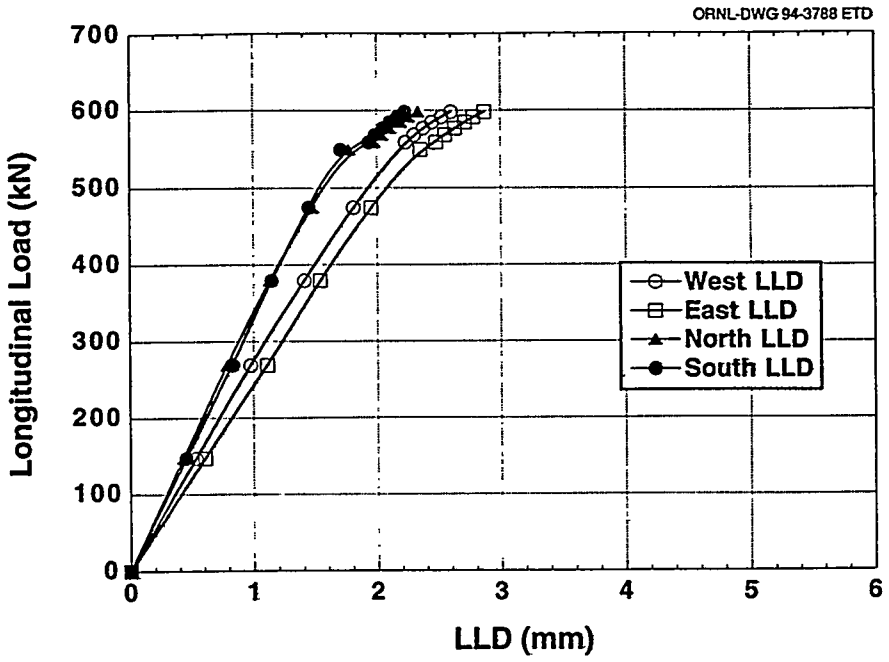

Figure 2.35 LLD for failure test of shallow-flaw cruciform specimen BB-10: load ratio = 1:1

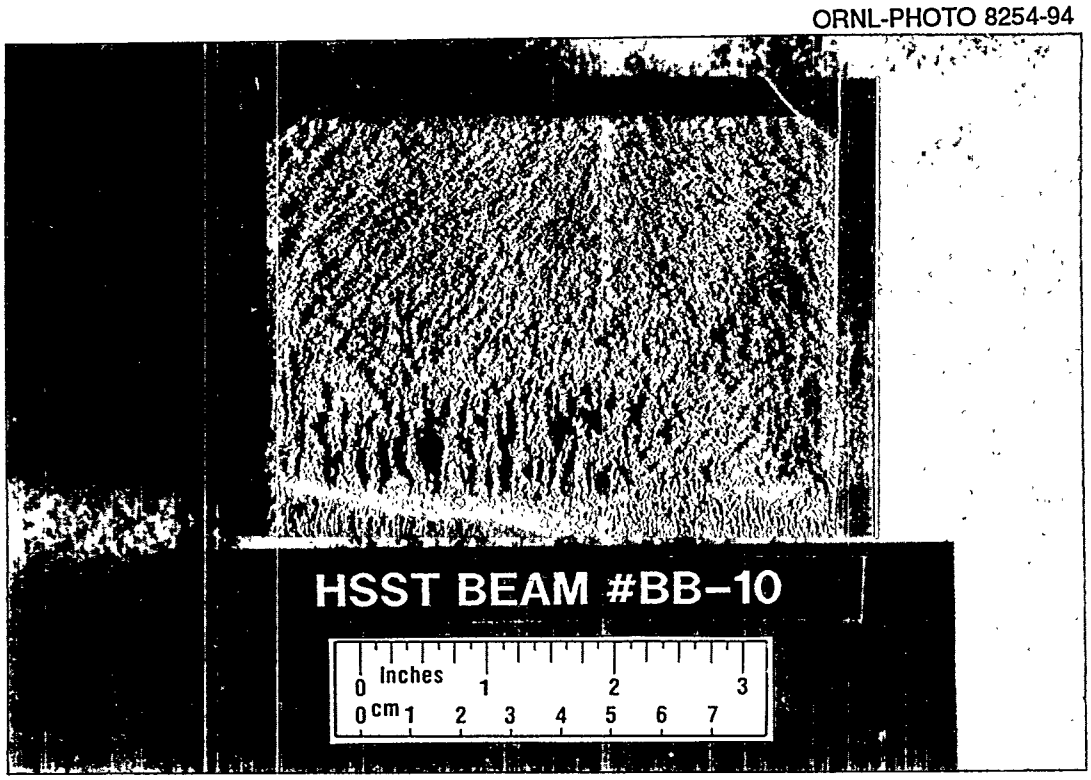

Figure 2.36 Fracture surface for shallow-flaw cruciform specimen BB-10 with fracture initiation site indicated

b = the remaining ligament (W-a),

η_{pl}^{c} = η-factor determined from the plastic area under the load-CMOD curve for a given applied J_{pl}. This is a dimensionless constant relating the area term A_{pl} to J_{pl}.

The η-factor for a particular test was determined using an elastic-plastic FEA in conjunction with the failure load for the test being evaluated. The analysis was performed using the test-specific load ratio with flaw depth, geometry, and material properties being the same for all analyses. The flaw depth was taken as a constant 10 mm. After fatigue

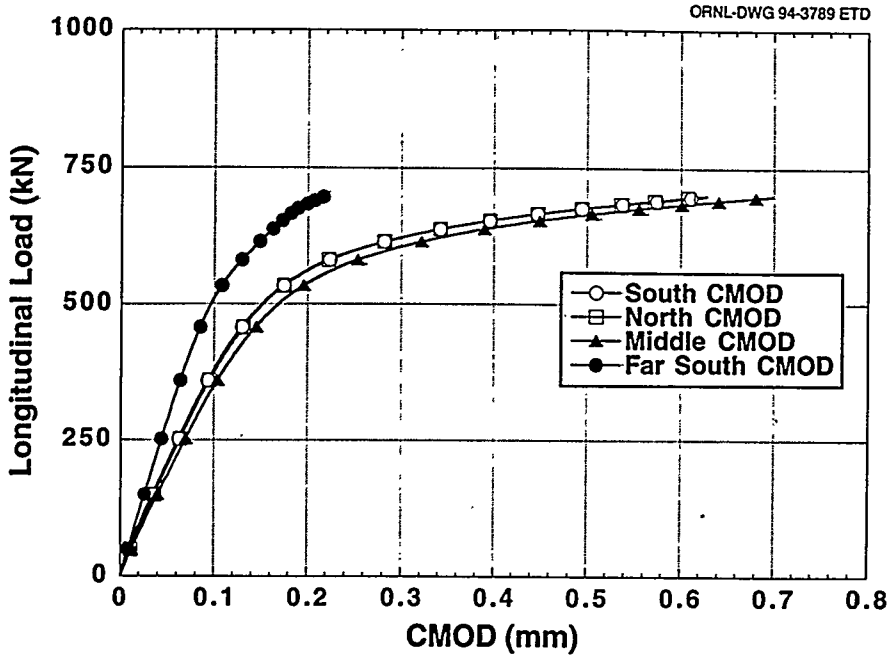

Figure 2.37 CMOD for failure test of shallow-flaw cruciform specimen BB-11: load ratio = 0:1

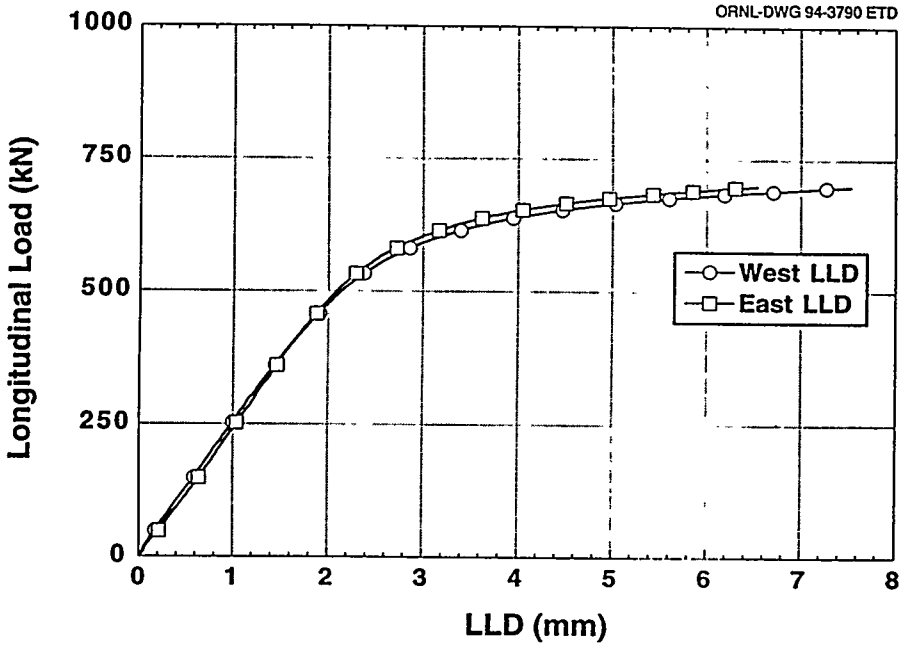

Figure 2.38 LLD for failure test of shallow-flaw cruciform specimen BB-11: load ratio = 0:1

precracking, there was some variability in flaw depth from specimen to specimen, but small variations in depth have negligible impact on the calculation of the η-factor. The actual flaw depth was incorporated into the final toughness calculation as is discussed later. The results of the FEA provided tabular values of centerline CMOD, LLD, J, and K vs longitudinal load for use in the η-factor and toughness evaluations.

While the data reduction procedures were performed numerically, a graphical illustration will be presented here for simplicity. Determination of the η-factor for a particular test was based primarily on the FEA results for the specific load ratio. The only experimental result used at this point was the failure load measured in the test. Integration of the FEA results was used to determine the total area under the load-CMOD curve up to the failure load. The total area, A_{total}, is that given by the area ABCA in

Load-Ratio

ORNL-PHOTO 8257-94

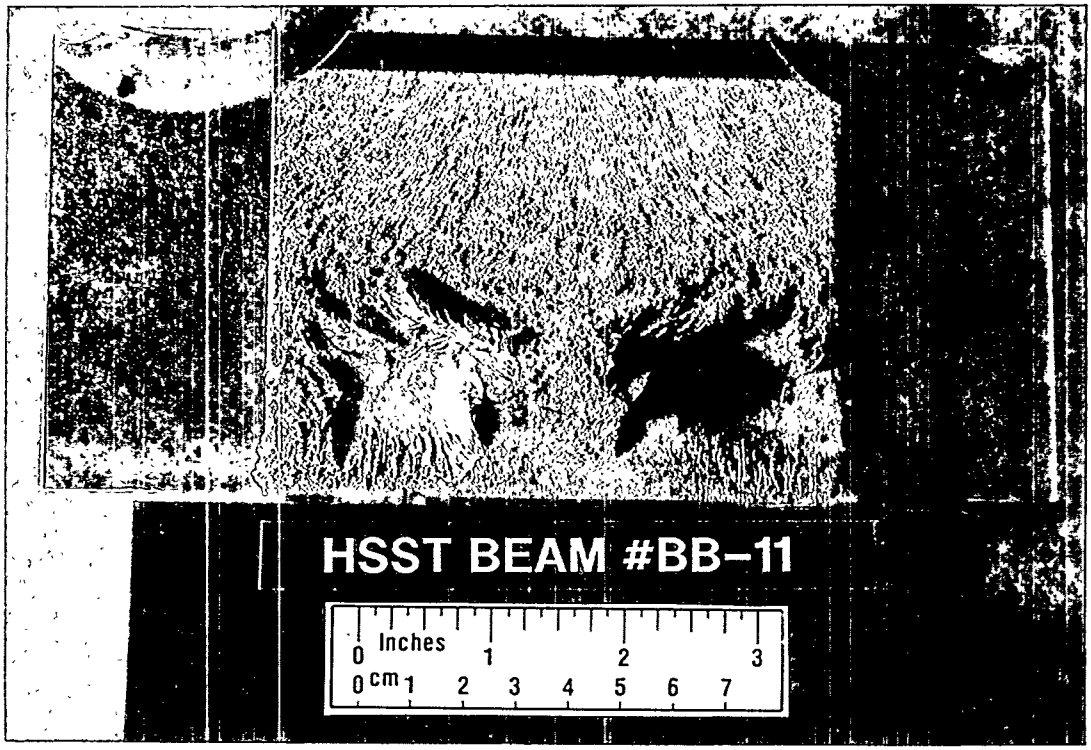

Figure 2.39 Fracture surface for shallow-flaw cruciform specimen BB-11 with fracture initiation site indicated

Fig. 2.40. The elastic area, A_{el}, is determined by the triangle DBC. The plastic area is then

$$A_{pl} = A_{total} - A_{el} \ .$$

The value of elastic stress intensity, K_{el}, from the FEA was used to calculate the elastic component of the J-integral at the failure load,

$$J_{el} = \frac{K_{el}^2(1-\nu^2)}{E} \ , \qquad (2.2)$$

where ν = Poisson's ratio and E = elastic modulus.

The η-factor was then determined from Eq. (2.1) using the value of J from the FEA corresponding to the failure load for the particular test. One point should be obvious from this procedure. Reliable predictions of the measured deformation behavior of the specimen are required to ensure that the η-factor is representative of the measured plastic response. Care was, therefore, taken in the modelling to match the experimentally determined deformation response of the specimen as closely as possible (see Chap. 3). Also, detailed materials characterizations were performed to ensure that the stress-strain curve used in the analyses was representative of the material behavior and that there was no through-thickness variation in properties that could affect the elastic-plastic response (see Sect. 2.4.2).

The procedure for determination of toughness followed basically the reverse of that for determination of η-factor. It was necessary to evaluate the elastic and plastic components of J using the experimental and FEA results. Using Eq. (2.2), the load vs K_{el} relationship from the FEA was used to determine the elastic component of J at failure. Integration of the area under the experimentally measured load vs CMOD curve provided A_{total}, which could be separated into A_{el} and A_{pl} as was done for the η-factor determination. The J value for the test was then calculated from Eq. (2.1), and the toughness was determined by

$$K_{JC} = \sqrt{\frac{J_C E}{(1-\nu^2)}} \ . \qquad (2.3)$$

The η-factors and toughness values for all tests determined using this technique are summarized in Table 2.2.

As noted, toughness values were determined in terms of the longitudinal load applied to the specimen. Use of longitudinal load provides a convenient normalizing parameter for comparing the results from all tests. However, application of an out-of-plane stress will produce additional

Table 2.2 Summary of results for load ratio fracture-toughness specimens

	Specimen							
	BB-1	**BB-2**	**BB-4**	**BB-5**	**BB-7**	**BB-9**	**BB-10**	**BB-11**
Load ratio	0.6:1	0:1	0.6:1	0.6:1	1:1	1:1	1:1	0:1
Geometry								
B, mm	102	111	111	111	113	113	113	112
W, mm	91	91	91	91	92	92	92	92
a, mm	11.1	10.6	10.1	10.0	9.4	9.9	10.4	9.6
Temperature,[a] °C	–45	–41	–46	–44	–44	–44	–43	–44
T – NDT, °C	–10	–6	–11	–9	–9	–9	–8	–9
Failure conditions								
P, kN	781	784	814	750	711	729	598	700
LLD, mm	4.18	8.51	5.10	5.06	5.70	6.10	2.77	7.00
CMOD, mm	0.45	0.82	0.47	0.51	0.75	0.76	0.29	0.70
U_{pl}, kN-mm	964	3,556	1,397	1,561	1,896	2,055	193	2,705
A_{pl}, kN-mm	161	470	182	210	369	397	60	319
η-factors								
η^{ℓ}_{pl}	0.195	0.237	0.218	0.173	0.610	0.574	0.432	0.275
η^{c}_{pl}	3.530	3.509	4.074	3.660	4.279	4.280	2.485	3.387
Fracture toughness								
Elastic component								
J_{el}, kN/m	72	83	82	69	62	65	44	66
K_I, MPa$\sqrt{m}$	119	128	127	117	111	114	93	114
P vs CMOD								
J_{pl}, kN/m	70	184	82	85	170	184	16	118
Total J, kN/m	141	266	164	154	233	249	60	183
K_{Jc}, MPa$\sqrt{m}$	169	232	182	177	217	224	110	193
P vs LLD								
J_{pl}, kN/m	23	94	34	30	125	127	9	81
Total J, kN/m	95	177	115	99	187	193	53	147
K_{Jc}, MPa$\sqrt{m}$	138	189	153	141	194	198	104	172

[a]For this material: NDT = –35°C.

longitudinal stresses at the flaw tip that will effect the relationships between A_{pl}, J_{pl}, and the η-factor. This is illustrated in Fig. 2.41, which shows the calculated plastic area under the FEA load vs CMOD curves for the three biaxial cases considered in this study. The plastic area does not behave monotonically with increasing biaxiality. When compared to uniaxial loading (0:1), 0.6:1 biaxial loading causes an increase in specimen stiffness, that is, reduced plasticity; while 1:1 biaxial loading causes a decrease in stiffness. The FEA calculated relationship between A_{pl} and J_{pl} for the three biaxial load ratios, however, exhibits monotonic behavior with biaxiality as is shown in Fig. 2.42. The limits of A_{pl} and J_{pl} shown exceed the values calculated for any of the tests in this series. At values of $A_{pl} < 0.1$, the comparative magnitudes of the results for the three biaxial ratios are not considered to be significant. In this range, the specimen deformation is predominantly elastic, and calculation of A_{pl} is highly sensitive to small variations in FEA results. Beyond A_{pl} of 0.1, trend lines are established that show a direct relationship between A_{pl}, J_{pl}, and the biaxial load ratio, an increase in biaxiality causes an increase in J_{pl} for the same level of A_{pl}. This same trend is exhibited in the relationship between A_{pl} and η-factor as is shown in Fig. 2.43. As with J_{pl}, the η-factor values determined at low A_{pl} values are not considered to be reliable. As A_{pl} increases, the same ordering is established with increasing magnitude of η-factor with increasing biaxiality. The out-of-plane stress component then does cause a change in the opening-mode plastic strains around the crack tip with subsequent changes in J and K for the

Load-Ratio

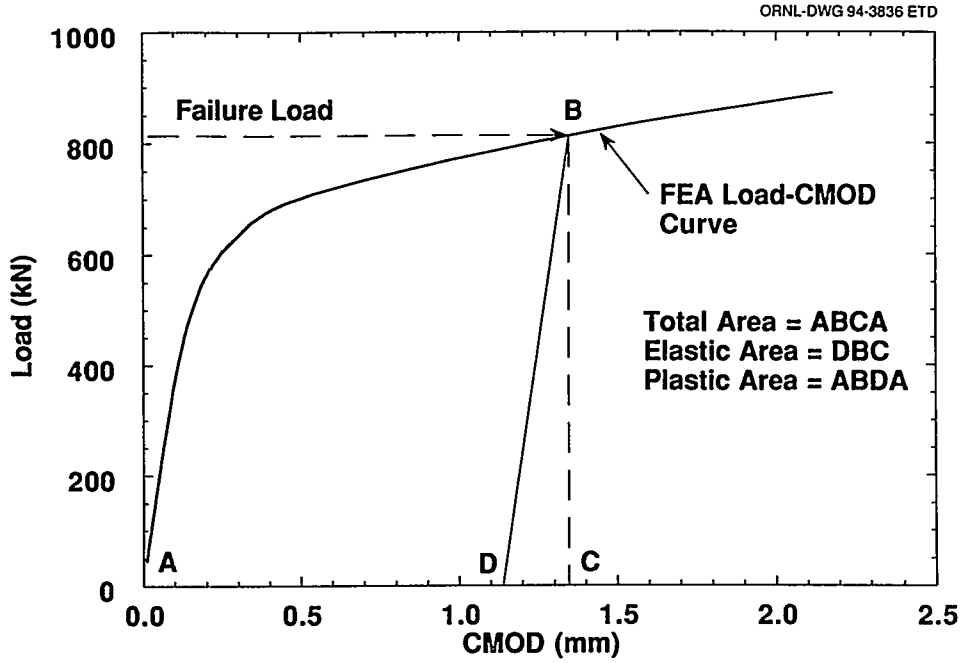

Figure 2.40 Graphical representation of procedure for determination of plastic component of area under longitudinal load-CMOD curve for cruciform specimen

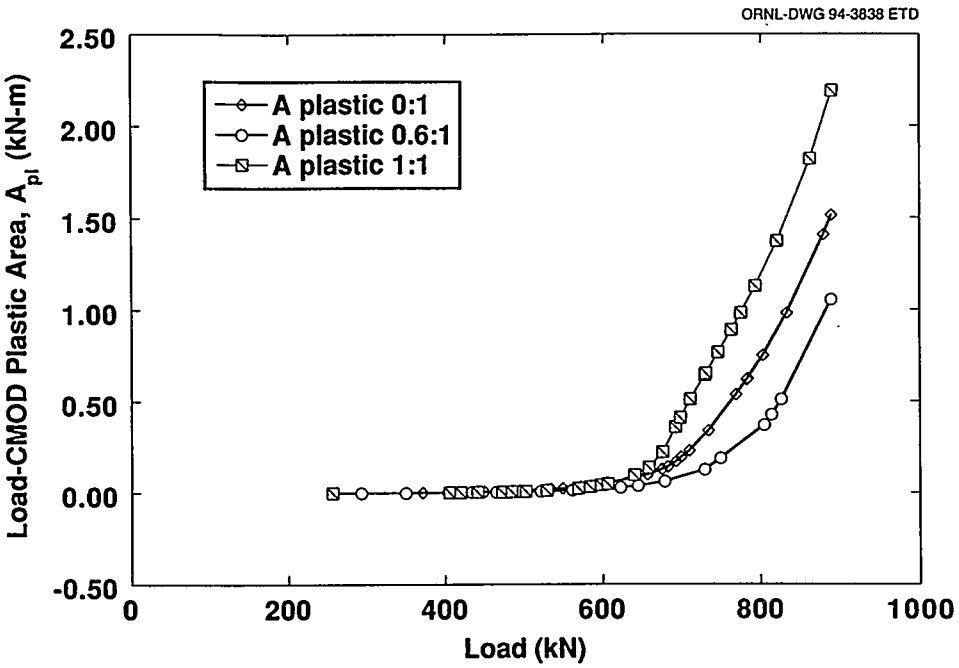

Figure 2.41 Plastic area under FEAs longitudinal load-CMOD curve as function of biaxial load ratio

same levels of longitudinal load. Because the η-factor is determined for each biaxial case, the effect of the out-of-plane stress is reflected in both the elastic and plastic components of J used in the determination of fracture toughness.

The second technique for determining toughness is similar to that just described but uses the load vs LLD record instead. The values of η_{pl}^{ℓ} and K_J determined for each test are shown in Table 2.2 in comparison to those determined using CMOD. Here, η_{pl}^{ℓ} is a dimensionless constant relating the area term, U_{pl}, to J_{pl} and is determined from the plastic area under the load-LLD curve. As was discussed in Ref. 1, at this stage of development of this specimen, refinements associated with attempts to estimate toughness considering the distribution of CMOD, LLD, J, and K along the flaw tip are not warranted.

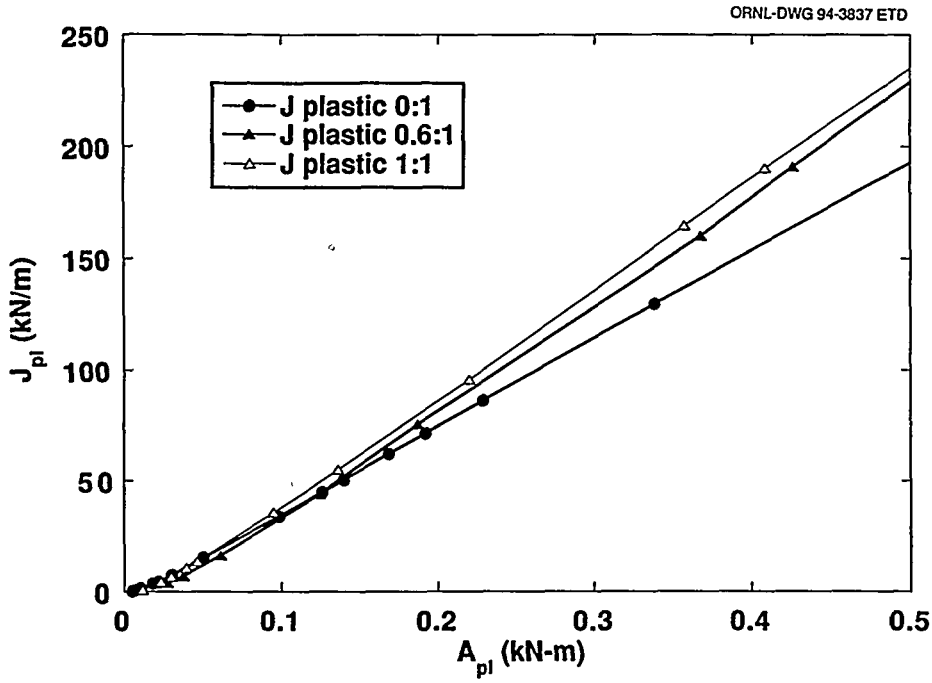

Figure 2.42 Relationship between longitudinal load-CMOD plastic area and plastic component of J as determined from FEAs of cruciform specimens

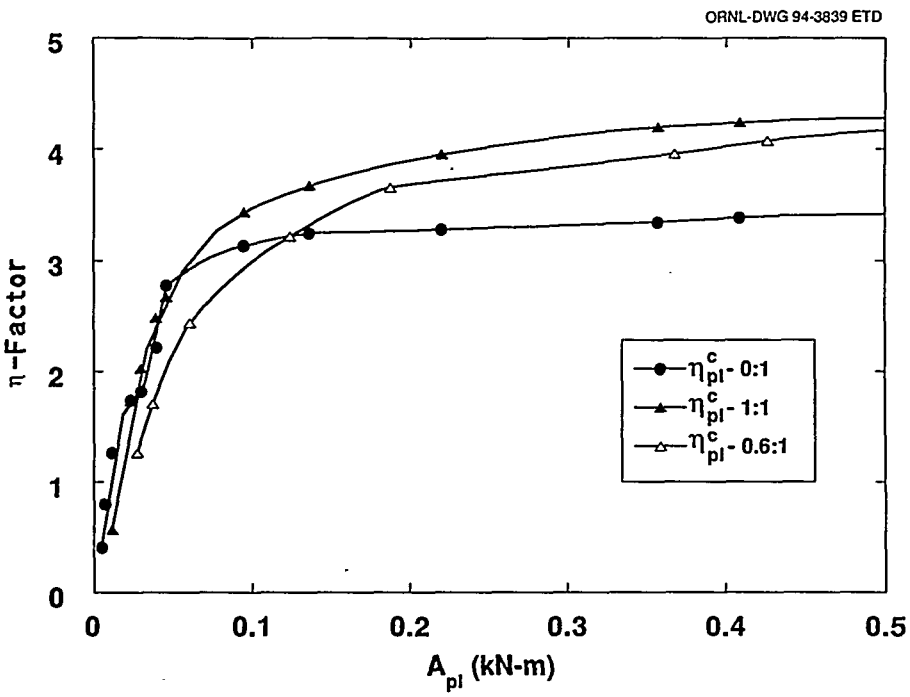

Figure 2.43 Relationship between longitudinal load-CMOD plastic area and η-factor as determined from FEAs of cruciform specimens

Both methods of estimating toughness appear to have advantages and disadvantages. The primary advantage of the LLD-based η-factor method is that the technique has been used extensively and is similar to the method outlined in ASTM E813. The primary disadvantage is that, for structures of this size and configuration, LLD measurements are less sensitive to variations in flaw geometry and deformation that effect material behavior at the flaw tip. This limitation is overcome using the CMOD technique. CMOD measurements are made close to the flaw tip and therefore more appropriately reflect conditions leading to fracture. It is then considered that the CMOD-based η-factor method is considered to be more appropriate for estimating toughness. For these tests, estimates of

toughness using the LLD-based η-factor method were for confirmation only.

2.4.2 Material Properties

As noted previously, interpretation of the data and estimation of fracture toughness from test results requires supporting elastic-plastic FEAs. Preliminary analyses were based on materials properties that had been developed as a "best estimate" for this type of steel. However, it was observed that predictions of CMOD and LLD tended to indicate a "stiffer" structure than what was measured in the experiments. In this case, "stiffer" means primarily that nonlinear behavior was measured in the specimens at load levels where essentially elastic behavior was predicted from the analyses.

Tensile testing was performed using source material that was excess from machining of one of the test sections. Standard ASTM 6.35-mm-diam (0.25-in.) round bar tensile specimens were used. They were machined such that the longitudinal axis of the specimen was parallel to the longitudinal direction of the cruciform specimen. Also, specimens were taken at seven equally spaced levels from near the surface to near the center of the source plate. Tests were performed at room temperature and at –46°C (–50°F) at a loading rate of 0.002 mm/s (0.005 in. /min).

The room temperature results for seven specimens, defining tensile properties from near surface to midplane, are shown in Fig. 2.44. There was consistent hardening from plate midplane to surface, but the difference in properties was entirely negligible. The validity of the assumption of uniform tensile behavior through the thickness of the cruciform was fully verified from these tests. The tensile tests performed at –46°C had the same trend as those shown in Fig. 2.44 with only the yield strength increasing due to the decrease in temperature. For final analyses purposes, the stress-strain curve presented later in Chap. 3 (Fig. 3.4) was recommended.

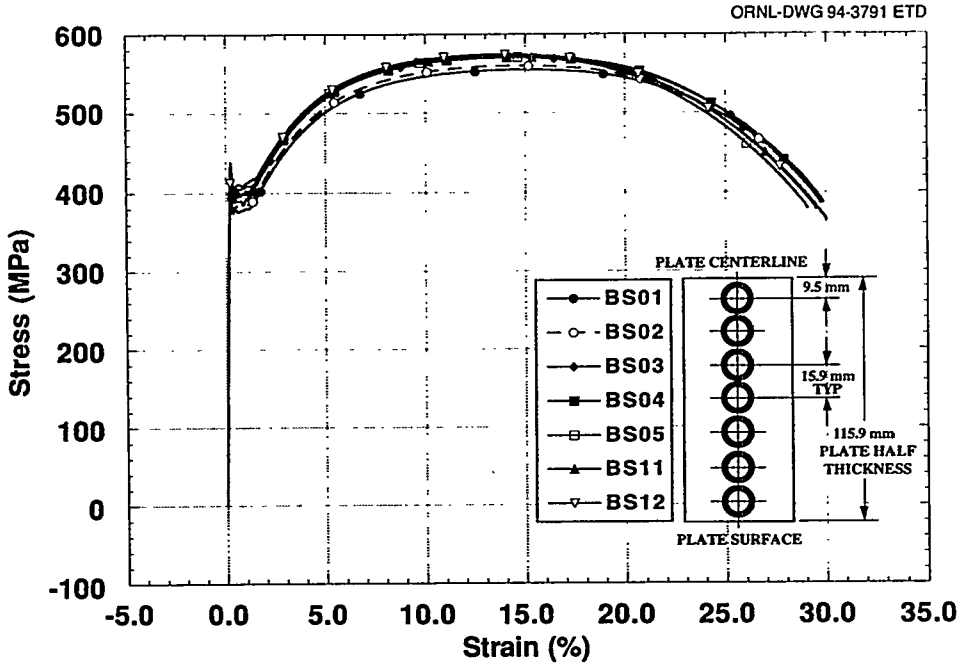

Figure 2.44 Room temperature stress-strain curves for CE plate material in as-received condition illustrating minimal through-thickness variation in tensile properties

References

1. T. J. Theiss et al., Martin Marietta Energy Systems, Inc., Oak Ridge National Laboratory, "Initial Results of the Influence of Biaxial Loading on Fracture Toughness," USNRC Report NUREG/CR-6036 (ORNL/TM-12349), April 1993.*

2. B. R. Bass et al., Martin Marietta Energy Systems, Inc., Oak Ridge National Laboratory, "Biaxial Loading and Shallow-Flaw Effects on Crack-Tip Constraint and Fracture Toughness," USNRC Report NUREG/CR-6132 (ORNL/TM-12498), January 1994.*

3. W. E. Pennell et al., "Biaxial Loading and Shallow-Flaw Effects on Crack-Tip Constraint and Fracture

Toughness," pp. 102–114 in *Changing Priorities of Codes and Standards: Failure, Fatigue, and Creep*, PVP-Vol. 286, American Society of Mechanical Engineers, 1994.†

4. U.S. Nuclear Regulatory Commission Regulatory Guide 1.154, *Format and Content of Plant-Specific Pressurized Thermal Shock Safety Analyses Reports for Pressurized Water Reactors*, January 1987.‡

5. D. J. Naus et al., Martin Marietta Energy Systems, Inc., Oak Ridge National Laboratory, "Crack-Arrest Behavior in SEN Wide Plates of Quenched and Tempered A 533 Grade B Steel Tested Under Nonisothermal Conditions," USNRC Report NUREG/CR-4930 (ORNL/TM-6388), August 1987.*

6. D. J. Naus et al., Martin Marietta Energy Systems, Inc., Oak Ridge National Laboratory, "High-Temperature Crack-Arrest Behavior in 152-mm-Thick SEN Wide Plate of Quenched and Tempered A 533 Grade B Class 1 Steel," USNRC Report NUREG/CR-5330 (ORNL/TM-11083), April 1989.*

7. T. J. Theiss, D. K. M. Shum, and S. T. Rolfe, "J and CTOD Estimation Equations for Shallow Cracks in Single Edge Notch Bend Specimens," *Proceedings of the TWI Shallow Crack Fracture Mechanics Toughness Tests and Applications Conference, Cambridge, United Kingdom, September 23–24, 1992.*

8. ASTM E813-89, "Standard Test Method for J_{IC}, A Measure of Fracture Toughness," *Annual Book of ASTM Standards*, Vol. 03.01, American Society for Testing and Materials, Philadelphia, Pa., 1992.**

9. M. T. Kirk and R. H. Dodds, Jr., Martin Marietta Energy Systems, Inc., Oak Ridge National Laboratory, "Experimental and Analytical Investigation of the Shallow-Flaw Effect in Reactor Pressure Vessels," USNRC Report NUREG/CR-5886 (ORNL/TM-12115), July 1992.†

---

*Available for purchase from National Technical Information Service, Springfield, VA 22161.

†Available in public technical libraries.

‡Copies are available from U.S. Government Printing Office, Washington, DC 20402. ATTN: Regulatory Guide Account.

**Available from American National Standards Institute, 1430 Broadway, New York, NY 10018, Copyrighted.

3 Finite-Element Analysis of Cruciform Specimens

Three-dimensional elastic-plastic fracture analyses were performed for the cruciform specimen using the ABAQUS finite-element program.[1] Local crack-tip stress fields obtained from these analyses were used in applications of stress-based constraint characterization models (see Chaps. 4 and 5). In addition, CMOD and LLD responses from these analyses provide η-factors that, in turn, were used to determine fracture-toughness values for the cruciform specimen tests (see Chap. 2).

3.1 Model Description

Symmetry considerations dictate that a one-quarter section of the cruciform specimen be modeled in the FEA. The one-fourth section depicted schematically in Fig. 3.1 is represented in the 3-D finite-element model of Fig. 3.2, which consists of 18,650 nodes and 3,890 twenty-node isoparametric brick elements. Reduced integration was employed to enhance model flexibility and eliminate shear and volume locking, which can occur in fully integrated twenty-node elements under bending loading. Collapsed-prism elements arranged in a focused or centered fan configuration at the crack tip were used to produce a 1/r strain singularity appropriate for inelastic analysis. The cruciform specimen was assumed to be supported on a rigid plate under the test section [i.e., the area defined by (-51 mm $\le Z \le 0$, $0 \le X \le 51$ mm) in Fig. 3.1] and loaded by uniformly applied forces at the ends of the longitudinal/transverse arms (i.e., locations C and D in Fig. 3.1) to produce the uniaxial or biaxial bending conditions. The rigid support plate was incorporated into the finite-element model of Fig. 3.2 via interface or contact elements. Uniform end loads were achieved by applying uniformly distributed pressure loading over a narrow strip (10 mm) of elements at the ends of the model. Pressure loading distributed the load over the end of the load arms and enhanced solution convergence by eliminating localized plastic punching, which occurs when concentrated nodal forces are used.

The full geometry of the LDCS was represented in the finite-element model [Fig. 3.2(b)]. The slot geometry incorporated in the finite-element model was represented by the configuration of Fig. 3.3(b); it was used for all test specimens reported here except specimen BB-2, which utilized the slot configuration shown in Fig. 3.3(a). The model also incorporated a highly refined mesh in the crack-tip region [Fig. 3.2(c)] to provide resolution of stress fields over the normalized distance $2 \le r\sigma_0/J \le 5$ in front of the crack. Here σ_0 is the yield stress, and r is distance in the

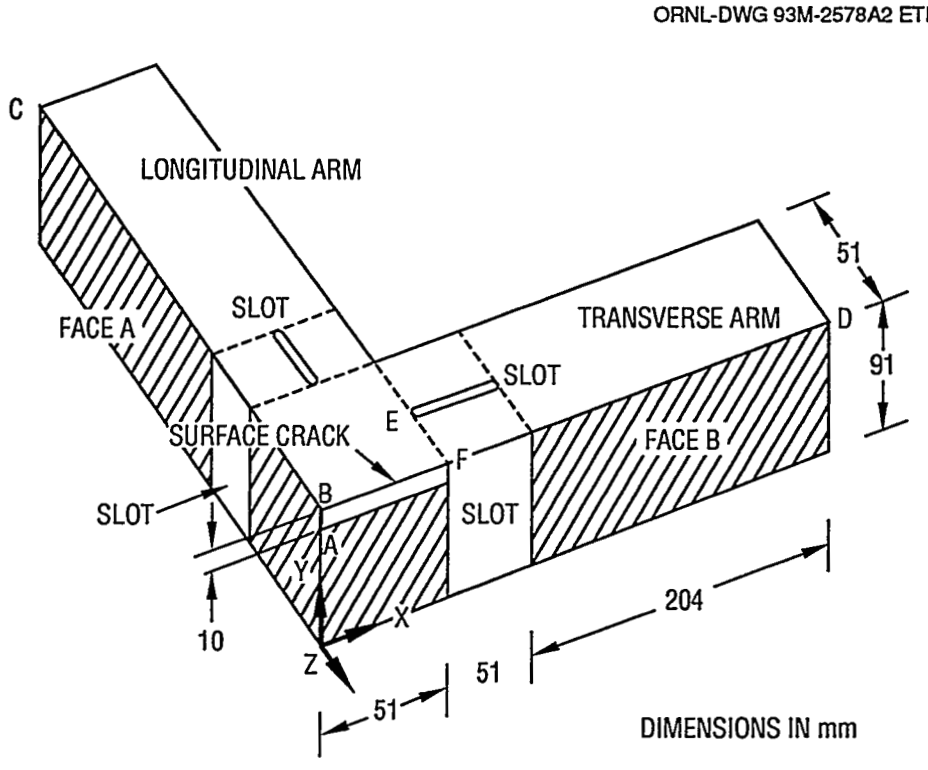

Figure 3.1 Definition of coordinate system and locations of interest for interpretation of finite-element results from analysis of HSST cruciform bend specimen

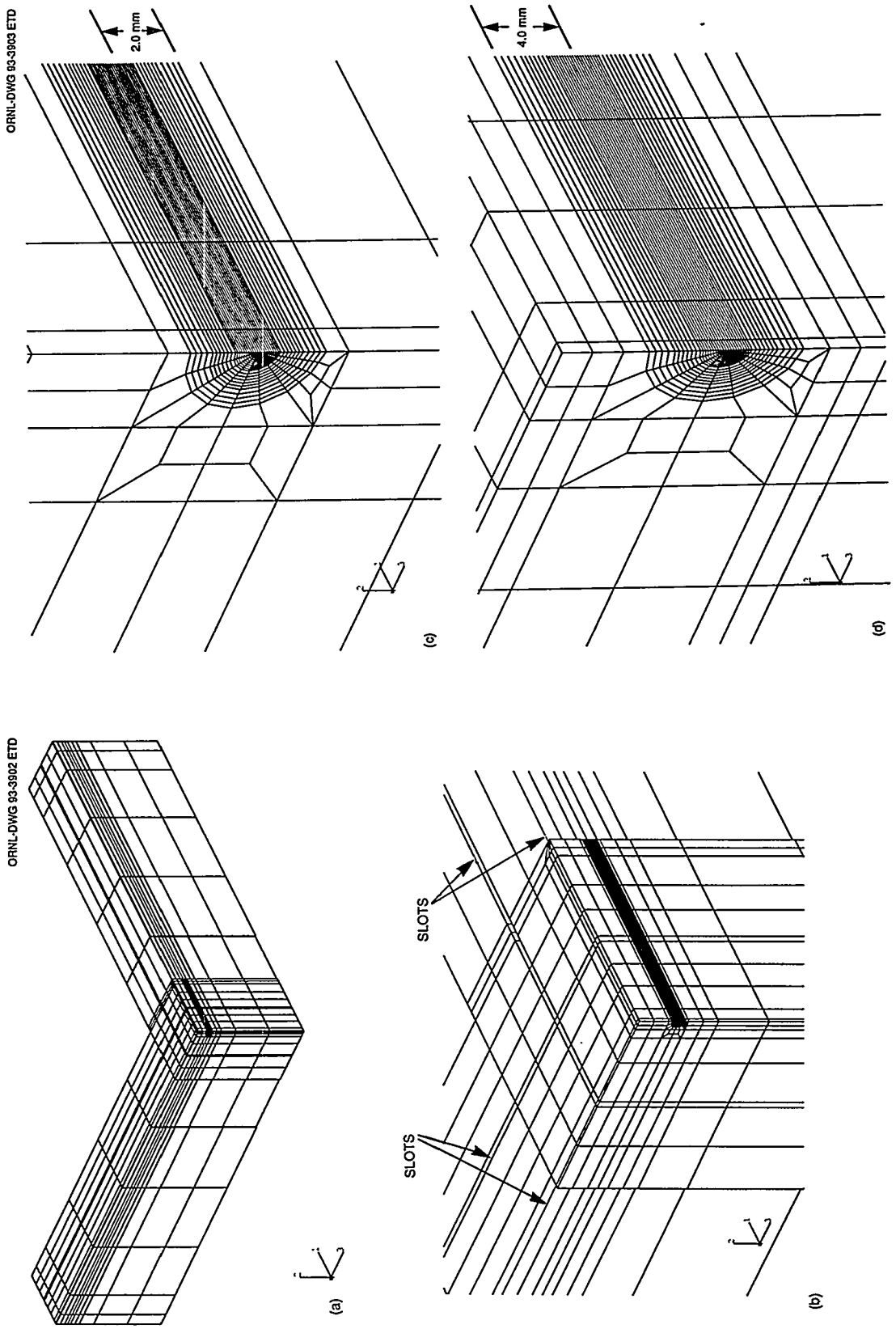

Figure 3.2 (a) Finite-element model for local crack-tip analyses of cruciform bend specimen, (b) test section region of finite-element model for cruciform bend specimen, (c) highly refined crack-tip region of finite-element model for cruciform bend specimen, and (d) finite-element model with expanded region of refinement near the crack tip.

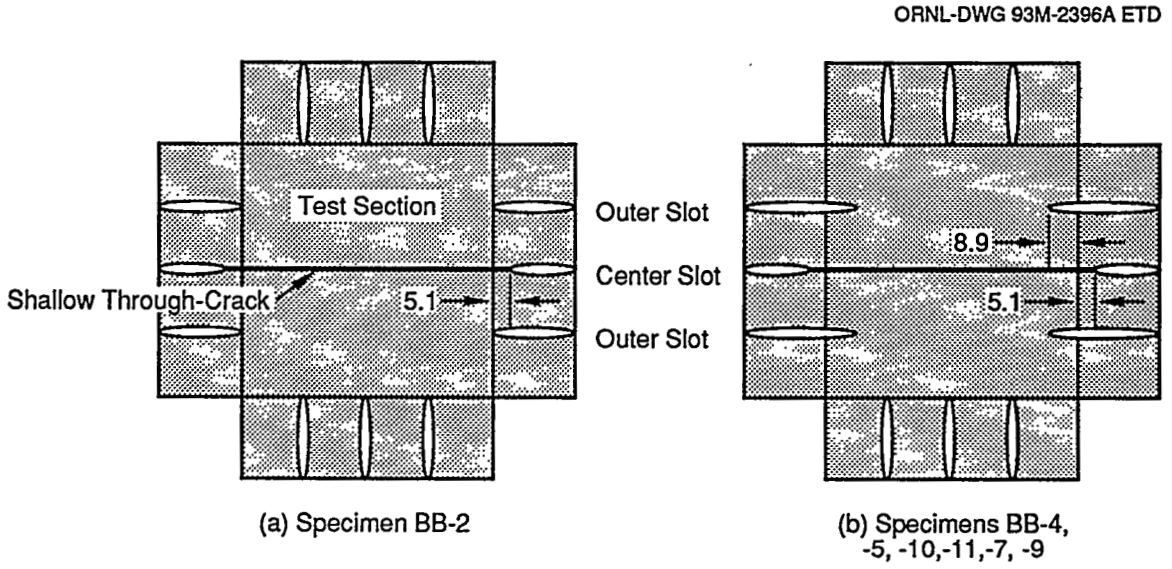

Figure 3.3 Slot configurations used for load diffusion control in cruciform specimens

crack plane measured from the initial crack tip. The range of 2 to 5 typically defines the region that contains the fracture process zone and is beyond the region of finite strain. A small strain analysis can thus be used. The outermost semicircular ring of nodes in the mesh of Fig. 3.2(c) has a radius of 2 mm, while elements immediately adjacent to the crack tip have a radial dimension of ~ 0.05 mm. The model of Fig. 3.2(c) was employed for the analysis of specimens BB-4 and BB-5, which were subjected to biaxial 0.6:1 loading. A second finite-element model, which employed the 4-mm ring of elements shown in Fig. 3.2(d), was utilized for specimens subjected to uniaxial 0:1 or biaxial 1:1 loading. The relatively higher failure loads (measured in terms of J) for the uniaxial 0:1 and biaxial 1:1 tests required an expanded region of refinement to resolve the stress at a normalized distance of $r\sigma_0/J = 5$.

3.2 Comparisons of Calculated and Measured Structural Response

Analyses were conducted for two sets of material properties (Fig. 3.4). The first set represented "estimated" properties for A 533 grade B class 1 steel at T = –40°C, taken from Refs. 2 and 3. The second set represented "measured" properties obtained from full material characterization tests (see Chap. 2). The "estimated" properties were used in the analytical crack-tip constraint studies presented in Ref. 3 and in initial fracture-toughness determinations for the cruciform specimen tests. The "measured" properties have only recently become available and were used to compute updated η-factors for implementation into final fracture-toughness calculations for the cruciform specimen tests. For both sets of material properties, softening beyond ultimate stress was modeled with perfect plasticity to facilitate numerical convergence.

Results from small-strain analyses of the cruciform specimens using "estimated" properties are compared with experimental results in Figs. 3.5 and 3.6. In Fig. 3.5, the calculated LLD response (measured at point C in Fig. 3.1) is compared with experimental data, while comparisons of calculated and experimental CMOD (measured at point B in Fig. 3.1) are presented in Fig. 3.6. As described in Ref. 3, the "estimated" properties were obtained by modifying material data from Ref. 2 to fit the LLD and CMOD response of the first uniaxially loaded cruciform specimen (BB-2). This specimen, however, had the transverse slot configuration shown in Fig. 3.3(a) rather than the slot configuration shown in Fig. 3.3(b), which was used in all subsequent tests. This slot design [Fig. 3.3(a)] is less compliant than the slot design of Fig. 3.3(b) as evidenced by comparing the experimental LLD and CMOD responses for tests BB-2 and BB-11, both uniaxially loaded specimens. While the calculated values for LLD and CMOD show good agreement with the experimental values for test BB-2, they give a somewhat stiff response relative to the experimental results for the remainder of the cruciform tests. In contrast, comparisons of analyses using the "measured" properties obtained from recent characterization studies with experimental results agree very well as demonstrated in Figs. 3.7–3.9. The

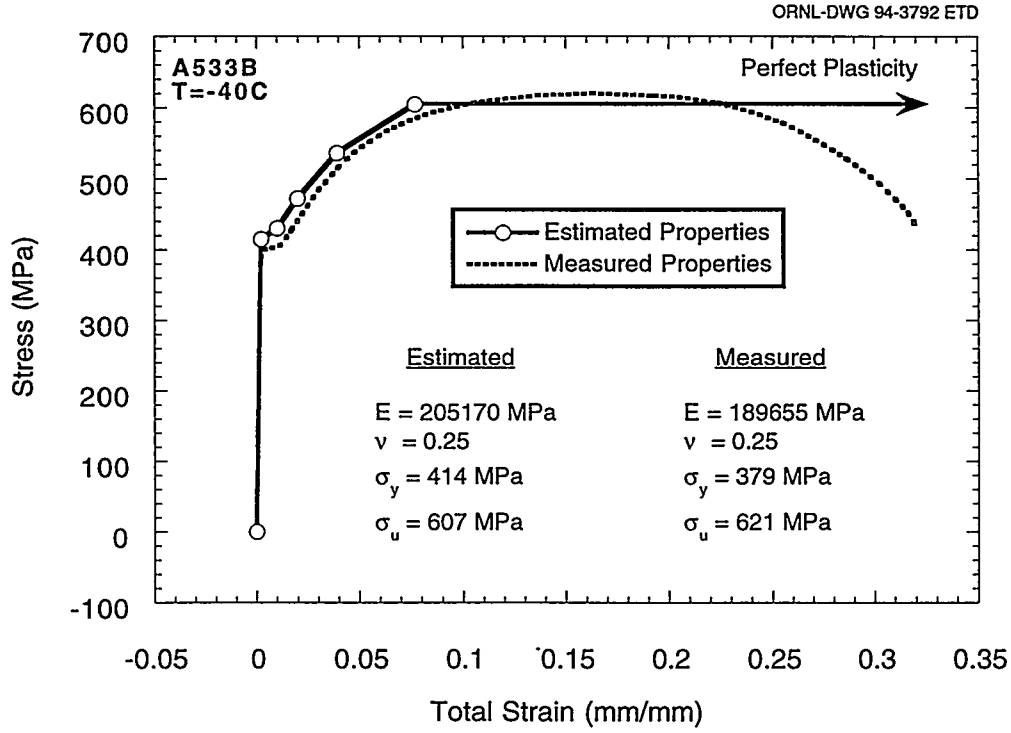

Figure 3.4 Material representation for A 533 B steel at T = –40°C

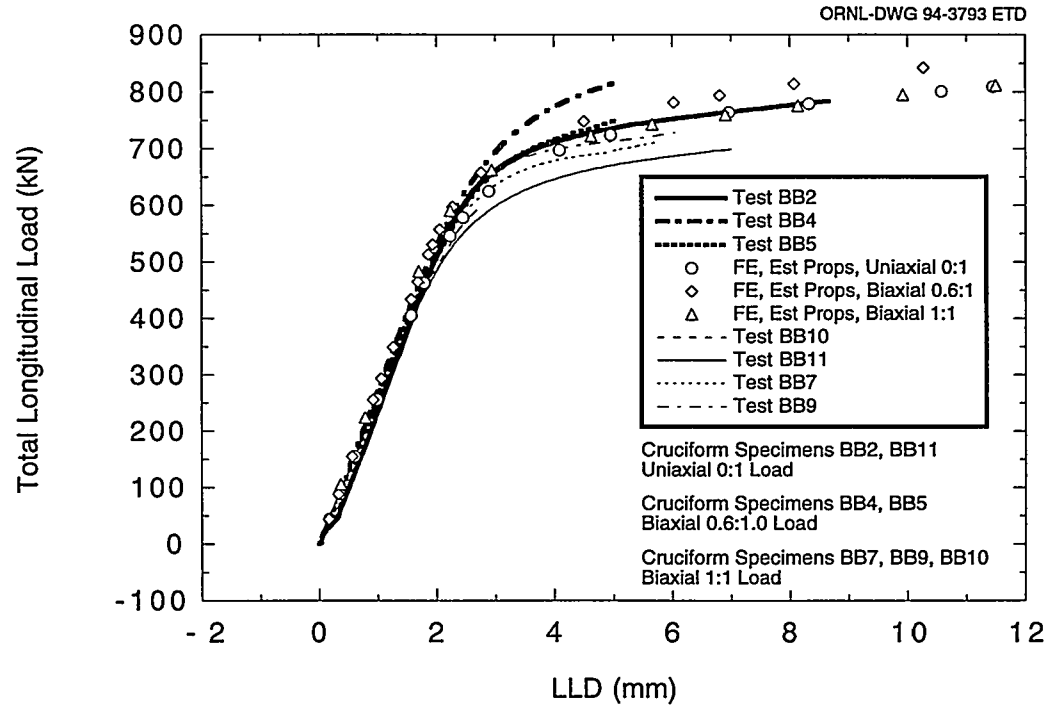

Figure 3.5 Comparison of calculated and experimental results for LLD using estimated material properties in analysis

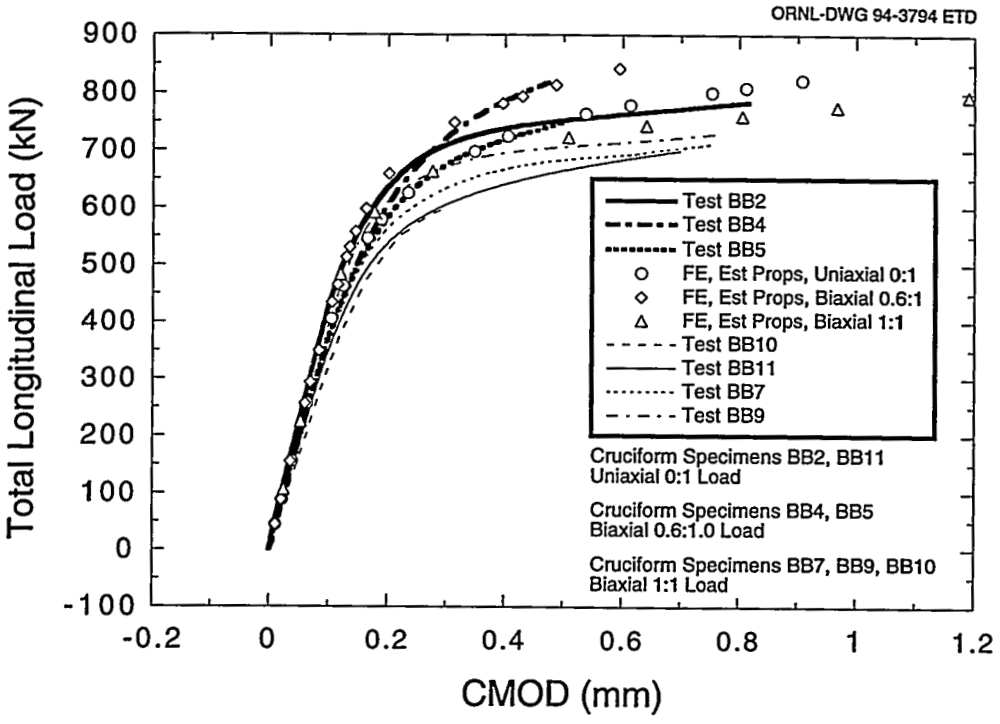

Figure 3.6 Comparison of calculated and experimental results for CMOD using estimated material properties in analysis

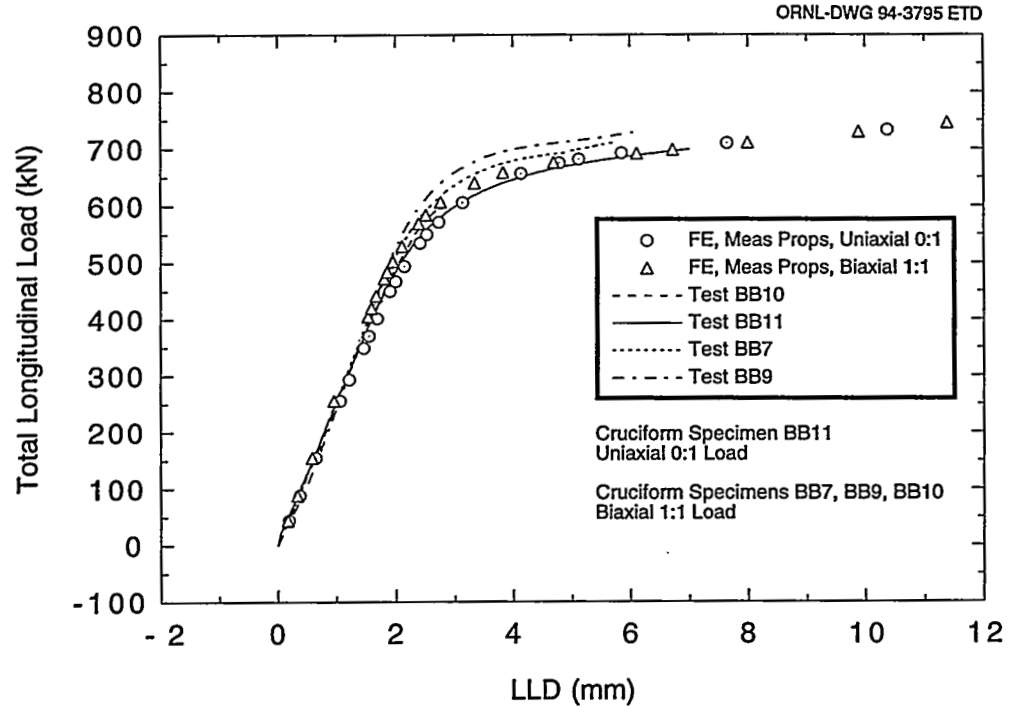

Figure 3.7 Comparison of calculated and experimental results for LLD using measured material properties in analysis

Finite-Element

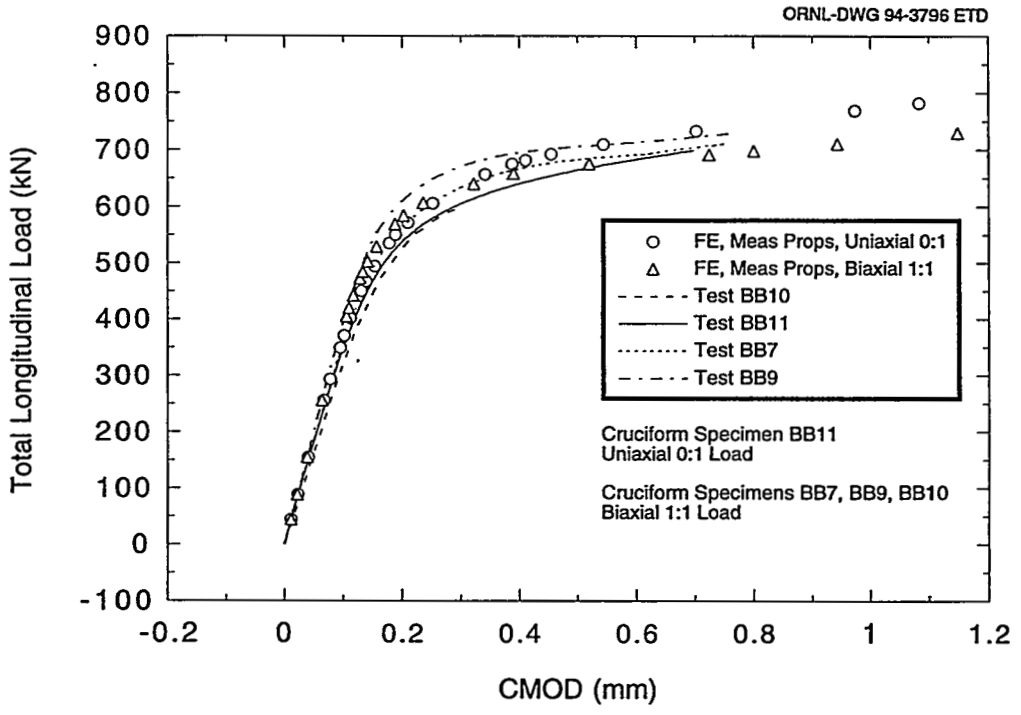

Figure 3.8 Comparison of calculated and experimental results for CMOD using measured material properties in analysis

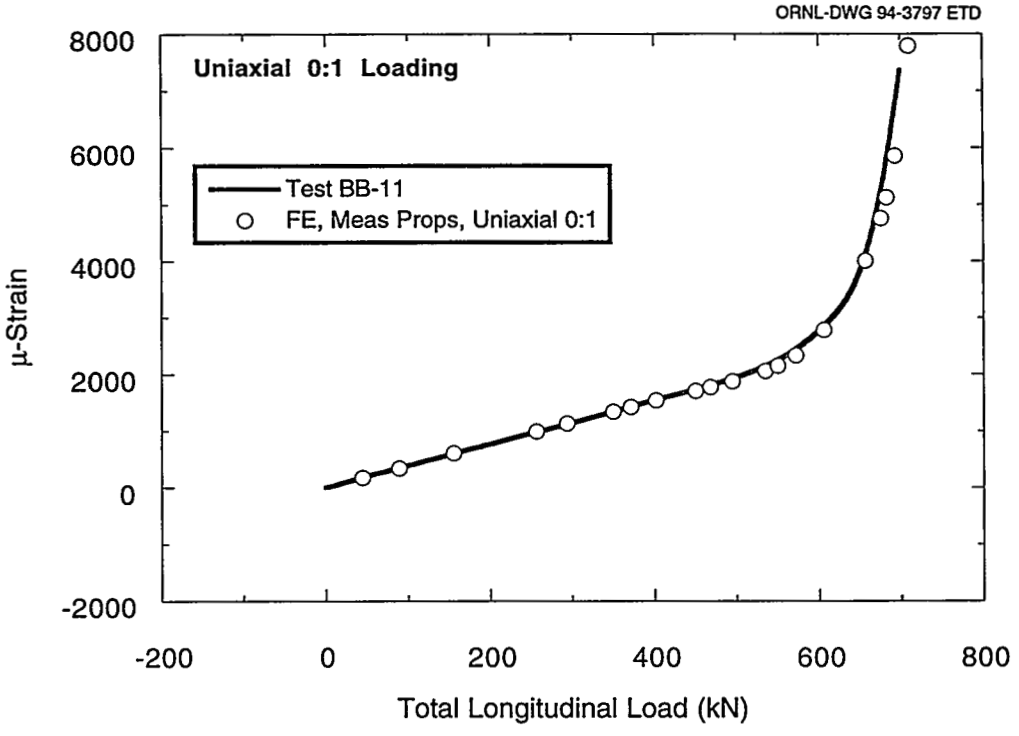

Figure 3.9 Comparison of calculated and experimental opening-mode strain on top center of specimen 32 mm from crack plane, uniaxial 0:1 loading

calculated CMOD responses shown in Fig. 3.8 using "measured" material properties were used to update all fracture-toughness results presented in Table 2.2 for the cruciform specimen tests (see Chap. 2). The self-contained analytical constraint studies presented in Ref. 3, as well as those that follow in Chap. 4, however, utilize calculations that employed the "estimated" material properties. Time considerations did not permit redoing the labor-intensive analytical constraint calculations with the more appropriate "measured" material properties. It is not anticipated, however, that the basic conclusions drawn in Chaps. 4 and 5 would be altered by this approach.

3.3 Calculations of Applied J and K_J Using Estimated Material Properties

The applied J vs longitudinal load values at two positions along the crack front, X = 0 mm and 26 mm (measured from the midplane), are given in Figs. 3.10 and 3.11. These results illustrate a lower J-value computed for specimens subjected to biaxial 0.6:1 loading at failure compared to uniaxial loading, but conversely they show higher J-values for biaxial 1:1 loading relative to uniaxial loading near failure. This is shown in Fig. 3.12, which is a cross plot of the plastic component of J vs biaxial load ratio for three different arbitrary load levels. The effect of out-of-plane stress on J is then not a direct consequence of the magnitude of that out-of-plane stress as one might intuitively assume. Studies are currently under way to resolve the relationships between load level, biaxiality ratio, J_{pl}, development of plastic zone, etc., for this specimen geometry. Figures 3.13–3.15 depict the variation of K_J (K from J assuming plane strain) along the crack front for uniaxial 0:1, biaxial 0.6:1, and biaxial 1:1 loading, respectively. Each figure is plotted to the same scale to emphasize the difference in absolute value of K_J for the three loadings. In each figure, as the failure load is approached, the crack-driving force across the middle half of the crack

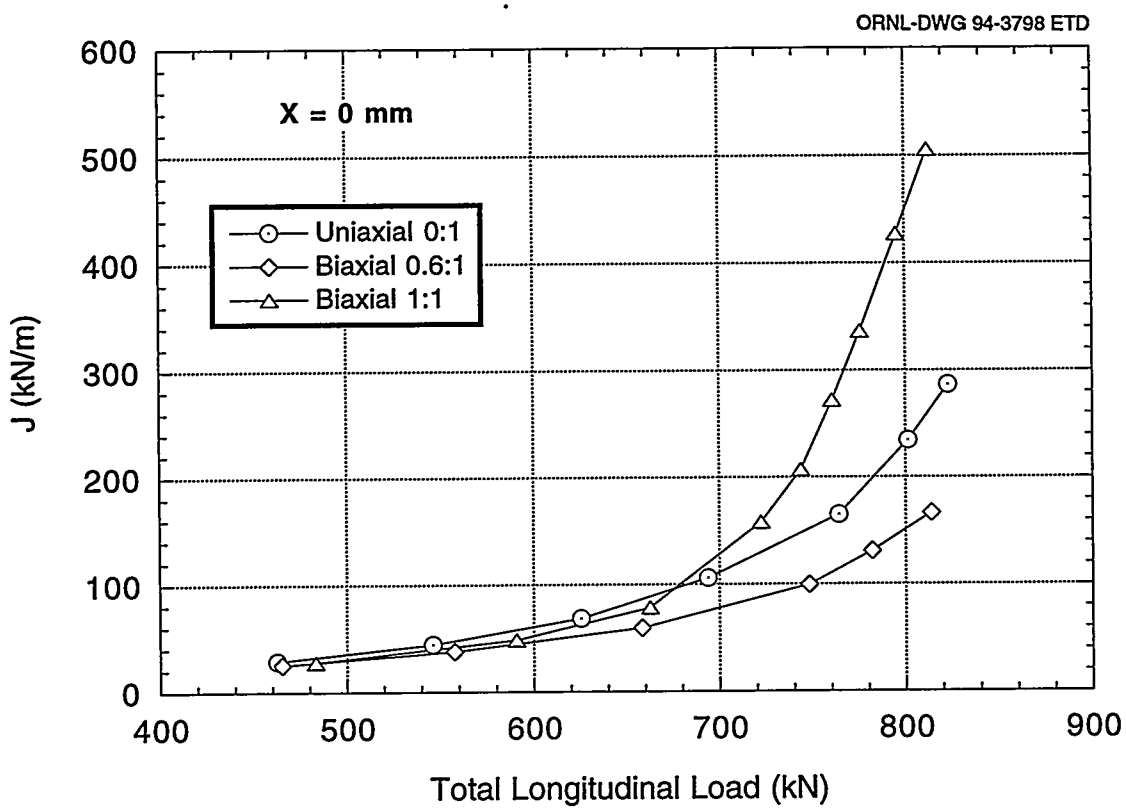

Figure 3.10 Applied J at X = 0 mm using estimated material properties in analysis

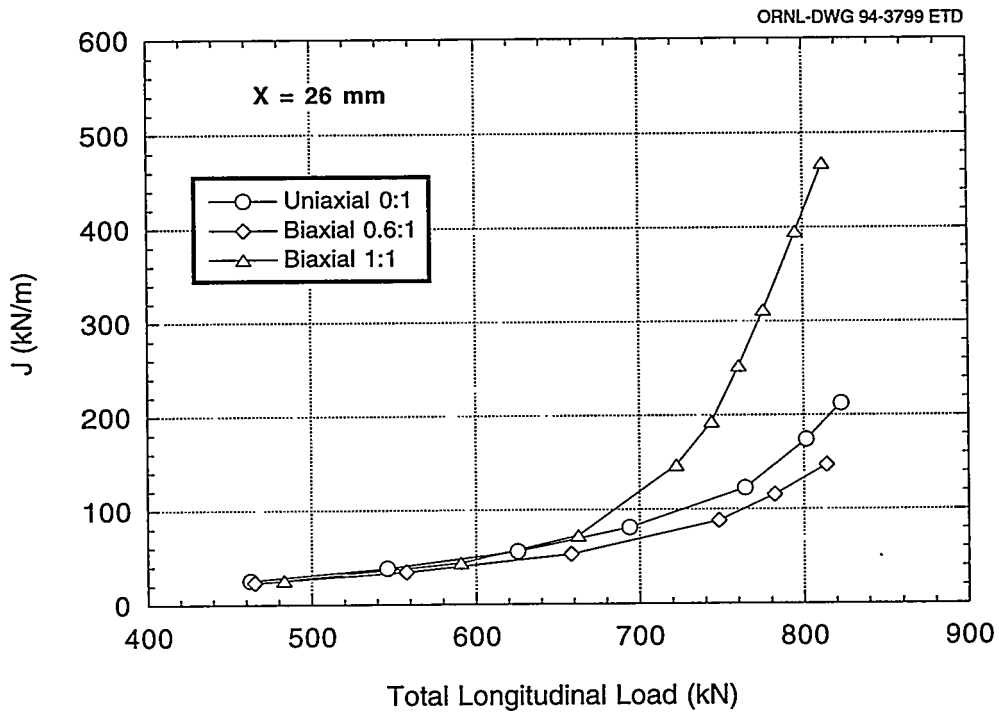

Figure 3.11 Applied J at X = 26 mm using estimated material properties in the analysis

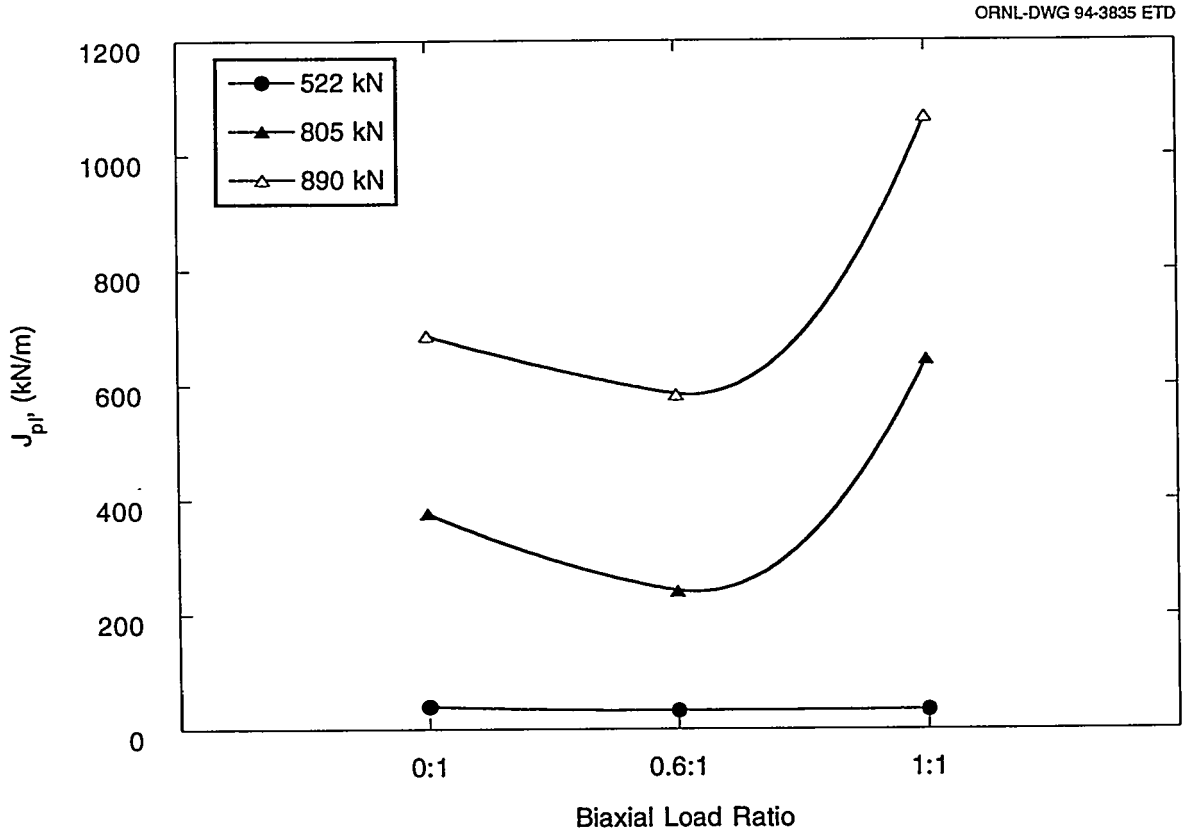

Figure 3.12 Effect of biaxial load ratio on the plastic component of J

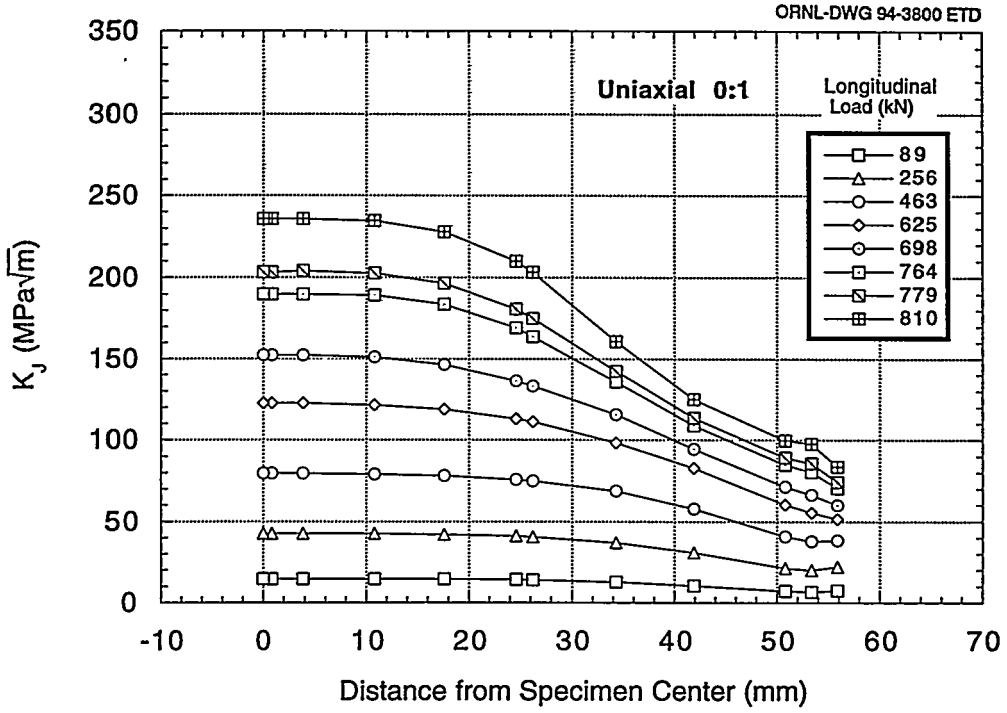

Figure 3.13 Variation of K_J along crack front using estimated material properties in analysis, uniaxial 0:1 loading

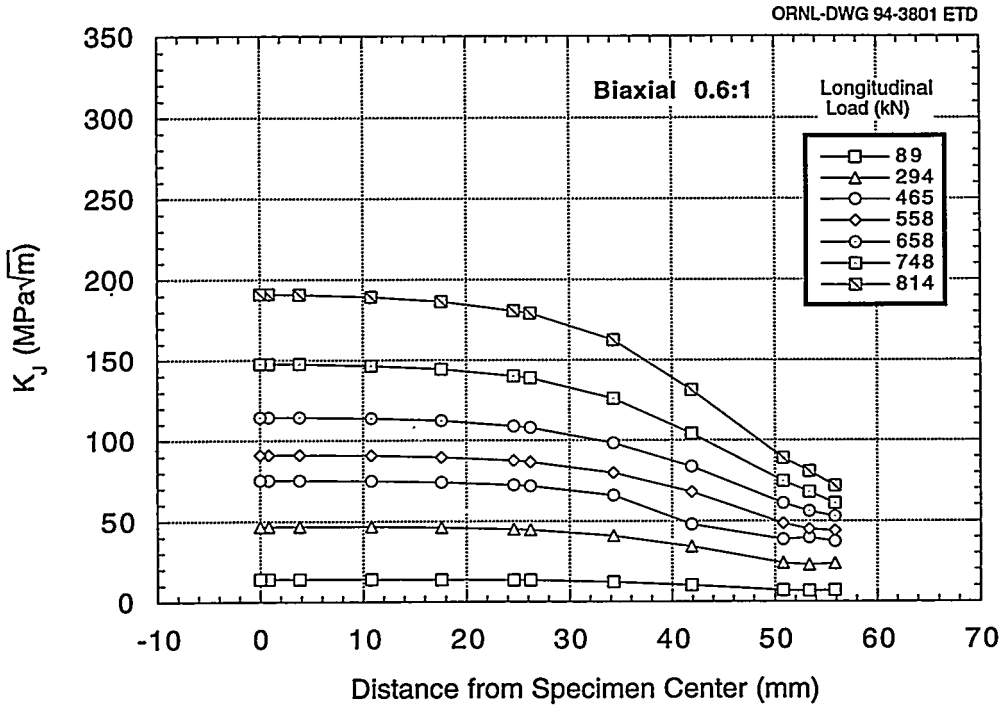

Figure 3.14 Variation of K_J along crack front using estimated material properties in analysis, biaxial 0.6:1 loading

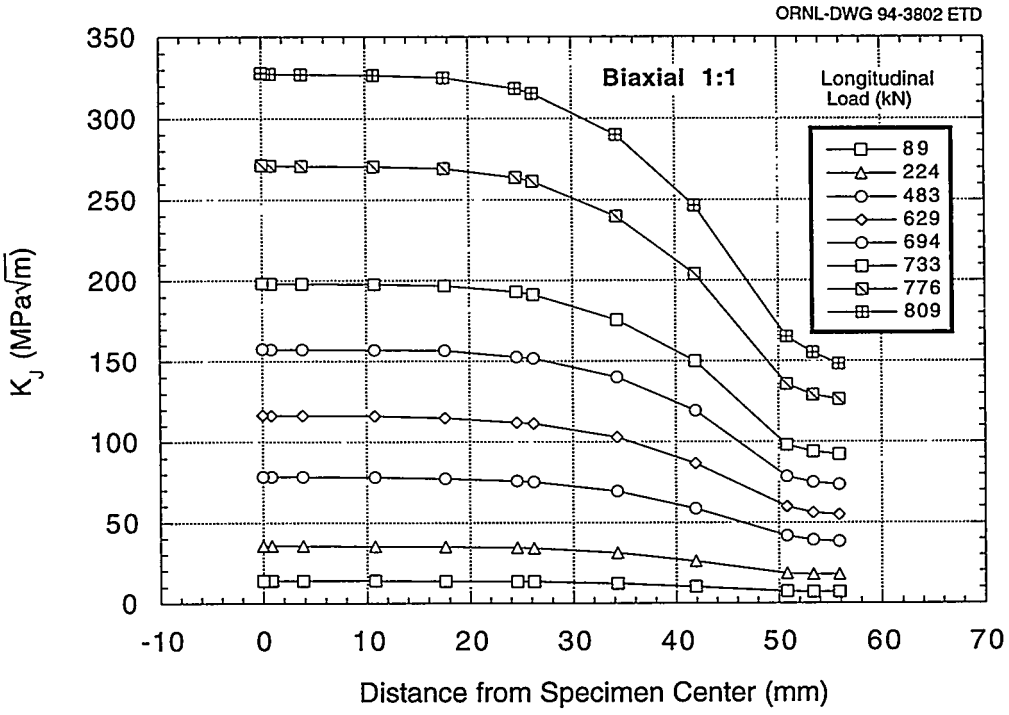

Figure 3.15 Variation of K_J along crack front using estimated material properties in analysis, biaxial 1:1 loading

front remains relatively uniform but decreases dramatically toward the ends of the crack. The slot configuration was designed to obtain this behavior to minimize the potential for crack initiation at the ends of the slots.

References

1. *ABAQUS Theory Manual*, Version 5.3, (Hibbitt, Karlson, and Sorenson, Inc., Providence, Rhode Island, 1993).

2. D. J. Naus et al., Martin Marietta Energy Systems, Inc., Oak Ridge National Laboratory, "High-Temperature Crack-Arrest Behavior in 152-mm-Thick SEN Wide Plates of Quenched and Tempered A 533 Grade B Class 1 Steel," USNRC Report NUREG/CR-5330 (ORNL/TM-11083), April 1989.*

3. B. R. Bass et al., Martin Marietta Energy Systems, Inc., Oak Ridge National Laboratory, "Biaxial Loading and Shallow-Flaw Effects on Crack-Tip Constraint and Fracture Toughness," USNRC Report NUREG/CR-6132 (ORNL/TM-12498), January 1994.*

*Available from National Technical Information Service, Springfield, VA 22161

4 Interpretation and Discussion of Results

4.1 Effects of Biaxial Loading

Initial tests in the HSST investigation of biaxial loading effects on fracture toughness in the transition temperature region were carried out using cruciform specimens fabricated from a single heat of A 533 B steel. These specimens were tested and analyzed according to the techniques described within Chaps. 2 and 3, respectively. Tests were performed for conditions of uniaxial loading and for biaxial 0.6:1 and 1:1 loading ratios. Fracture-toughness data obtained from testing and analysis of the cruciform specimens are given in Fig. 4.1 as a function of the biaxiality loading ratio. The plot indicates a pronounced reduction in the lower-bound shallow-crack fracture toughness as the biaxiality ratio is varied from 0:1 to 1:1. As the biaxiality ratio approaches 1:1, the lower bound to the shallow-crack toughness approaches that derived from SENB uniaxial deep crack data[1] for A 533 B steel. These data also indicate a trend of decreasing scatter for a stress ratio of 0.6:1 when compared with the data scatter observed in the uniaxial SENB shallow-crack tests and in the biaxial 1:1 tests. In summary, the limited biaxial toughness data base, depicted in Fig. 4.1, provides evidence of a significant biaxial loading effect on cleavage fracture toughness in the the transition temperature region for RPV steels.

4.2 Dual-Parameter Fracture-Toughness Characterization

Current fracture prevention technology relies on the use of fracture correlation parameters (K or J) to characterize both the applied loading and the resistance of engineering materials to crack initiation. Shortcomings of these conventional one-parameter fracture correlation methods, which have been well-documented in numerous references (e.g., see Refs. 2–5), are being addressed through development of various dual-parameter fracture methodologies. Determinations are being made within the HSST Program concerning the bounds of applicability of both stress-based and stress-strain-based dual-parameter correlation models. The emphasis in these studies is placed on applications to measured data generated from both uniaxially and biaxially loaded shallow-crack fracture specimens. A major objective is to determine the effectiveness of the various

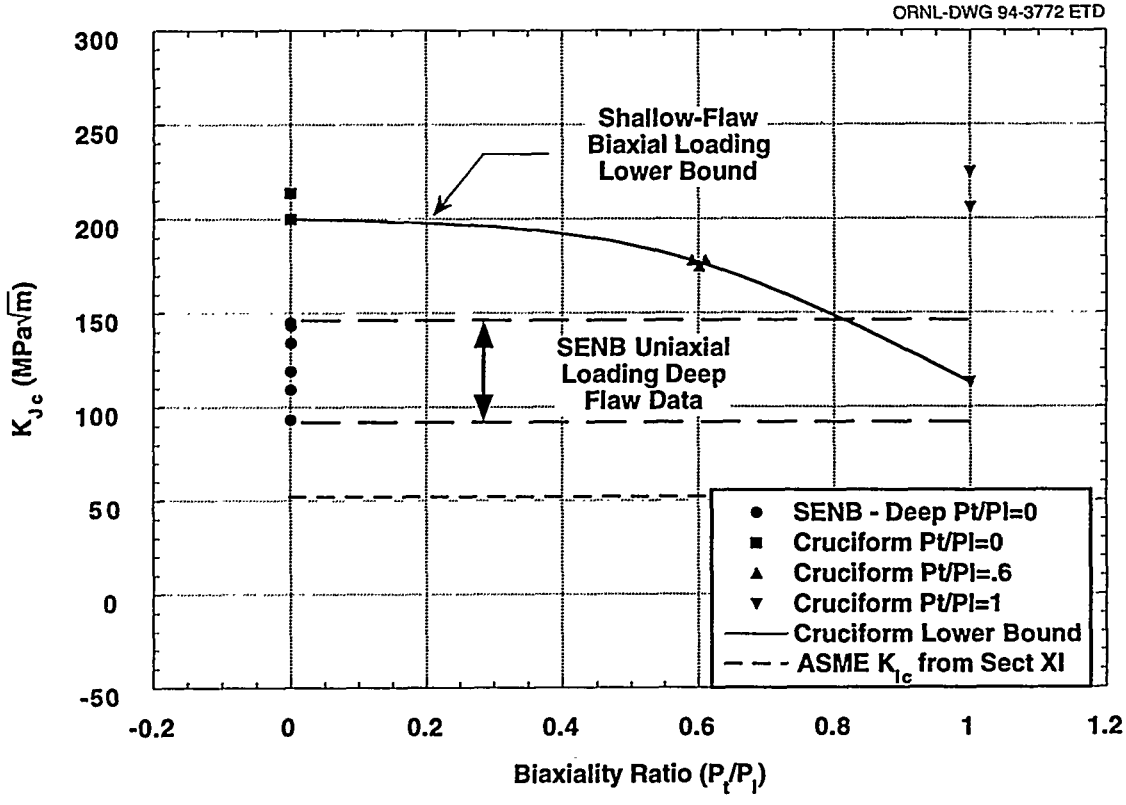

Figure 4.1 Reduction in lower-bound toughness values as function of biaxiality ratio for single heat of A 533 B steel

methodologies in correlating measured toughness data in the transition temperature region of RPV steels.

4.2.1 Stress-Based Methodologies

Two stress-based dual-parameter methodologies that have been investigated within the HSST Program are the J-Q methodology of O'Dowd and Shih,[6–8] combined with the RKR fracture criteria,[9] and the Dodds-Anderson (D-A) constraint correction technique.[2,10–11] These two fracture methodologies share the common feature of utilizing the effects of crack-tip constraint on in-plane stresses at the crack tip to infer the effect of constraint on fracture toughness. In Ref. 12, both the J-Q methodology and the D-A constraint scaling model were applied to shallow- and deep-crack SENB specimens[1] and to uniaxially and biaxially loaded cruciform specimens. Analysis results from these applications indicated that both methodologies could be used successfully to interpret experimental data from the shallow- and deep-crack uniaxially loaded SENB specimen tests. Figures 4.2 and 4.3 summarize an application of the D-A constraint correction model to fracture-toughness data from the HSST shallow-crack SENB program. In Fig. 4.2, the shallow- and deep-crack toughness data are plotted as a function of crack depth for a normalized temperature range of –10°C to –25°C. As expected in a low-constraint geometry, Fig. 4.2 shows both an increase in the mean fracture-toughness value and in data scatter from the shallow-crack specimens when compared with the deep-crack specimens. The corresponding toughness data, following application of the D-A correction model, are shown in Fig. 4.3. The regression analysis shown in Fig. 4.3 implies that the corrected toughness data are essentially independent of crack depth.

Applications of the J-Q and D-A constraint methodologies to the uniaxially and biaxially loaded cruciform specimens in Ref. 12 yielded results that were considerably more difficult to interpret than those of the SENB specimens. The uniaxially loaded cruciform specimen analyzed in Ref. 12 failed at a sufficiently high load that the far-field bending stress began to impinge on the near-tip stress fields, a factor that rendered the J-Q results inconclusive. A modified D-A scaling procedure employed in Ref. 12 resulted in a J_{FB}/J_0 ratio (J_{FB} = J finite body; J_0 = J infinite body) for biaxial 0.6:1 loading that was ~ 25% greater than that for uniaxial loading. This implies a greater constraint loss for biaxial 0.6:1 loading than for uniaxial loading, a result inconsistent with toughness determined from the experimental data. However, these results from the D-A approach were obtained using an engineering model developed by Dodds et al.[2] that approximates the scaling

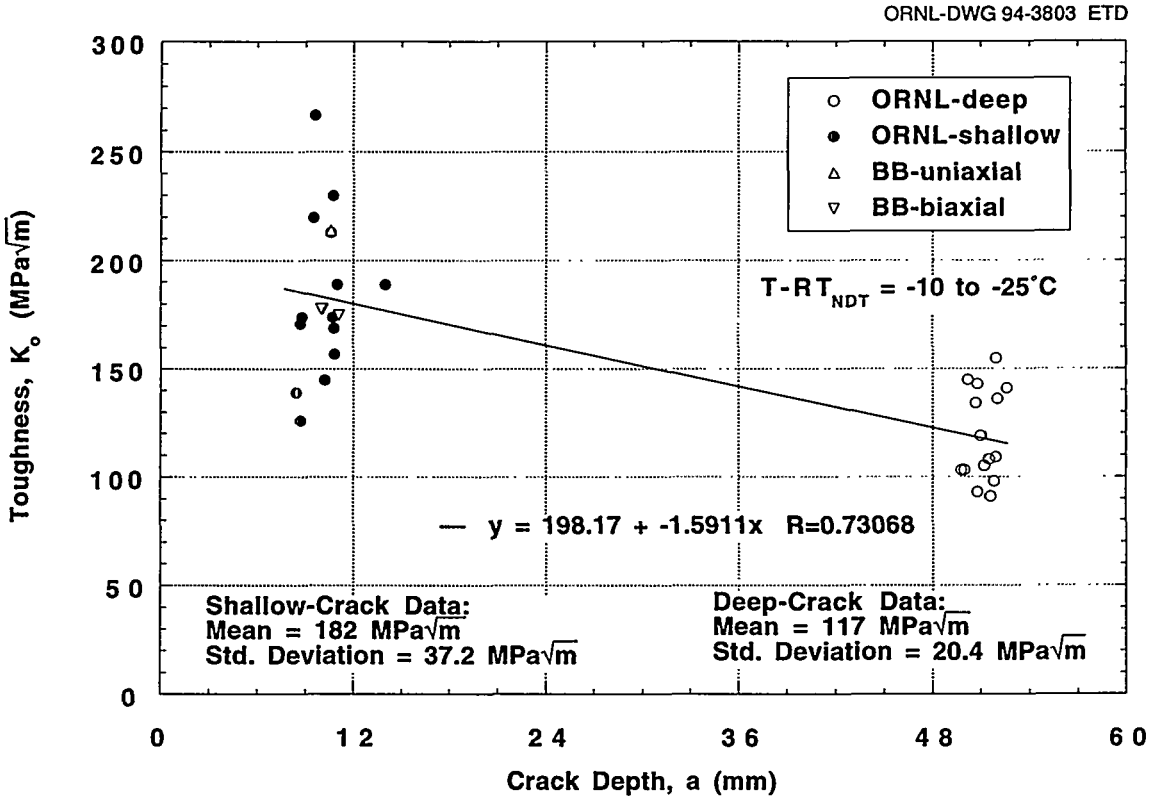

Figure 4.2 Mean value and scatter in toughness data increasing for deep-crack specimens as compared to shallow-crack specimens

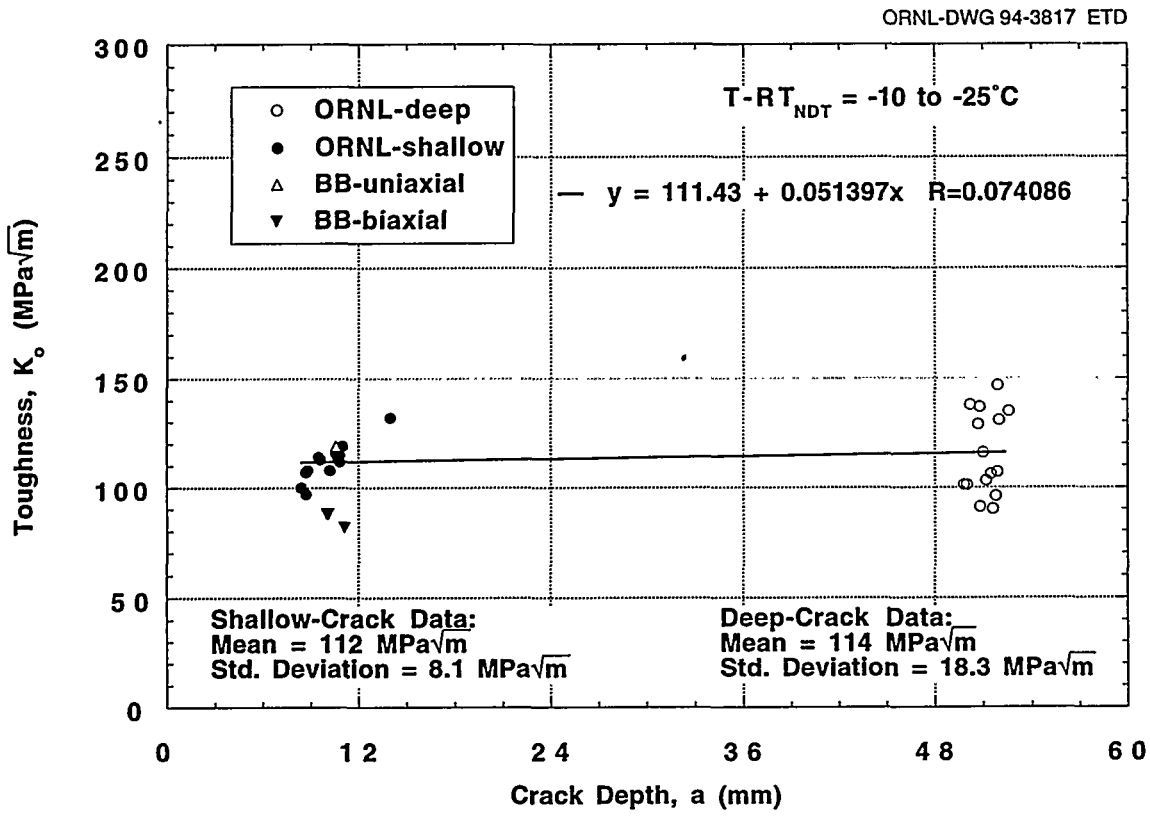

Figure 4.3 D-A constraint adjustment procedure applied to SENB data predicting no change in toughness with crack depth

factors (J_{FB}/J_0) of the original D-A model. In the original formulation,[11] toughness data are adjusted to small-scale yielding (SSY) values based on ratios of areas (or volumes) within principal stress contours around the crack tip. The engineering model applied to the cruciform specimens approximates these ratios using the stress distribution in the crack plane directly ahead of the crack tip that draws upon a J-Q description of the crack-tip fields. Thus, the engineering model assumes that the stressed areas are similarly shaped, allowing the comparison of distances ahead of the crack rather than areas (or volumes). In Ref. 12, the possibility was raised that the engineering model may not be suitable for the cruciform specimen that possesses 3-D stress fields that vary through the thickness of the test section.

Because of these uncertainties concerning applications of the D-A engineering model in Ref. 12, the cruciform bend specimen was re-analyzed using the original formulation of the D-A scaling model based on stressed areas and volumes. Maximum principal stress contours in the range $2.5\sigma_0$ to $2.8\sigma_0$ (σ_0 = yield stress) enclose critical areas (or volumes) ahead of the crack tip, that is, where cleavage fractures initiate. For the present study, maximum principal stress contours defined by $\sigma_1/\sigma_0 = 2.5$ were obtained at several positions along the crack front for a number of load steps [up to 845 kN (190 kips) longitudinal load] using ABAQUS-POST. The contour areas were then determined and plotted against the ABAQUS computed J-values for the respective crack front location and load value. From these curves, J-values for uniaxial and biaxial loading that give the same stressed areas can be determined and plots of J_b vs J_u can then be constructed (J_b is J for the biaxially loaded specimen, and J_u is J for the uniaxially loaded specimen).

The following results were obtained from application of the D-A scaling procedure to the biaxial 0.6:1 loading case: (1) self-similar principal stress areas were obtained with increasing load for both uniaxial and biaxial loading; (2) both maximum principal stress areas and J were essentially constant for the center 38 mm (1.5 in.) of the specimen, and then both area and J decreased rapidly as the crack-slot juncture was approached; (3) on average, the fact that J_b was somewhat greater than J_u agrees with the "modified" procedure employed in Ref. 12 and implies greater constraint loss for biaxial 0.6:1 loading than for uniaxial loading. This result is contrary to the experiments to date. A comparison of the results for J_b vs J_u is shown in Fig. 4.4 for the biaxial 0.6:1 loading case.

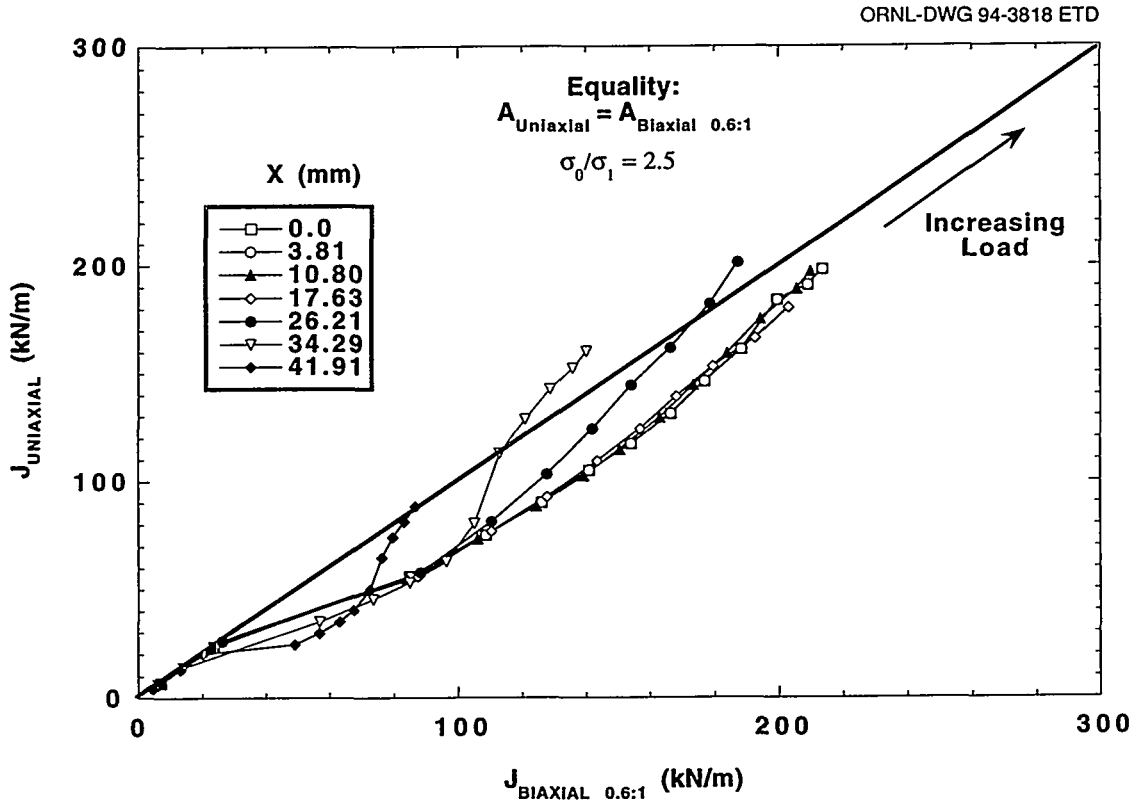

Figure 4.4 Validation check on D-A constraint correction for ORNL biaxial (0.6:1) and uniaxial (0:1) tests

The D-A scaling procedure was also applied to biaxial 1:1 loading in light of the significantly reduced toughness result obtained in one of the tests (BB-10). A comparison of the D-A scaling procedure for J_b vs J_u is shown in Fig. 4.5 for the biaxial 1:1 loading case. Because the D-A methodology predicts a small biaxial effect on constraint, the predicted failure J for biaxial loadingw is essentially equal to the measured value for uniaxial loading. However, the predicted J value is substantially higher than the measured J from the lower-bound toughness of the biaxial 1:1 loading experiments (see Fig. 4.1).

The implication of the foregoing results, and those described in Ref. 12, is that the D-A and J-Q methodologies that are applied to in-plane stress fields at the crack tip do not adequately describe the effect of biaxial loading on fracture toughness. In an attempt to better understand these results, additional FEAs were performed on the cruciform specimen to clarify the relationship between biaxial loading ratio and development of the stress fields and plastic zone in the near crack-tip region. The stress components referenced in this discussion are calculated at the nodal location (N-5006), identified in Fig. 4.6, at a distance r = 2.54 mm (0.1 in.) from the crack tip; the coordinate system is given in the same figure.

Analysis results indicate that the point located at r = 2.54 mm (0.1 in.) experiences yielding at different load levels, depending on the out-of-plane loading ratio. According to the von Mises yield criterion, yielding occurs when the second deviatoric stress invariant, J_2, reaches a critical value,

$$\sqrt{J_2} = K \ ,$$

where

$$J_2 = (1/6)[(P_1 - P_2)^2 + (P_2 - P_3)^2 + (P_3 - P_1)^2] \ .$$

Here, P_1, P_2, and P_3 are the principal stresses. The above yield criterion can be written in terms of the effective stress, σ_{eff}, according to

$$\sigma_{eff} = \sqrt{(3 \cdot J_2)} = \sqrt{3} \cdot K \ .$$

The Mises effective stress and, consequently, the yield criterion are governed by the differences in the principal stresses.

Relevant stress components (Cartesian normal stresses, hydrostatic stress, and Mises effective stress) are plotted in

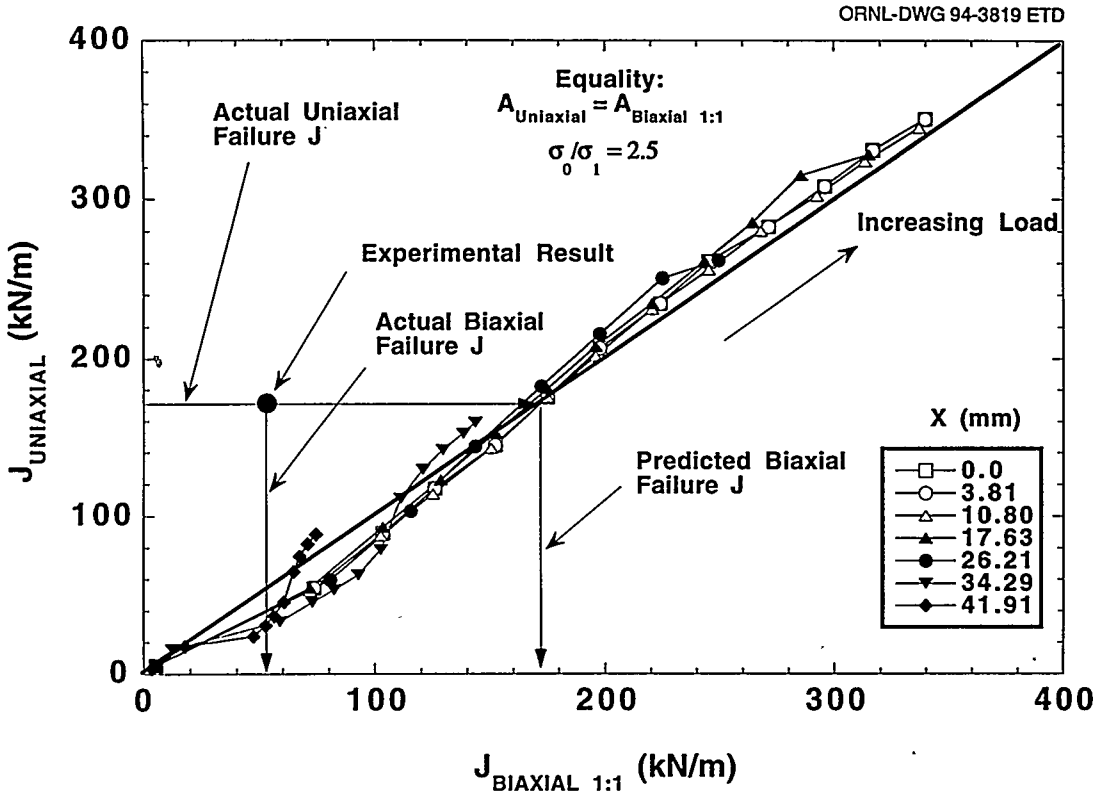

Figure 4.5 Validation check on D-A constraint correction for ORNL biaxial (1:1) and uniaxial (0:1) tests

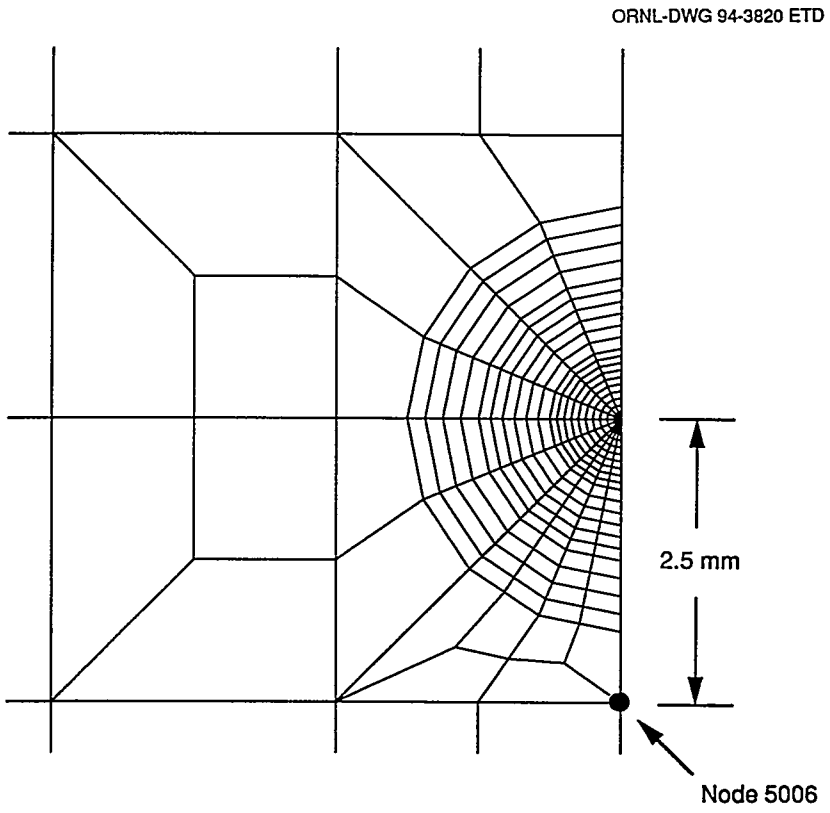

Figure 4.6 Stress components examined at material point (node 5006) 2.54 mm (0.100 in.) ahead of crack tip

Figs. 4.7–4.9 to provide a better understanding of plastic zone development in the cruciform specimen. In Figs. 4.7–4.9, the Cartesian normal stress components (σ_{11}, σ_{22}, σ_{33}) represent good approximations to the magnitude of the principal stress values (the shear stress components are small). Applications of increasing ratios for out-of-plane to in-plane loading are accompanied by substantial elevations of the hydrostatic stress and the out-of-plane normal stress (σ_{11}). In contrast, the in-plane normal stress components (σ_{22}, σ_{33}) do not change a great deal as a function of load ratio, except at the highest load levels.

Development of the plastic zone can be correlated with the applied biaxial loading ratio and resultant out-of-plane normal stress component (σ_{11}). For the 0:1 (uniaxial) loading case (Fig. 4.7), the out-of-plane component is well below the two in-plane components, and the onset of yielding occurs at a relatively low applied load. When the out-of-plane load is increased to a 0.6:1 ratio (Fig. 4.8), the out-of-plane component roughly tracks the lower in-plane component up to 580 kN (130 kips) and then begins to increase at a substantially higher rate. The effect of the 0.6:1 load ratio is to delay the onset of yielding to a much higher load [~756 kN (170 kips)] than was observed in the 0:1 load case.

For the 1:1 load case (Fig. 4.9), the out-of-plane component (σ_{11}) turns up and essentially tracks the opening-mode (maximum) stress component (σ_{33}) beyond the 667-kN (150-kip) load level. Also, the normal stress components (σ_{11}, σ_{33}) and the hydrostatic stress are observed to increase at a greater rate beyond 667 kN (150 kips). [In this load range, observe that the hydrostatic and the out-of-plane stresses for the 1:1 load case are substantially elevated above those of the 0.6:1 case (see Fig. 4.8).] Near the 667-kN (150-kip) level, the plastic zone width progresses abruptly through N-5006, and the node exhibits significant strain hardening. An increase in differences between principal stress components is reflected in the increasing Mises effective stress.

In summary, Figs. 4.7–4.9 illustrate that increasing the out-of-plane to in-plane biaxial loading ratio from 0:1 to 1:1 results in a dramatic increase of the out-of-plane normal stress component, while the two in-plane components remain relatively unchanged (except at the highest loads). Thus, far-field biaxial stresses have little effect on in-plane stresses in the cruciform specimen. This effect is further illustrated in Fig. 4.10 that depicts the variation of stress components at N-5006 with far-field biaxial stress ratio. As a consequence, conventional stress-based cleavage fracture

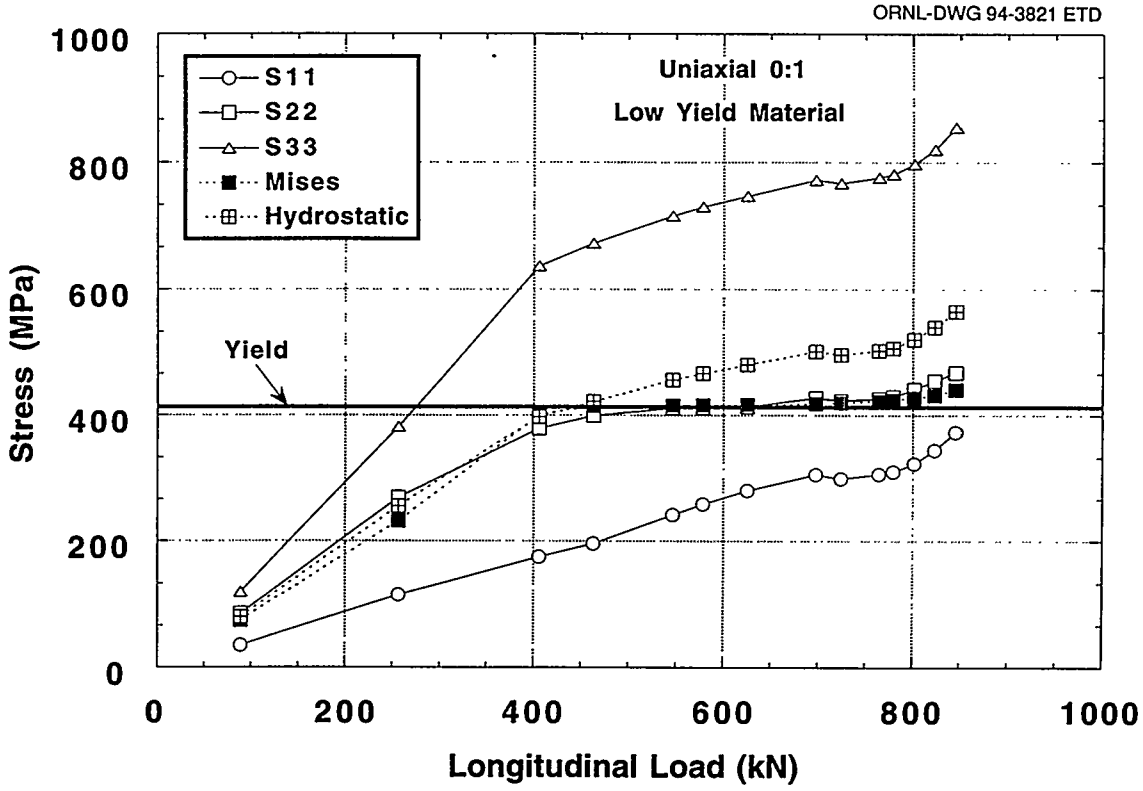

Figure 4.7 Stress components at material point 2.54 mm ahead of crack tip for uniaxial 0:1 loading

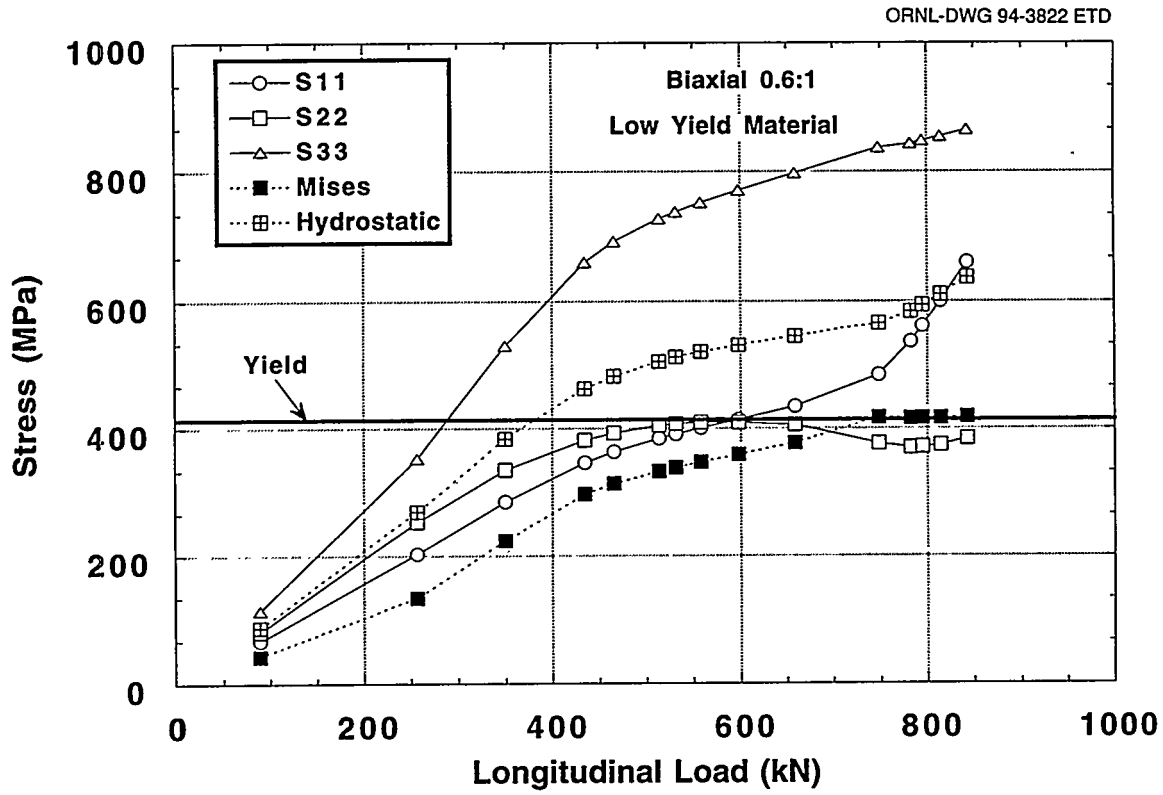

Figure 4.8 Stress components at material point 2.54 mm ahead of crack tip for biaxial 0.6:1 loading

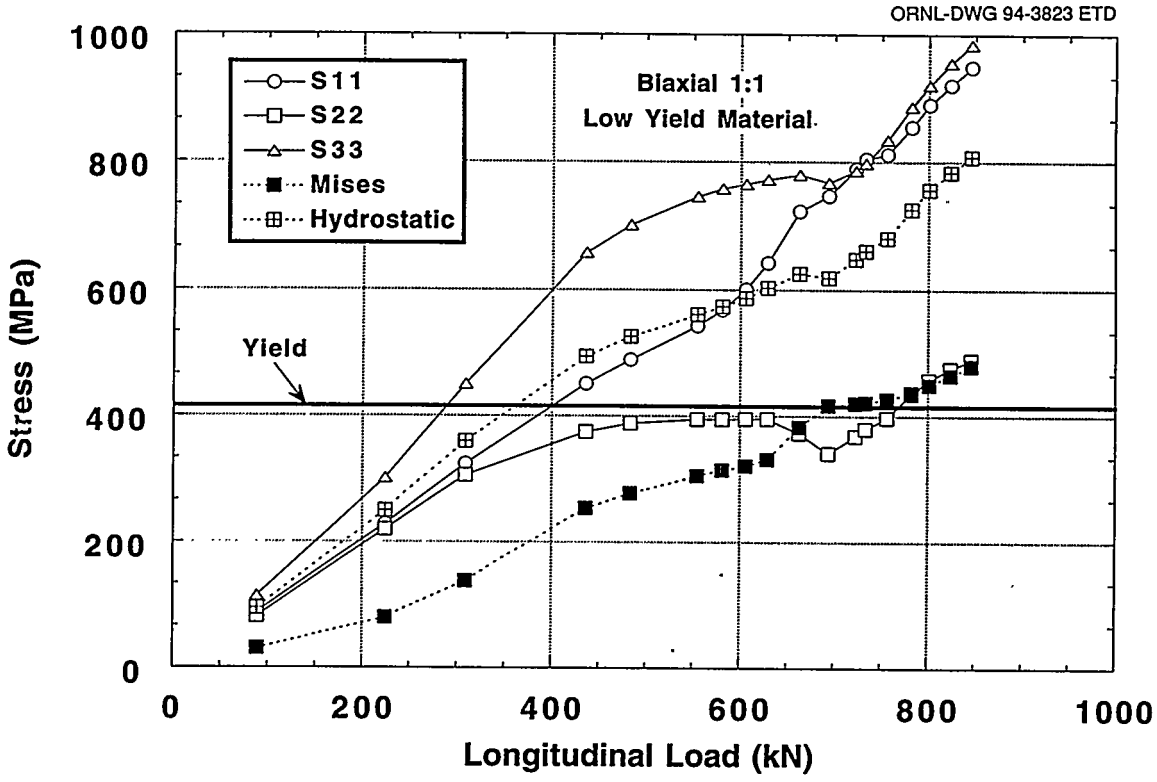

Figure 4.9 Stress components examined at material point 2.5-mm ahead of crack tip for biaxial 1:1 loading

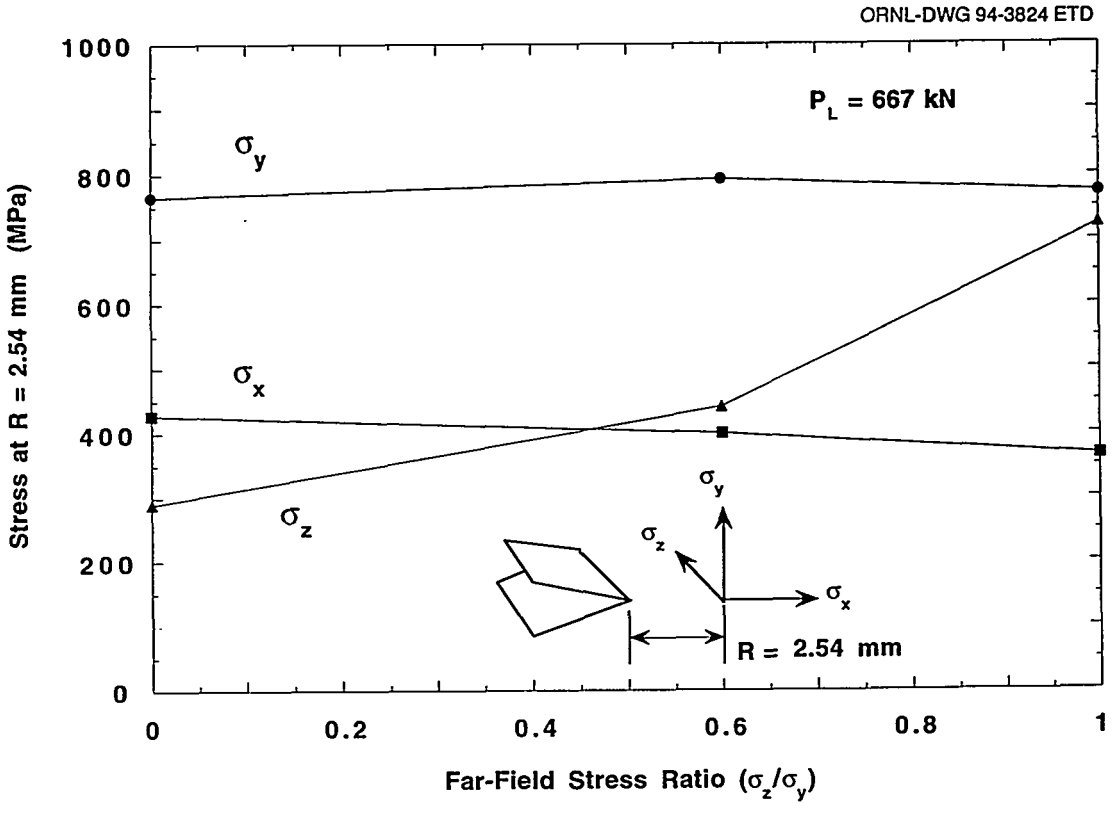

Figure 4.10 Far-field stress biaxiality exerting little influence on in-plane stress near crack tip

methodologies formulated in terms of in-plane stress components cannot detect the biaxial toughness effect clearly demonstrated in the ORNL data base. This conclusion is supported by measured biaxial toughness data (Fig. 4.1) and results depicted in Figs. 4.4 and 4.5 from applications of the D-A scaling procedure to the biaxially loaded cruciform specimen.

4.2.2 Stress-Strain-Based Methodologies

Experimental and analytical investigations presented in the previous section concluded that out-of-plane biaxial loading has no significant effect on in-plane stresses ahead of the crack tip. However, biaxial loading does influence development of the crack-tip plastic zone in the direction of crack propagation. These results, as well as results from prior experimental/analytical studies (described below), suggest that a strain-based fracture-toughness correlation is appropriate for RPV steels in the transition temperature region. This section describes studies initiated within the HSST Program that attempt to characterize crack-tip conditions through development and application of strain-based correlation methodologies.

Fractographic data obtained from examinations of broken halves of uniaxially and biaxially loaded cruciform specimens[12] were found to be consistent with a strain-based fracture-toughness correlation. Figure 4.11(*a*) depicts the normalized opening-mode near-crack-tip stress distributions obtained from finite-strain analyses of cruciform specimens; the stress distributions are plotted vs normalized distance in front of the crack tip. The finite-strain SSY solution is shown for reference. In Fig. 4.11(*b*), initiation toughness data are plotted vs normalized distance from the initial crack-tip locations to the cleavage initiation sites. These data incorporate crack initiation sites located in the region of the crack-tip process zone where strain is increasing, but stress is decreasing (i.e., to the left of stress peak A) with increasing applied load. The expectation is that a cleavage initiation event will be governed by a criterion that exhibits a rising near-tip field at the initiation site under increasing applied load.

Previous investigations of strain-based methodologies in the transition region include those of Clausing,[13] Barsom,[14] Merkle,[15] Weiss,[16] Pennell,[17] and Tetleman and McEvily (T-M)[18]. Clausing[13] related the decrease in toughness associated with increased strength of structural steels to a decrease in plane-strain ductility. Barsom[14] and Merkle[15] developed expressions for K_{Ic} based on plane-strain ductility, both of which compared well with measured toughness data in the transition temperature region.

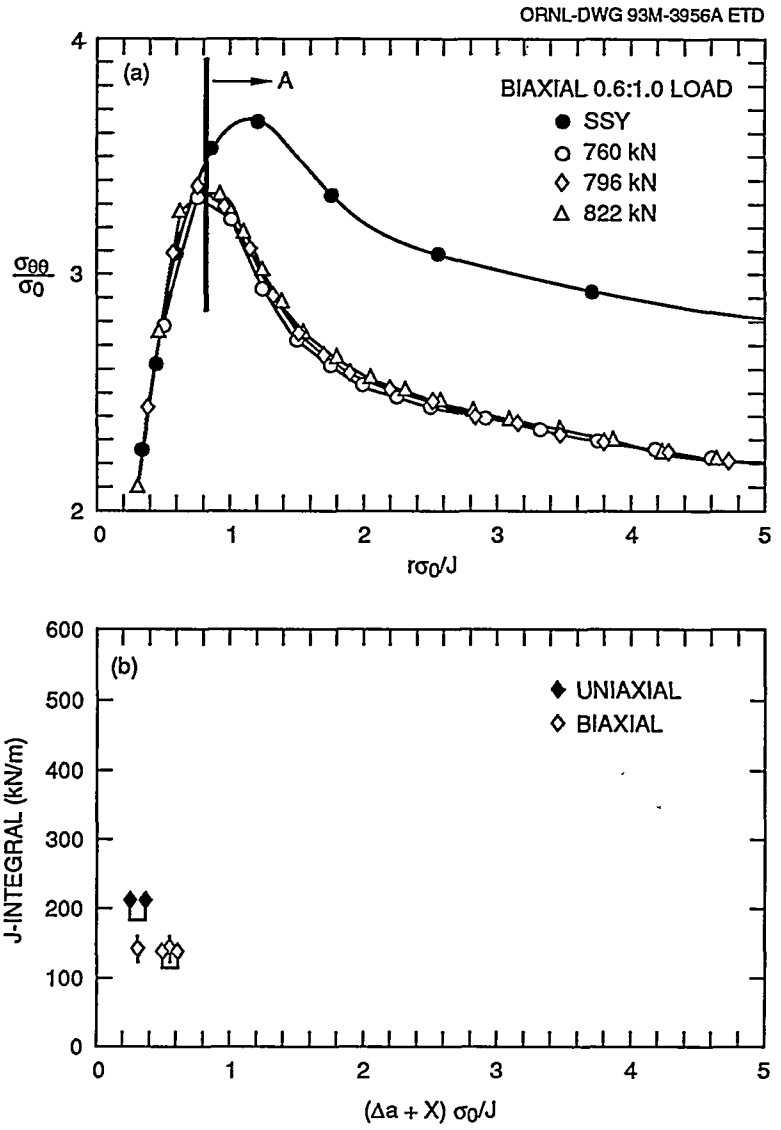

Figure 4.11 Initiation site locations determined from fractographic data indicating that strain-based failure modes may govern fracture initiation under biaxial loading at temperature in transition region

Weiss[16] developed an analytical relation for fracture toughness based on the material fracture strain. Pennell[17] adapted the Weiss relation to provide an estimate of biaxial loading effects on cleavage fracture toughness for RPV steels. In Ref. 17, the ratio of toughness values (K_b/K_u) corresponding to equibiaxial and uniaxial loading conditions, respectively, is predicted to be 0.47. This predicted value compares with the lower-bound K_b/K_u ratio of 0.57 obtained from measured data for A 533 B steel. The good agreement between analytical prediction and measured data provides further support for a strain-based fracture-toughness correlation.

According to the T-M criterion[18] plastically induced fracture initiates in a ligament immediately adjacent to the blunted crack tip when the ligament strain reaches the fracture strain (ef) of the material. Pennell* has interpreted the T-M fracture criterion as a limiting condition for absorption of energy by the crack-tip material as a result of inelastic deformation. In addition, it was suggested that the effects of constraint on fracture toughness can be quantified by analyzing the response of the crack-tip material to increasing load and determining the radius of the blunted crack tip corresponding to the crack-tip ligament strain at fracture (ef). Direct application of the latter strain-based approach would require a finite-strain elastic-plastic FEA to determine the crack-tip radius as a function of the ligament strain. To circumvent this computationally intensive approach, Pennell* proposes an alternative

*W. E. Pennell, "Reactor Pressure Vessel Structural Integrity Research," presented at the 22nd Water Reactor Safety Meeting, Bethesda, Md., October 24–26, 1994. To be published in "Proceedings of the U.S. Nuclear Regulatory Commission 22nd Water Reactor Safety Information Meeting," NUREG/CP-0140.

methodology that utilizes R, the plastic zone width in the plane of the crack, as a correlation parameter for fracture toughness. An important feature of this methodology is that the parameter R can be calculated accurately in a small-strain analysis.

An analytical basis for the approach utilizing plastic zone width R as a correlation parameter is found in the T-M development.[18] The T-M formulation relates R and crack-tip displacement as a function of applied stress, crack depth, and crack-tip radius for the case of plane-stress tensile loading and contained yielding. For the latter conditions, the T-M formulation leads to a proportional relationship between R and the crack-opening displacement. An analytical relation for the case of plane-strain tensile loading is not provided, although some approximations are discussed in Ref. 18. Existence of a relationship between these variables for conditions approaching plane strain is suggested by toughness data and computational results from 3-D inelastic analysis that are discussed at the end of this section.

Development of an HSST strain-based methodology is focusing on correlations of the cruciform test results with simple functions of the plastic zone width R. The investigation of biaxial loading effects on ligament conditions [at location r = 2.54 mm (0.1 in.)] described in the previous section provides the variation of R with applied load shown in Fig. 4.12; the biaxial load ratio is taken as a parameter in this figure. The analyses revealed that increasing the load ratio from 0:1 to 0.6:1 effectively delays the onset of yielding to a much higher applied load in the latter case. Further increase of the ratio to 1:1 leads to relatively abrupt uncontained yielding at an intermediate load level [at ~667 kN (150 kips)], followed by behavior essentially like that of the uniaxial case for load levels beyond those shown in Fig. 4.12. Thus, a material point ahead of the crack tip experiences yielding at different load levels, depending on the out-of-plane loading. Studies have been initiated within the HSST Program to further clarify cause-and-effect relationships among the R-parameter, the load level, and the biaxiality ratio that lead to results for the cruciform specimen depicted in Fig. 4.12.

Pennell* has observed that the abrupt development of uncontained yielding in the 1:1 case may explain why some researchers, using small test specimens in which uncontained yielding was unavoidable, have reported no

*W. E. Pennell, "Reactor Pressure Vessel Structural Integrity Research," presented at the 22nd Water Reactor Safety Meeting, Bethesda, Md., October 24–26, 1994. To be published in "Proceedings of the U.S. Nuclear Regulatory Commission 22nd Water Reactor Safety Information Meeting," NUREG/CP-0140.

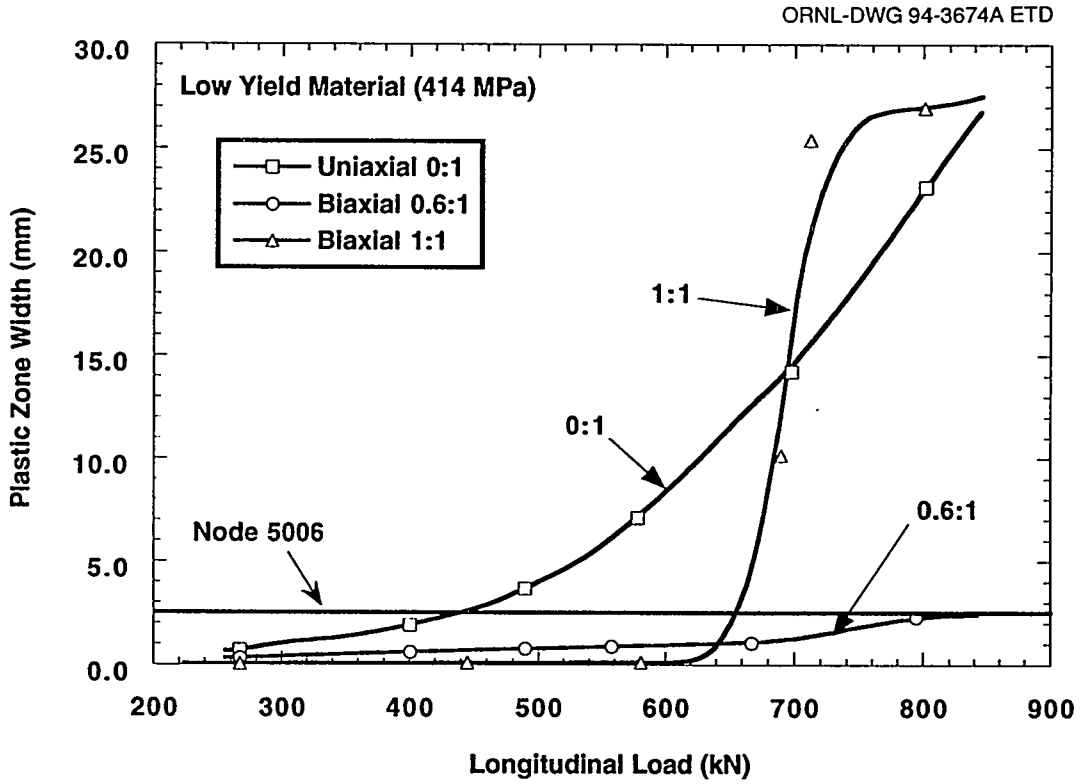

Figure 4.12 Material point (node 5006) 2.54 mm ahead of crack tip that experiences yielding at different load levels, depending on out-of-plane loading ratio

effects of biaxial loading on fracture toughness. Development of the crack-tip plastic zone in the cruciform specimen for three different loading ratios, that is, 0:1, 0.6:1 and 1:1, is depicted for a portion of the specimen in Figs. 4.13–4.15.

The ORNL/HSST strain-based constraint-effects model, incorporating R as a second parameter, was utilized to predict an effect of biaxial loading on fracture toughness. This approach is illustrated in Fig. 4.16 where the biaxial fracture-toughness data from Fig. 4.1 is plotted as a function of the natural logarithm of the plastic zone width [ln(R)]. The data conform essentially to a straight-line relationship when plotted as a function of ln(R). The $\pm 22\text{-MPa}\sqrt{m}$ uncertainty band in Fig. 4.16 represents the fracture-toughness locus for the A 533 B test material, corresponding to a single normalized temperature (T – NDT) of –10°C. A family of similar fracture-toughness loci would be required to span the full range of normalized temperatures that could be encountered in an RPV transient analysis.

In Fig. 4.17, K_J vs ln(R) loading trajectories for the three cruciform analyses are superposed on the fracture-toughness locus of Fig. 4.16. These trajectories have three distinct phases that are characterized by the growth rate for R. The range of fracture-toughness values possible at T – NDT = –10°C, for a given loading condition, is predicted by the intersection of the K_J vs ln(R) loading trajectory with this fracture-toughness locus. In Fig. 4.17, unique K_{Jc} values are predicted for the uniaxial and biaxial 0.6:1 loading cases. The intersection of the K_J vs ln(R) trajectory for biaxial 1:1 loading with the toughness locus predicts both low and high K_{Jc} values for this loading condition. In fact, these low and high toughness values were realized in two tests of the biaxial 1:1 loading case; these toughness data are given in Fig. 4.1. Uncontained yielding that developed in two of the biaxial 1:1 tests gave high toughness values that were similar to those of the uniaxial loading tests.

Implicit in the previous correlation of biaxial toughness data with the parameter R is an apparent influence of crack-tip strains on determination of cleavage fracture toughness in the transition region. Specifically, strains in the plastic zone adjacent to the blunted crack tip are observed to increase as the root radius of the blunted crack decreases. Furthermore, the root radius of the blunted crack can be related directly to the width R of the plastic zone under certain conditions (see Ref. 18). Thus, correlation of fracture toughness with the width R may be due to the effect of biaxial loading in restricting the growth of the root radius of the blunted crack. Consequences of this effect

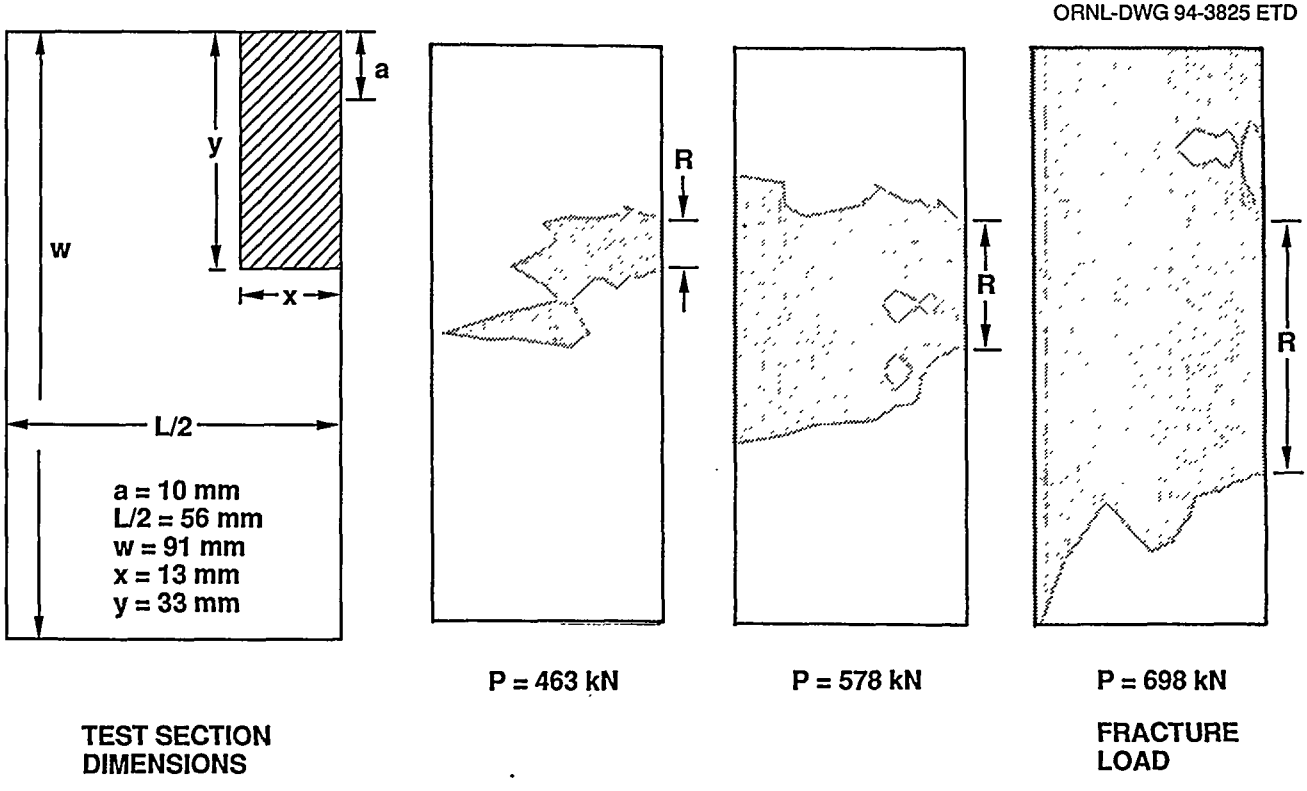

Figure 4.13 Development of crack-tip plastic zone under uniaxial (0:1) loading

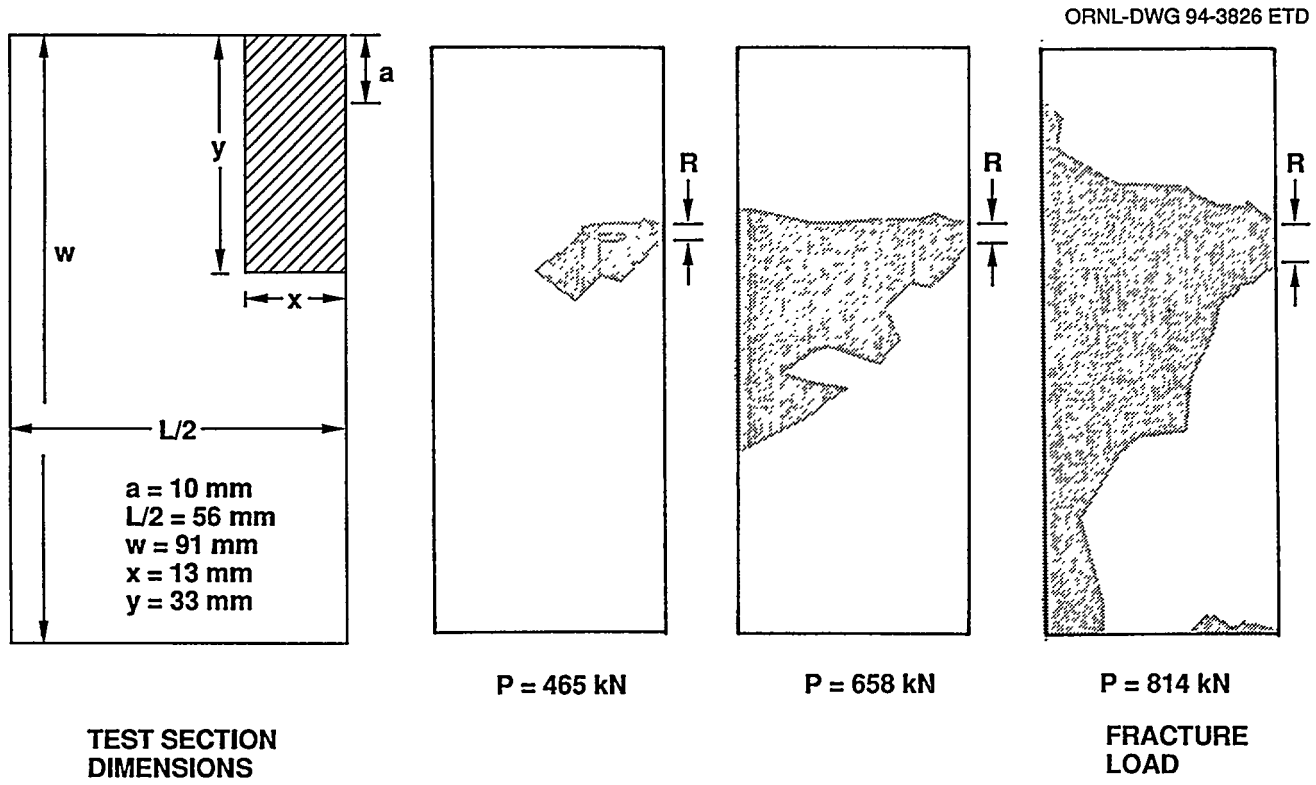

Figure 4.14 Development of crack-tip plastic zone under biaxial (0.6:1) loading

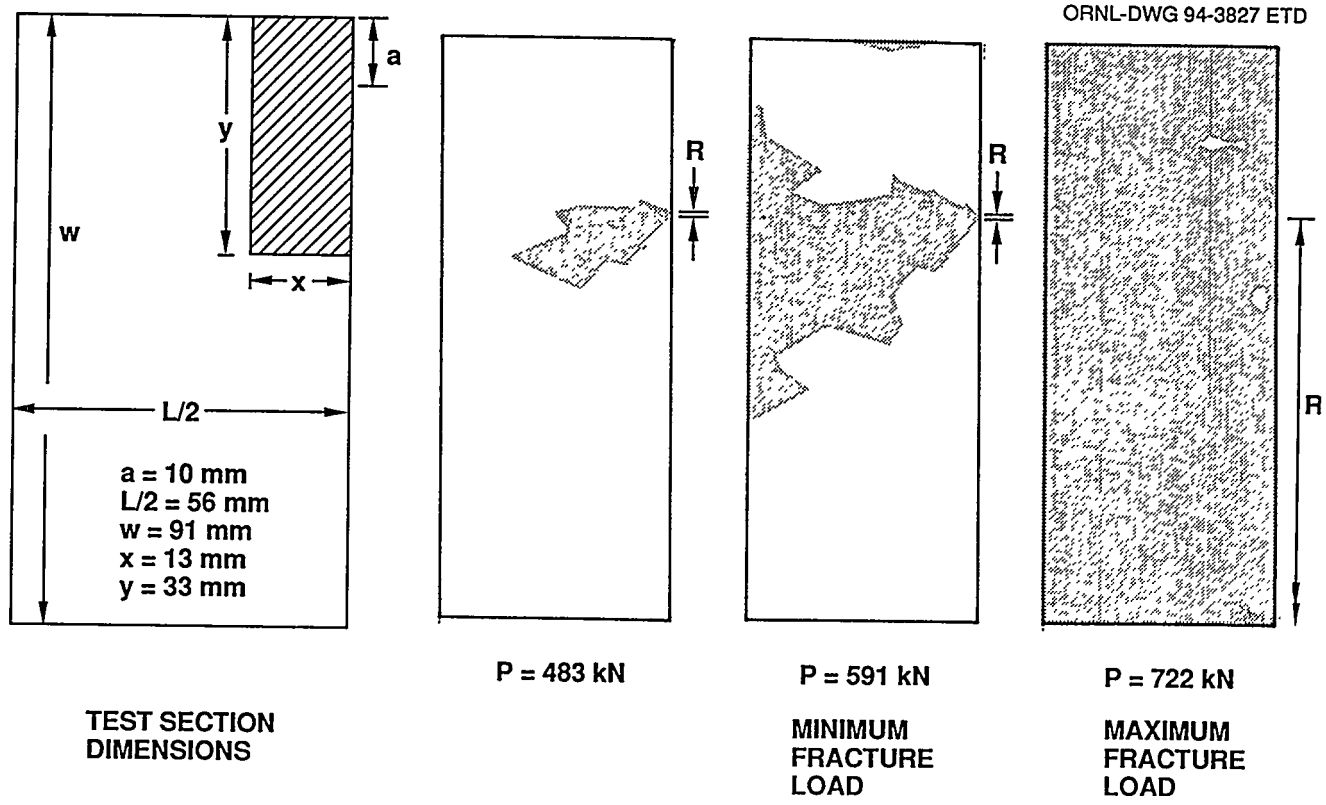

Figure 4.15 Development of crack-tip plastic zone under biaxial (1:1) loading

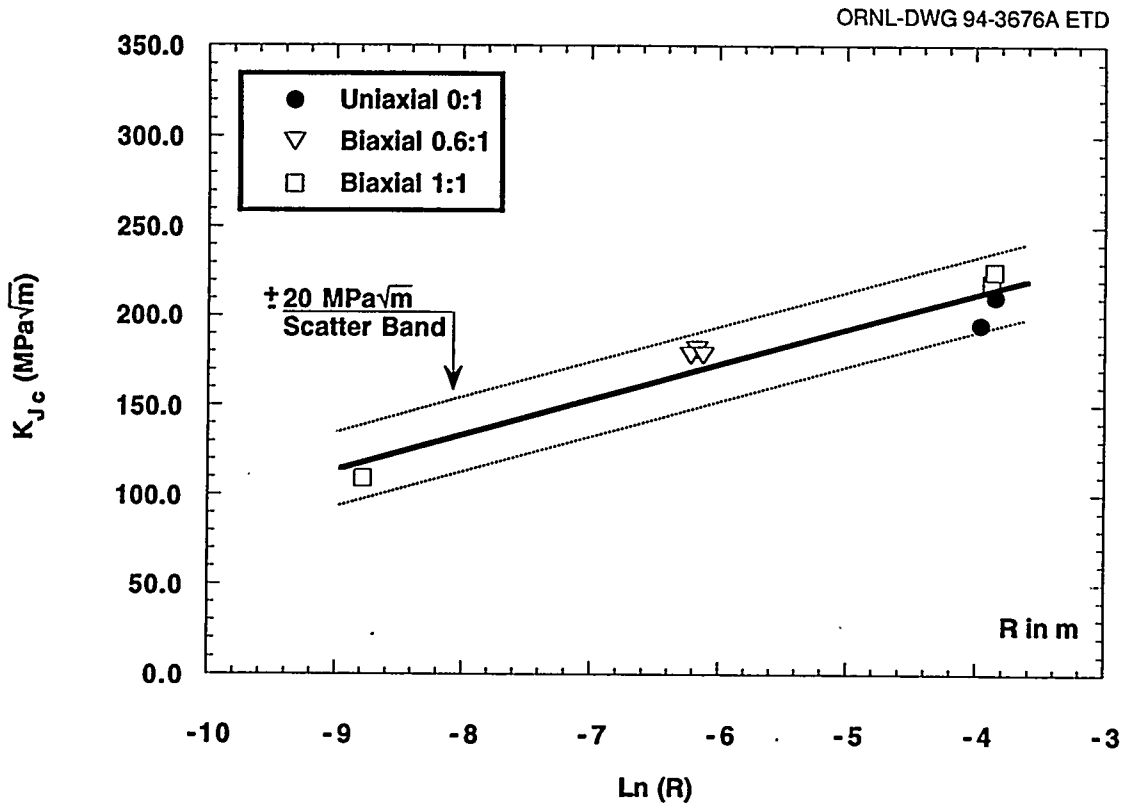

Figure 4.16 Shallow-flaw fracture-toughness locus, K_J-Ln(R), defined by results from cruciform specimen tests

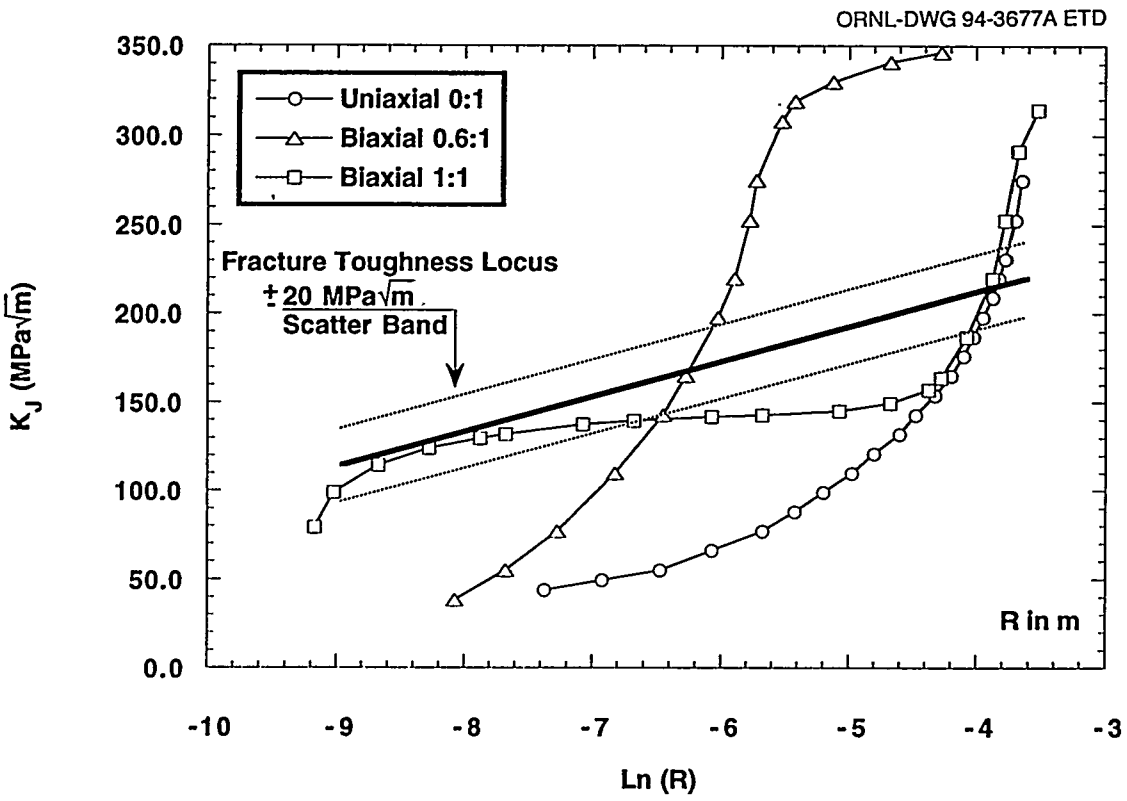

Figure 4.17 K_J – Ln(R) trajectories for biaxial loading with three distinct phases characterized by plastic zone width (R) growth rate. Intersection of trajectory for 1:1 loading with fracture-toughness locus predicts both low and high K_{Jc} values for this loading condition

may be such that strains in the near-tip region increase to the plane-strain fracture ductility of the material. Confirmation of this fracture model for the cruciform specimen under uniaxial and biaxial loading requires computationally intensive finite-strain inelastic analyses of the crack-tip region that are not yet completed. Some evidence for these arguments is provided by normalized curves for cleavage fracture toughness (K_{Jc}) and crack-tip opening displacement (CTOD) of the cruciform specimens vs ln(R), which are found to have similar trends (see Fig. 4.18).

The results presented in this section lend support to the argument that the strain-based K_J vs ln(R) approach has potential as a dual-parameter correlation model capable of representing fracture behavior of RPV steels in the transition region, including effects of biaxial out-of-plane loading on fracture toughness.

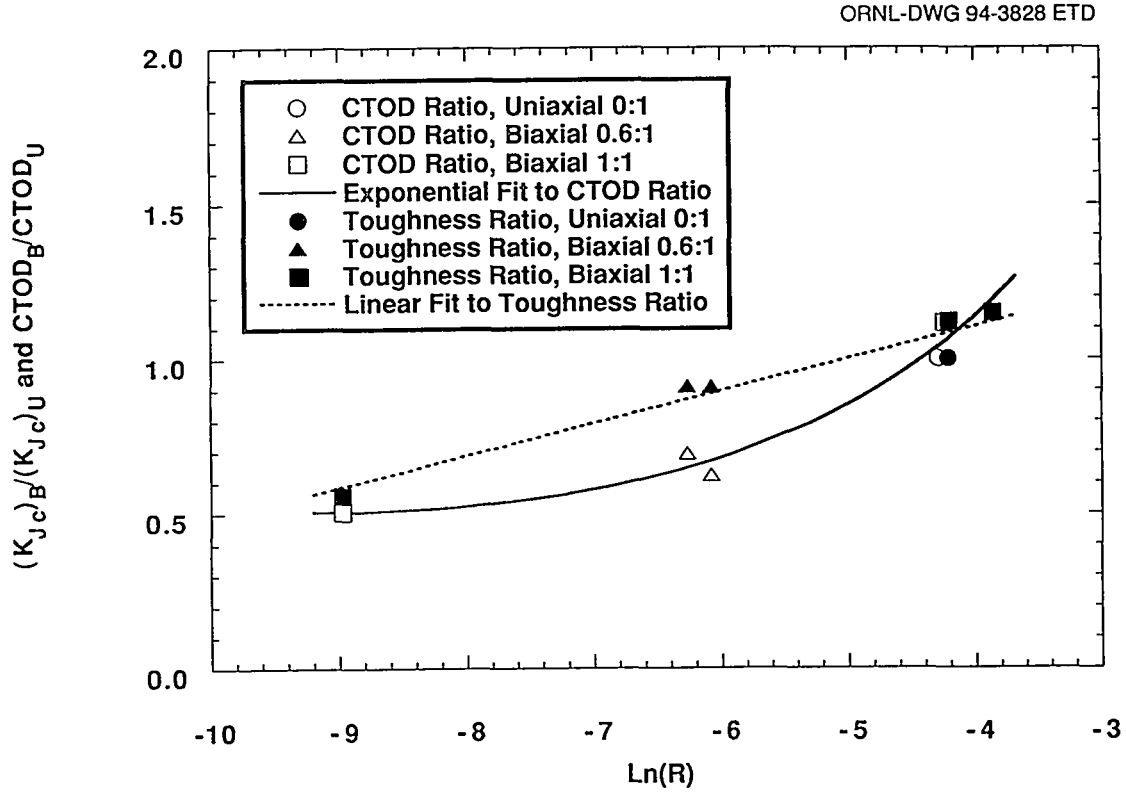

Figure 4.18 Similar trends of normalized K_{Jc} and CTOD curves suggesting that biaxial loading acts to inhibit crack-tip blunting and thereby decrease fracture toughness by increasing strains adjacent to the crack tip

References

1. T. H. Theiss and D. K. M. Shum, Martin Marietta Energy Systems, Inc., Oak Ridge National Laboratory, "Experimental and Analytical Investigation of the Shallow-Flaw Effect in Reactor Pressure Vessels," USNRC Report NUREG/CR-5886 (ORNL/TM-12115), July 1992.*

2. R. H. Dodds, C. F. Shih, and T. L. Anderson, "Continuum and Micromechanics Treatment of Constraint in Fracture," University of Illinois, UILU/ENG-92-2014, November 1992.†

3. R. M. McMeeking and D. M. Parks, "On Criteria for J-Dominance of Crack-Tip Fields in Large-Scale Yielding," pp. 175–194 in *Elastic-Plastic Fracture*, ASTM STP 668, American Society for Testing and Materials, 1979.†

4. C. F. Shih and M. D. German, "Requirements for One Parameter Characterization of Crack Tip Fields by the HRR Singularity," *Int. J. Fract.* 17(1), 27–43 (1981).†

5. A. M. Al-Ani and J. W. Hancock, "J-Dominance of Short Cracks in Tension and Bending," *J. Mech. Phys. Solids* (39), 23–43 (1991).†

6. N. P. O'Dowd and C. F. Shih, "Family of Crack-Tip Fields Characterized by a Triaxiality Parameter: Part I–Structure of Fields," *J. Mech. Phys. Solids* 39, 989–1015 (1991).†

7. N. P. O'Dowd and C. F. Shih, "Family of Crack-Tip Fields Characterized by a Triaxiality Parameter: Part II–Fracture Applications," *J. Mech. Phys. Solids* 40, 939–963 (1992).†

8. N. P. O'Dowd and C. F. Shih, "Two Parameter Fracture Mechanics: Theory and Applications," USNRC Report NUREG/CR-5958 (CDNSWC/SME-CR-16-92), Naval Surface Warfare Center, February 1993.*

9. R. O. Ritchie, J. F. Knott, and J. R. Rice, "On the Relationship Between Critical Tensile Stress and Fracture Toughness in Mild Steel," *J. Mech. Phys. Solids* 21, 395–410 (1973).†

10. R. H. Dodds, T. L. Anderson, and M. T. Kirk, "A Framework to Correlate a/W Ratio Effects on Elastic-Plastic Fracture Toughness (J_c)," *Int. J. Frac.* 48, 1-22 (1991).†

11. T. L. Anderson and R. H. Dodds, "Specimen Size Requirements for Fracture Toughness Testing in the Ductile-Brittle Transition Region," *J. Test. Eval.* 19, 123–134 (1991).†

12. B. R. Bass, J. W. Bryson, T. J. Theiss, and M. C. Rao, Martin Marietta Energy Systems, Inc., Oak Ridge National Laboratory, "Biaxial Loading and Shallow Flaw Effects on Crack-Tip Constraint and Fracture Toughness," USNRC Report NUREG/CR-6132 (ORNL/TM-12498), January 1994.*

13. D. P. Clausing, "Effect of Plastic-Strain State on Ductility and Toughness," *Int. J. Fract. Mech.* 6(1) (March 1970).†

14. J. M. Barsom, "Relationship Between Plane-Strain Ductility and K_{Ic} for Various Steels,"Paper 71-PVP-13, *Journal Engineering for Industry* (November 1971).†

15. J. G. Merkle, Union Carbide Corp. Nucl. Div., Oak Ridge National Laboratory, "An Elastic-Plastic Thick-Walled Hollow Cylinder Analogy for Analyzing the Strains in the Plastic Zone Just Ahead of a Notch Tip," ORNL/TM-4071, January 1973.*

16. V. Weiss, "Material Ductility and Fracture Toughness of Metals," *Proceedings of the International Conference on Mechanical Behavior of Materials, Kyoto, Japan, August 15–20, 1971*, The Society of Materials Science, Japan, 1971.†

17. W. E. Pennell, "Heavy-Section Steel Technology Program: Recent Developments in Crack Initiation and Arrest Research," *Nucl. Eng. Des.* 255–266 (1993).†

18. A. S. Tetleman and A. J. McEvily, Jr., *Fracture of Structural Materials* (John Wiley & Sons, Inc., New York, 1967).†

*Available for purchase from National Technical Information Service, Springfield, VA 22161.
†Available in public technical libraries.

5 Summary and Conclusions

This report contains the preliminary results for an investigation of the effects of biaxial loading on fracture toughness of RPV steels and for an assessment of methodologies used in describing the effect of such loading on toughness predictions. Three-dimensional FEAs have shown that biaxial loading, a condition characterized by imposition of a far-field out-of-plane stress component on the flaw tip, changes the constraint conditions at the crack tip and may alter the apparent fracture toughness of the material. Any modification of RPV fracture toughness, either through loading conditions or crack-tip constraint, must be assessed for its effect on the fracture mechanics technologies used in the safety assessment procedures for commercially licensed nuclear RPVs. A validated technology that incorporates constraint effects is essential both in the proper evaluation of RPV loading conditions on crack-tip response and on the transfer of fracture-toughness data from laboratory-scale specimens, particularly miniature specimens proposed for use in surveillance programs, to RPV safety assessments.

That constraint has an effect on fracture toughness has been demonstrated through prior experimental testing. Uniaxial tests of SENB specimens with either deep or shallow flaws have shown that fracture toughness is elevated for shallow flaws relative to deep flaws. Through analyses, this elevation has been shown to be the result of reduced constraint at the crack tip. Crack-tip constraint conditions can be modified by the application of other than uniaxial loads. Application of a far-field out-of-plane stress has the potential to increase stress triaxiality (constraint) at the crack tip and thereby reduce some of the fracture-toughness elevation associated with shallow flaws. This effect can also be inferred from existing biaxial fracture-toughness data which suggest that biaxial loading will result in a reduction in fracture toughness as compared to uniaxial results.

This investigation was thus aimed at developing a fracture-toughness data base of sufficient extent to demonstrate the general effect of biaxial loading on toughness and to permit a preliminary evaluation of the applicability of existing constraint methodologies. An evaluation of alternate specimen designs indicated the superiority of a cruciform beam specimen with a 2-D shallow, through-thickness flaw for the proposed testing. A special loading fixture was also designed and constructed to permit testing of this specimen configuration under a range of biaxiality ratios. This fixture was designed with a beam reaction support system that resulted in statically determinant reaction loads. This permitted tests of nominally identical specimens with the applied stress biaxiality being the only variable between tests.

Provisions for a full range of instrumentation were provided to measure specimen CMOD, LLD, surface strains, beam arm load, and applied load. Full operability and functionality of the generic specimen design and the load fixture were demonstrated through a detailed sequence of shakedown tests. A series of development tests were then performed to generate biaxial data, to refine the specimen design, and to demonstrate the viability of the specimen/fixture design for producing biaxial fracture-toughness data. Specimens subjected to biaxial-bending load ratios of 0:1 (uniaxial) or 0.6:1 were tested, and critical fracture-toughness values were calculated for each test using load vs LLD and load vs CMOD experimental results in conjunction with 3-D elastic-plastic FEAs. These tests showed that biaxial loading of 0.6:1 resulted in a reduction in fracture toughness of ~12% as compared to the uniaxial test (BB-2). Also, the 0.6:1 subset (three tests: BB-1, -4, and -5) showed remarkably little scatter as compared to conventional compact tension or SENB fracture test results. The matrix was then extended to include full 1:1 biaxial loading. The three biaxial (1:1) tests (BB-7, -9, and -10) behaved in an unexpected manner because the results yielded two subsets of toughness values. The first subset, two specimens (BB-7 and -9), agreed within 3% of each other, and the mean of the subset agreed with the mean of the uniaxial results within < 4%. The second 1:1 subset, one specimen (BB-10), yielded a fracture toughness of 43% less than that of the other 1:1 subset. It was concluded that this last test could readily be explained using a ductility-based constraint procedure. More discussion on this follows.

Of the nine specimens tested in this effort, seven gave valid fracture-toughness results as judged by location of the fracture initiation site(s). Specifically, the criterion used was that initiation should occur within approximately the center two-thirds of the crack front. Over this region, the analyses indicated near uniform stress intensity values resulting from either uniaxial or biaxial loading. One specimen (BB-1) failed near the edge of the specimen but was considered to provide valid results for the intended purpose. One specimen (BB-3) failed at the specimen edge and was considered invalid. With refinements in the specimen design, all failures occurred near the center of the crack front. It is concluded that a valid specimen for biaxial fracture-toughness testing has been developed.

The two stress-based dual-parameter methodologies, the J-Q theory and the D-A micromechanical scaling model, were assessed for their capability in describing the observed experimental results. Previous work had indicated that both of these methodologies could be used with success in an interpretation of the fracture-toughness

test results from both shallow- and deep-flaw SENB specimens under uniaxial loading. When these methodologies were applied to the cruciform test results, however, inconsistencies were observed both between the predictive techniques and between the techniques and the experimental data. Considering the uniaxial and biaxial (0.6:1) cruciform results, the D-A scaling model predicted no biaxial effect. The J-Q method gave results that were generally inconclusive. A major deficiency was noted when both methods were applied to the 1:1 biaxial data. Both failed to predict the observed reduction in fracture toughness obtained in the test of specimen BB-10. The D-A and J-Q methodologies are applied to in-plane stress at the crack tip. Three-dimensional elastic-plastic FEAs have shown that an out-of-plane far-field stress (stress biaxiality) has very little effect on in-plane stresses at the flaw tip. It was concluded that the stress-based, dual-parameter, fracture-toughness correlations, in their present form, are not capable of predicting the fracture-toughness reductions observed in these biaxial loading tests.

In an attempt to better understand the above conclusion, additional FEAs were performed to investigate the relationship between biaxial loading and the stress and strain fields at the crack tip. It was observed that out-of-plane far-field stresses have a strong influence on the plastic deformation at the flaw tip. The out-of-plane stress acts to inhibit both blunting of the flaw tip and growth of the flaw-tip plastic zone width. An implicit strain-based, dual-parameter, fracture-toughness correlation was proposed and investigated as an alternative method for quantifying the cruciform test results. The parameters utilized were K_{Jc} and ln(R), where R is the width of the plastic zone in the plane of the flaw and in the direction of flaw propagation, that is, nominally normal to the flaw front.

Substantiation for a strain-based methodology stems in part from fractographic observations on the location of cleavage fracture initiation sites in SENB and cruciform specimens in conjunction with 3-D FEAs that provide stress and plastic strain distributions around the flaw tip. The initiation sites are located in a region where the opening-mode stress is decreasing, after going through a maximum while the plastic strain is increasing. When applied to the cruciform data, the [K_{Jc}, ln(R)] fracture-toughness correlation performed acceptably for both the uniaxial and biaxial cruciform specimen tests. Specifically, this model predicts the possibility for both low- and high-toughness values observed for cases of 1:1 biaxial loading. For the case of contained yielding at the flaw tip, the plastic zone size and, thus, the fracture toughness are reduced. Where uncontained yielding occurs, a plastic zone size comparable to that for uniaxial loading develops, and this method predicts 1:1 fracture-toughness values comparable to those obtained for the uniaxial tests. The reduction in toughness observed for the intermediate biaxiality ratio 0.6:1 is appropriately predicted using the plastic zone width determined from the analyses.

Evaluations of the cruciform test data have led to the conclusion that this dual-parameter strain-based model has the capability for representing fracture behavior of RPV steels in the transition region, including the effects of out-of-plane loading on fracture toughness.

INTERNAL DISTRIBUTION

1. D. J. Alexander
2–5. B. R. Bass
6–9. J. W. Bryson
10. J. M. Corum
11. W. R. Corwin
12. T. L. Dickson
13. R. G. Gilliland
14. F. M. Haggag
15. J. E. Jones Jr.
16. S. K. Iskander
17. J. A. Keeney
18–22. W. J. McAfee
23. D. E. McCabe
24. J. G. Merkle
25. R. K. Nanstad
26. D. J. Naus
27. W. E. Pennell
28. C. E. Pugh
29. C. C. Southmayd
30. Central Research Library
31. Document Reference Section
32–33. Laboratory Records
34. Laboratory Records (RC)

EXTERNAL DISTRIBUTION

35. T. L. Anderson, Department of Mechanical Engineering, Texas A&M University, College Station, Texas 77843.
36. W. H. Bamford, Westinghouse R&D Center, P.O. Box 2728, Pittsburgh, Pennsylvania 15230-2728.
37. R. G. Carter, 1300 W. T. Harris Boulevard, Charlotte, North Carolina 28262.
38. R. C. Cipolla, APTECH Engineering Services, Inc., 1282 Reamwood Avenue, Sunnyvale, California 94089.
39. R. Dodds, 3140 Newmark Laboratory, 205 North Matthews, Urbana, Illinois 61801.
40. R. Fields, National Institute of Standards and Technology, Bldg. 223, B144, Gaithersburg, Maryland 20899.
41. W. L. Fourney, Department of Mechanical Engineering, University of Maryland, College Park, Maryland 20742.
42. T. J. Griesbach, ATI Consulting, 2010 Crow Canyon Place, Suite 140, San Ramon, California 94583.
43. E. M. Hackett, Materials and Chemical Engineering Branch, U.S. Nuclear Regulatory Commission, Washington, D.C. 20555-0001.
44. G. R. Irwin, Department of Mechanical Engineering, University of Maryland, College Park, Maryland 20742.
45. L. James, Westinghouse Bettis Laboratory, P.O. Box 79, ZAP 13A, 814 Pittsburgh McKeesport Boulevard, West Mifflin, Pennsylvania 15122.
46. J. M. Joyce, U.S. Naval Academy, Annapolis, Maryland 21402.
47. J. D. Landes, The University of Tennessee, Knoxville, Tennessee 37996-2030.
48–49. S. N. M. Malik, Division of Engineering, U.S. Nuclear Regulatory Commission, MS-T10E10, Washington, D.C. 20555-0001.
50–51. M. E. Mayfield, Director, Division of Engineering, U.S. Nuclear Regulatory Commission, MS-T10E10, Washington, D.C. 20555-0001.
52. S. T. Rolfe, The University of Kansas, Lawrence, Kansas 66045-2235.
53. D. A. Scarth, Ontario Hydro Research Division, 800 Kipling Avenue, Toronto, Ontario, Canada M8Z 5S4.
54. C. W. Schwartz, Department of Civil Engineering, University of Maryland, College Park, Maryland 20742.
55. J. Strosnider, Division of Engineering, U.S. Nuclear Regulatory Commission, 1 White Flint, MS-N1D7, Washington, D.C. 20555-0001
56. F. A. Simonen, Pacific Northwest Laboratories, P.O. Box 999, Richland, Washington 99352.
57. E. T. Wessel, 312 Wolverine Street, Haines City, Florida 33844.
58. K. R. Wichman, Materials and Chemical Engineering Branch, U.S. Nuclear Regulatory Commission, Washington, D.C. 20555-0001.
59. Office of Assistant Manager for Energy Research and Development, DOE-ORO, Oak Rdge, TN 37831
60–61. Office of Scientific and Technical Information, P.O. Box 62, Oak Ridge, TN 37831.

NRC FORM 335 (2-89) NRCM 1102, 3201, 3202

U.S. NUCLEAR REGULATORY COMMISSION

BIBLIOGRAPHIC DATA SHEET

(See instructions on the reverse)

1. REPORT NUMBER (Assigned by NRC, Add Vol., Supp., Rev., and Addendum Numbers, if any.)

NUREG/CR-6273
ORNL/TM-12866

2. TITLE AND SUBTITLE

Biaxial Loading Effects on Fracture Toughness of Reactor Pressure Vessel Steel

3. DATE REPORT PUBLISHED

MONTH	YEAR
March	1995

4. FIN OR GRANT NUMBER

B0119

5. AUTHOR(S)

W. J. McAfee, B. R. Bass, J. W. Bryson, Jr., W. E. Pennell

6. TYPE OF REPORT

Technical

7. PERIOD COVERED *(Inclusive Dates)*

8. PERFORMING ORGANIZATION -- NAME AND ADDRESS *(If NRC, provide Division, Office or Region, U.S. Nuclear Regulatory Commission, and mailing address; if contractor, provide name and mailing address.)*

Oak Ridge National Laboratory
Oak Ridge, TN 37831-8056

9. SPONSORING ORGANIZATION -- NAME AND ADDRESS *(If NRC, type "Same as above"; if contractor, provide NRC Division, Office or Region, U.S. Nuclear Regulatory Commission, and mailing address.)*

Division of Engineering Technology
Office of Nuclear Regulatory Research
U.S. Nuclear Regulatory Commission
Washington, DC 20555-0001

10. SUPPLEMENTARY NOTES

11. ABSTRACT *(200 words or less)*

The preliminary phases of a program to develop and evaluate fracture methodologies for the assessment of crack-tip constraint effects on fracture toughness of reactor pressure vessel (RPV) steels has been completed by the Heavy-Section Steel Technology (HSST) Program. The primary objectives of this effort were to analytically and experimentally investigate the effect of biaxial loading on fracture toughness, to quantify this effect through use of existing stress-based, dual-parameter, fracture-toughness correlations, or to propose and verify alternate correlations. A cruciform beam specimen with a two-dimensional shallow, through-thickness flaw and a special loading fixture was designed and fabricated. Tests were performed using biaxial loading ratios of 0:1 (uniaxial), 0.6:1, and 1:1 (equi-biaxial). Critical fracture toughness values were calculated for each test. Biaxial loading of 0.6:1 resulted in a reduction in the lower bound fracture toughness of ≈12% as compared to the uniaxial tests. The biaxial loading of 1:1 yielded two subsets of toughness values; one agreed well with the uniaxial data while one was reduced by ≈43% when compared to the uniaxial data. The results were evaluated using the J-Q theory and the Dodds-Anderson (D-A) micromechanical scaling model. The D-A model predicted no biaxial effect while the J-Q method gave inconclusive results. When applied to the 1:1 biaxial data, these constraint methodologies failed to predict the observed reduction in fracture-toughness obtained in one experiment. A strain-based constraint methodology that considers the relationship between applied biaxial load, the plastic zone size at the flaw tip, and fracture-toughness was formulated and applied successfully to the data. Evaluation of this dual-parameter strain-based model led to the conclusion that it has the capability of representing fracture behavior of RPV steels in the transition region, including the effects of out-of-plane loading on fracture-toughness. This report is designated as HSST Report No. 150.

12. KEY WORDS/DESCRIPTORS *(List words or phrases that will assist researchers in locating the report.)*

A533 Grade B class 1 steel
Shallow-crack beam
Constraint Analysis
Biaxial loading
Factography
Elastic-plastic fracture mechanics
Fracture toughness data
J-Q Methodology
Constraint Adjustment model
Cruciform beam

13. AVAILABILITY STATEMENT

Unlimited

14. SECURITY CLASSIFICATION

(This Page) Unclassified

(This Report) Unclassified

15. NUMBER OF PAGES

16. PRICE

NRC FORM 335 (2-89)